ERDC/GSL TR-18-22

Geotechnical and Structures Laboratory

US Army Corps
of Engineers®
Engineer Research and
Development Center

ERDC
ENGINEER RESEARCH & DEVELOPMENT CENTER

Laboratory Investigations of Cohesionless Shear Strength in Low Confinement Environments

Katherine E. Winters, Oliver-Denzil S. Taylor,
Woodman W. Berry, Amy L. Cunningham, Wesley R. Rowland,
and Mark D. Antwine

August 2018

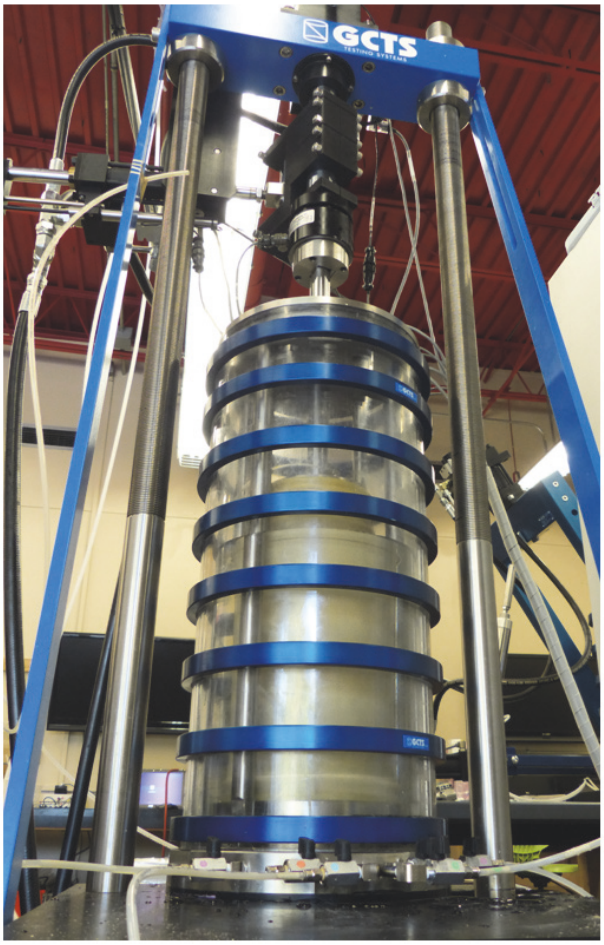

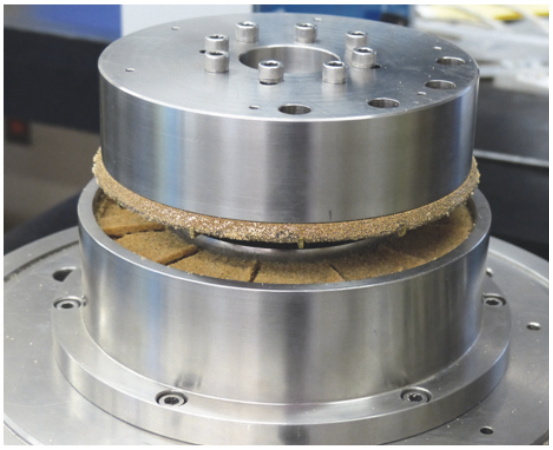

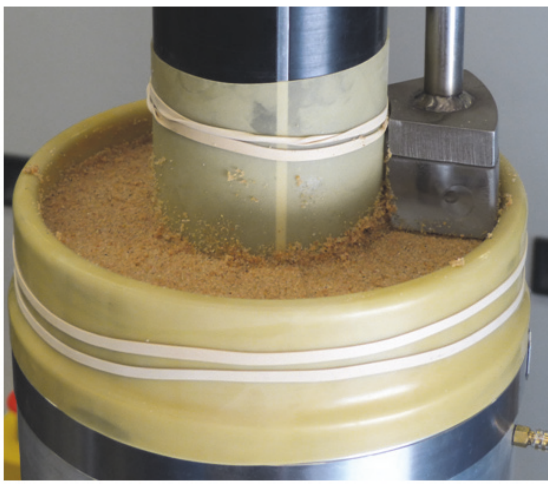

The U.S. Army Engineer Research and Development Center (ERDC) solves the nation's toughest engineering and environmental challenges. ERDC develops innovative solutions in civil and military engineering, geospatial sciences, water resources, and environmental sciences for the Army, the Department of Defense, civilian agencies, and our nation's public good. Find out more at www.erdc.usace.army.mil.

To search for other technical reports published by ERDC, visit the ERDC online library at http://acwc.sdp.sirsi.net/client/default.

ERDC/GSL TR-18-22
August 2018

Laboratory Investigations of Cohesionless Shear Strength in Low Confinement Environments

Katherine E. Winters, Oliver-Denzil S. Taylor,
Woodman W. Berry, Amy L. Cunningham, Wesley R. Rowland,
and Mark D. Antwine

Geotechnical and Structures Laboratory
U.S. Army Engineer Research and Development Center
3909 Halls Ferry Road
Vicksburg, MS 39180-6199

Final report

Prepared for U.S. Army Corps of Engineers
Washington, DC 20314-1000

Under Project 458272, “Integrated Force Protection Against Advanced Threats”

Abstract

In low-confining stress environments, Mohr-Coulomb failure mechanics implies that a cohesionless soil has negligible shear strength. This report presents results of total stress laboratory investigations from triaxial and simple shear loadings for three loose- to medium-dense, cohesionless materials, i.e., a poorly-graded sand (SP), a silty sand (SM), and a silt (ML), at confining pressures ranging from zero to 1,000 kPa, as well as cyclic ring shear testing of the SP material at confining pressures from 10 to 100 kPa. All materials exhibited shear strengths and stress paths in excess of expected failure surfaces at confining pressures under 100 kPa. The data indicate that cohesionless soils exhibit significant soil fabric strength characteristics that are not captured by the standard internal friction angle definition, as evidenced by the shear stress intercept of the trendlines relating shear strength and confining pressure. Under low confinement, the continuum fabric dominates the angle of the Mohr envelope. The significant difference in the Mohr envelope shape illustrates that the internal fabric's ability to resist different loading mechanisms cannot be assumed by a linear approximation.

Contents

Figures and Tables

Figures

Tables

Preface

This study was conducted for the U.S. Army Corps of Engineers under U.S. Army Military Engineering "Integrated Force Protection Against Advanced Threats" Program. The project manager was Dr. Michael I. Hammons.

The work was performed by the Structural Engineering Branch (StEB) of the Geosciences and Structures Division (GSD), U.S. Army Engineer Research and Development Center, Geotechnical and Structures Laboratory (ERDC-GSL). At the time of publication, Mr. Charles W. Ertle was Chief, StEB; Mr. James L. Davis was Chief, GSD; and Ms. Pamela G. Kinnebrew was the Technical Director for Military Engineering. The Deputy Director of ERDC-GSL was Dr. William P. Grogan, and the Director was Mr. Bartley P. Durst.

COL Ivan P. Beckman was the Commander of ERDC, and Dr. David W. Pittman was the Director.

Unit Conversion Factors

English - Multiply	By	To Obtain - Metric
cubic feet	0.02831685	cubic meters
cubic inches	1.6387064 E-05	cubic meters
cubic yards	0.7645549	cubic meters
feet	0.3048	meters
pounds (force) per foot	14.59390	newtons per meter
pounds (force) per inch	175.1268	newtons per meter
pounds (mass)	0.45359237	kilograms
pounds (mass) per cubic foot	16.01846	kilograms per cubic meter
pounds (mass) per cubic inch	2.757990 E+04	kilograms per cubic meter
yards	0.9144	meters

1 Introduction

Understanding the true behavior of cohesionless soils immediately impacts the fields of internal erosion prediction, surficial sloughing of dams and levee slopes, wave propagation, geo-sensor coupling, and geoenvironmental contamination and remediation designs. Laboratory experimentation on cohesionless soil fabric behavior in low-to-zero vertical confining pressure environments (representing the upper one meter) relies on the use of effective stress principles to infer behavior (Fannin et al. 2005; Huang et al. 2015; Lancelot et al. 2006). However, effective-stress-based laboratory tests are not indicative of low-confining pressure in situ environments. Mohr-Coulomb mechanics defines a continuum's shear strength, τ, as a function of the normal effective stress along the failure plane, σ_f'.

$$\tau = c' + \sigma_f' \tan(\phi_f') \quad (1)$$

For cohesionless materials, the c' parameter is assumed to be zero, and the internal friction angle, ϕ_f', is then determined through a best-fit failure envelope anchored around the origin of the Mohr diagram (τ vs. σ' graph). In low-confining stress environments, this implies that a cohesionless soil has negligible shear strength. Ho wever, confining pressure is not the only factor that contributes to a soil's ability to resist shear. The structure and fabric of the soil must also be explicitly accounted for. The term soil continuum fabric is defined as the inclusion of both the soil fabric and structure as defined by Mitchell and Soga (2005) as well as the sum of the continuum granular contact forces (Koustuvee et al. 2014) that govern a specimen's strength and volumetric behavior. The validity of Equation 1 then relies on the standard definitions of ϕ_f' and c'. For most geotechnical problems, Equation 1 yields relatively accurate approximations due to moderate to high-confining stresses. However, the failure plane suggested by Mohr-Coulomb mechanics may not be the actual failure plane upon which shear strains concentrate under near-surface environments. Herein, the terms "theoretical failure plane" and "observational failure plane" are used to signify the expected failure plane following traditional Mohr-Coulomb mechanics and the failure plane calculated from the test data, respectively.

To illustrate the significance of the conservatism of Mohr-Coulomb mechanics and the effects of soil continuum fabric on the continuum shear strength within low-confining pressure environments, this report presents results from total stress laboratory investigations from triaxial and simple shear loadings for three cohesionless materials, i.e., a loose-to-medium-dense poorly-graded sand (SP), a silty sand (SM), and a silt (ML), and cyclic shear loading of poorly-graded sand (SP).

1.1 Background

Seismic arrays are utilized globally to persistently monitor subsurface events, spanning a variety of technologies from permanently emplaced borehole seismometer networks to monitor earthquakes (Chapman 2013), to mobile and temporarily deployed oil and gas land-streamer geophone survey rigs (Tsoflias et al. 2006). Through careful analysis, these seismic arrays can forensically investigate events of interest, such as discrimination of nuclear and chemical explosions (Stump et al. 1999), pipeline explosions (Koper et al. 2003), and even military events (Bonner et al. 2013). However, in order to effectively reconstruct source properties such as duration, spatial length, strength or dominant period, and yield, receiver-side effects must be properly assessed for each deployment. The emplacement location of these sensors balances the need for signal identification and logistics. Historically, the geophysical sensor is placed in a relatively quiet location to allow maximum signal detection, and calibration surveys are performed to assess quality of the environment. Ideally, seismic sensors are emplaced in a hard rock environment with a low-noise field, ensuring the maximum possible signal-to-noise ratio. The ability to discriminate between triggering seismic sources, e.g., person(s), animals, vehicular type(s), etc., and their distance/direction from the receiver is necessary for persistent monitoring geophysical instrumentation, no matter the time scale of deployment.

Generally, arrays can be considered a suite of instruments subject to an integrated processing scheme. The design of a given array is situated to meet one or more objectives, such as the detection of low-magnitude events or the location of events. The advantages inherent in using arrays include the separation of the signal from the local noise, the improvement of the signal-to-noise ratio for small events, and the determination of phase velocity and back-azimuth or direction of arrival. Therefore, arrays are designed for the optimum detection of signals with sufficient reliability to enhance weak signals (Ringdal and Husebye 1982; Mykkeltveit et al.

1990). The amplitude of observed signals is directly dependent on the absorption loss over the propagation path. It is difficult to measure absorption in the field because the relationship between laboratory measurements and observations in the field is not clearly defined (Sheriff and Geldart 1995).

Ideally, seismic arrays are situated in a medium that is not sensitive to low confinement conditions, e.g., the bedrock installation of earthquake monitoring networks, thereby simplifying the contribution of propagation path effects on source identification. However, operational arrays with deployments spanning days to months do not have the luxury of avoiding inconvenient meteorological events, nor are they able to be situated in an ideal medium due to logistical constraints. Therefore, rather than being placed in rock, seismic sensors may be placed in near-surface soil, and therefore, the propagation media are neither hard rock nor an isotropic Newtonian fluid (Aki and Richards 1980). For targeted temporary persistent monitoring situations, careful site selection is usually not possible, and the target of interest dictates sensor location. Currently, sensors are calibrated onsite for specific signals of interest. If the site conditions change or signals of interest change, extensive retraining or tuning may be required to avoid misclassification of signals or errors in localization. By understanding the near-surface attributes and characterizing how they change in different geologies, seismic signals may be predicted before installation. Therefore, the low-confinement soil continuum fabric behaviors play a critical role in the performance and signal processing of these temporary persistent monitoring arrays.

1.2 Overview

The purpose of this research is to show that that cohesionless soils exhibit significant soil fabric strength characteristics that are not captured by the standard internal friction angle definition.

1.2.1 Chapter 2: Experimentation

Chapter 2 begins with a description of the three cohesionless materials tested in this study: a poorly-graded sand (SP), a silty sand (SM), and a silt (ML). Specimen preparation methods are then detailed, as well as triaxial, simple shear, and cyclic ring shear testing protocols for confining pressures ranging from zero to 1,000 kPa. Three repetitions of each

triaxial and simple shear test condition were conducted, while 10 repetitions of each cyclic ring shear test were conducted.

1.2.2 Chapter 3: Results

Chapter 3 presents the analysis methods and results for each testing type. Average values are listed for each test condition. In total, 63 triaxial tests, 81 simple shear tests, and 50 cyclic ring shear tests were conducted. All materials exhibited shear strengths and stress paths in excess of expected failure surfaces at confining pressures under 100 kPa.

1.2.3 Chapter 4: Discussion

Chapter 4 contains a discussion of the implications of the findings, namely that the data imply that the governing mechanics in the near-surface environment are not simply controlled by the confining pressures and are more complex than approximated by Mohr-Coulomb mechanics. In all loading cases, there is a y-intercept (c') suggesting that even a non-plastic cohesionless material will retain some degree of internal structure even without confining pressures.

Of particular importance is the impact to sensor work as near-surface seismic sensors are placed within low-confinement environments. These data further imply departures from expected modulus values that impact signal-processing calculations.

The chapter concludes with a summary of the research findings.

1.2.4 Chapter 5: References

Chapter 5 contains the references cited within this technical report.

2 Experimentation

2.1 Material

The grain-size distributions of the cohesionless materials in this study are shown in Figure 1.

Figure 1. Grain-size distribution.

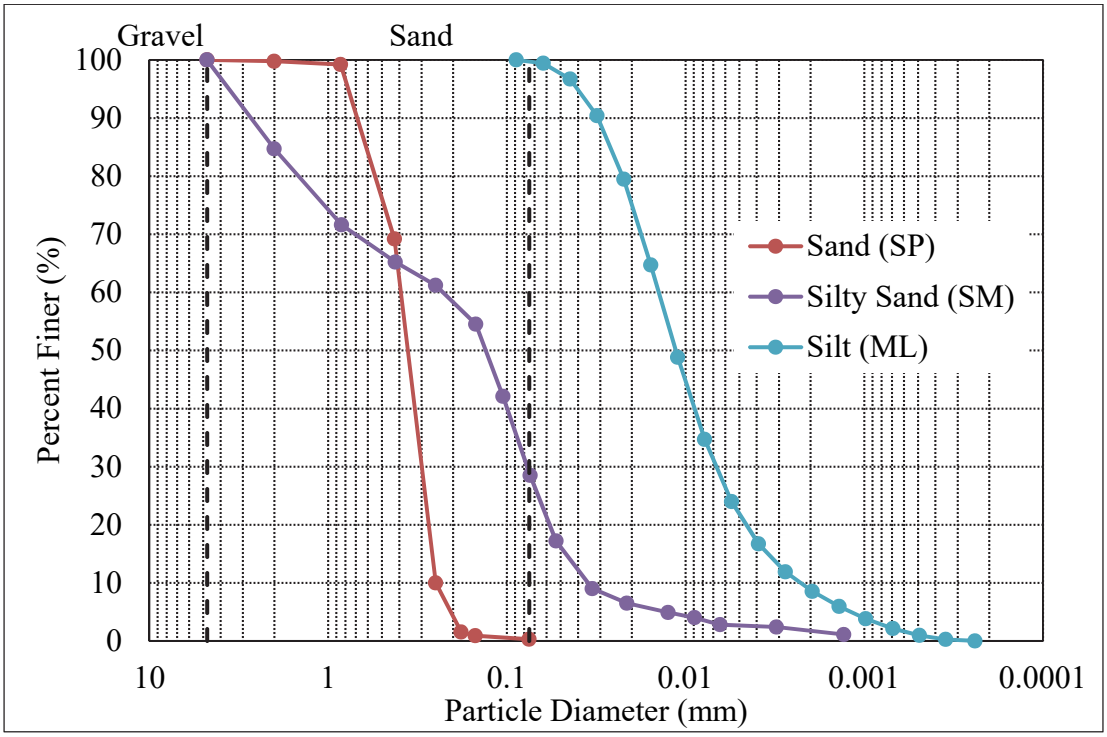

The sand is a washed, uniform, medium-to-fine beach sand (SP). The material is poorly graded with 90 percent of the material between 0.25 and 0.85 mm in diameter. The Coefficient of Uniformity is 1.52, reflecting the dominance of the No. 40 and No. 60 sieves in the grain-size distributions. The Coefficient of Curvature is 1.12. The specific gravity is 2.70.

The silty sand is a cohesionless engineered silty sand (SM) representative of known soils at Aberdeen Proving Grounds, MD. The soil consisted of 71.5 percent sand, 26.8 percent silt, and 1.7 percent clay. Atterberg limits tests classify the material as non-plastic (ASTM Standard D4318) (ASTM International 2010). The specific gravity is 2.78. High-pressure triaxial testing (confining pressures of 2.5 MPa to 200 MPa) of this material can be found in Graham et al. (2014).

The silt is a blended silt (ML) consisting of three natural Rhode Island silts. The liquid limit could not be determined rendering these silts as non-plastic (ASTM Standard D4318) (ASTM International 2010; Taylor 2011). A negligible presence of organic material was detected. The specific gravity of the silt is 2.75. Further information on this silt can be found in Taylor (2011).

2.2 Specimen preparation

Consistently tight tolerances during sample preparation are crucial to both replicate in-situ field conditions and ensure continuity across multiple reconstituted laboratory samples (Bradshaw and Baxter 2007; Taylor 2011; Taylor et al. 2016). Samples were reconstituted using a modified moist tamping procedure resulting in less than 2 percent difference in sample density and moisture content (Taylor 2011; Taylor et al. 2012; Taylor et al. 2016). These tolerances are stricter than ASTM laboratory procedures, thereby yielding highly repeatable samples with no appreciable fabric variance from reconstitution between specimens. Thus, observed effects at low-to-zero confining pressures are representative of fabric behavior and not artifacts of variation in sample preparation.

All samples were constructed at loose-to-medium density and dry of the optimal moisture content in accordance with Taylor et al. (2016), with modifications for UD (unconsolidated drained) and ICD (isotropic consolidated drained) specimens tested at 15-kPa confining pressure (Berry et al. 2018). Sand specimens were compacted to a density of 1.65 g/cc and water content of 5.66 percent. Silty sand specimens were compacted to a density of 1.76 g/cc and water content of 10.5 percent. Silt specimens were compacted to a density of 1.68 g/cc and water content of 12.8 percent.

Specimens were tested under isotropic consolidated-drained simple shear (ICD_{SS}), unconsolidated-drained simple shear (UD_{SS}), isotropic consolidated-drained triaxial (ICD_{TX}), and unconsolidated-drained triaxial (UD_{TX}) conditions with confining pressures between 0 kPa and 1,000 kPa.

2.3 Triaxial specimen preparation and testing protocol

Triaxial test specimens measured 71.9 mm in diameter by 145.0 mm in height. After compaction, the height was measured and the density calculated to ensure the target density was obtained. No vacuum pressure

was applied to specimens tested at or below 15-kPa confining pressure to prevent artificial granular movement.

- For UD_{TX} specimens: After the membrane was secured to the top platen, the mold was removed. The test cell was not used. The specimen valve was opened to the atmosphere creating drained conditions. Previous research showed no appreciable difference in shear strength for UD_{TX} specimens tested both with and without a 0.3-mm-thick latex membrane (Winters et al. 2016), so the membrane was left in place for ease of UD_{TX} testing for the sand and removed for the silty sand and silt.

All samples followed near-surface testing protocols (Berry et al. 2018) under an axial loading strain rate of 0.25 percent/min. Three repetitions of each test condition were conducted for a total of 21 tests per soil type. Figure 2 shows a typical UD_{TX} test specimen without a membrane before and after testing.

Figure 2. Typical UDTX test on SM specimen before (a) and after (b) testing.

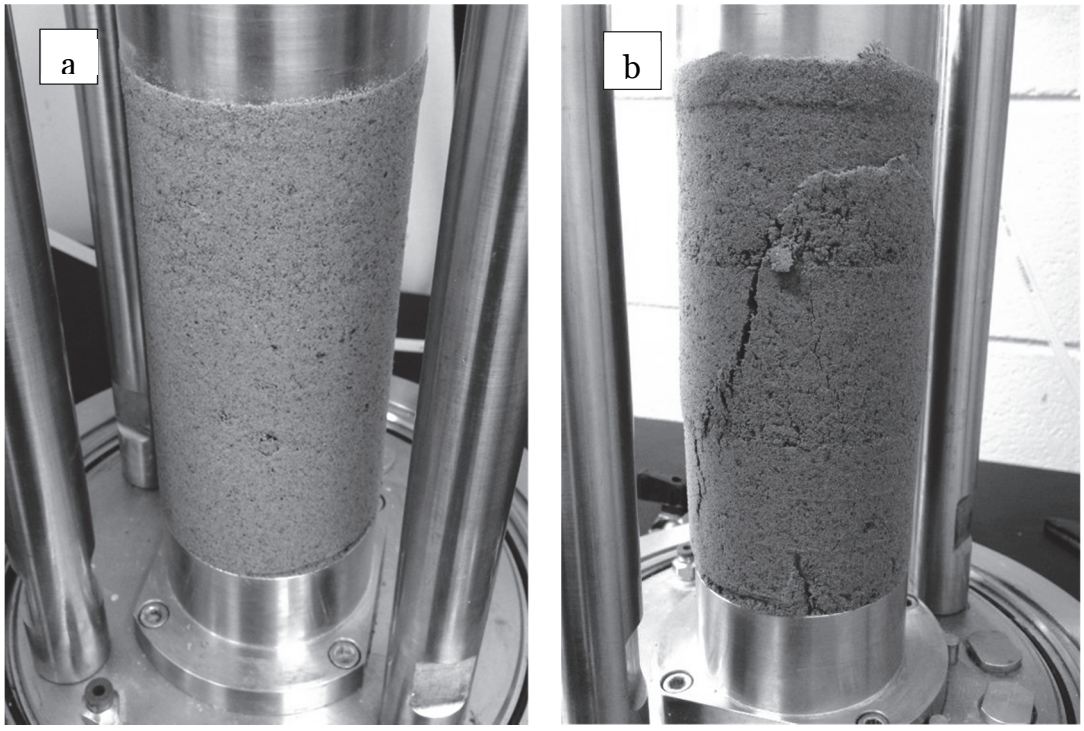

2.4 Simple shear specimen preparation and testing protocol

Simple shear specimens measured 72.9 mm in diameter by 32.0 mm in height. Simple shear specimens were constructed in one layer in accordance with Taylor et al. (2016) and Berry et al. (2018).

- For ICD_{SS} specimens tested at 25-kPa confining pressure or greater: A vacuum was applied to the sample, and the mold was removed. The test cell was secured and filled with water. A cell pressure of 25 kPa was applied, the vacuum was released opening the specimen to the atmosphere and creating drained conditions, and the test confining pressure was applied. A 5-kPa vertical seating pressure was applied.
- For ICD_{SS} specimens tested at 15 kPa confining pressure or less: No vacuum was applied to the sample. The mold was removed. The test cell was secured and filled with water. The specimen valve was opened to the atmosphere creating drained conditions, and the test confining pressure was applied. A 5-kPa vertical seating pressure was applied.
- For UD_{SS} specimens: No vacuum was applied to the sample. After the top platen was brought into contact with the specimen, the mold was removed. The test cell was not used. Samples were constructed using either a latex membrane or wax paper to line the construction mold. After the top platen was brought into contact with the specimen, the mold was removed, and the latex membrane or wax paper was carefully cut from the sample. Latex membranes were left in place for ease of UD_{SS} testing for the SP and removed for the SM and ML materials. One series of tests was conducted with a 5-kPa seating pressure and another series of tests at 2-kPa seating pressure to investigate the impact of the seating load on shear strength.

All samples were sheared at a strain rate of 0.25 percent/min (Berry et al. 2018). Three repetitions of each test condition were conducted for a total of 27 simple shear tests per soil type. Figure 3 shows a typical UD_{SS} test specimen without a membrane before and after testing.

Figure 3. Typical UDSS specimen before (a) and after (b) testing.

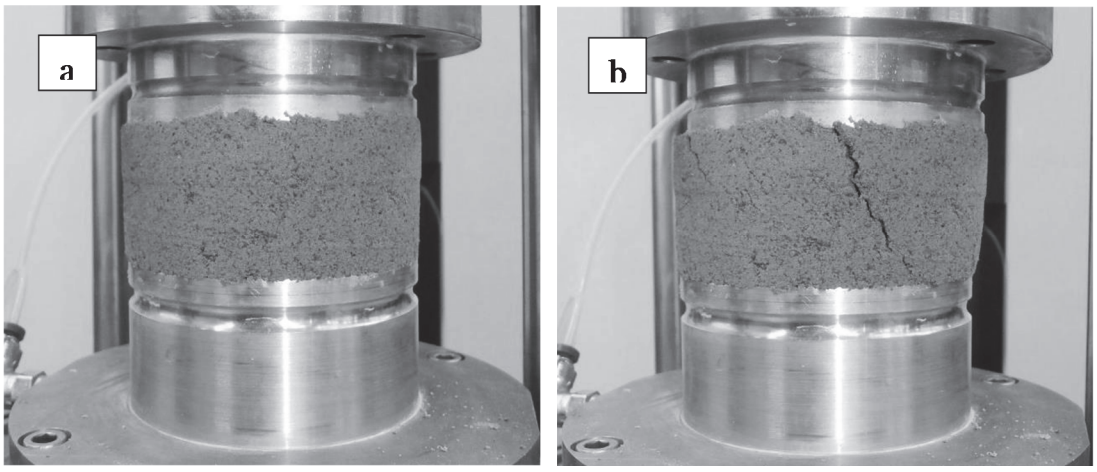

2.5 Cyclic ring shear

Cyclic ring shear specimens measured 150 mm in outer diameter, 100 mm in inner diameter, and 25 mm in height. Ring shear specimens were constructed in one layer in accordance with Taylor et al. (2016) and Berry et al. (2018).

After specimen construction and application of a seating load, the specimen was saturated in a water bath. The confining pressure was then increased to the test confining pressure. The specimen was held at the test confining pressure for 30 min before shearing.

During shearing, the confining pressure was held constant while the specimen was sheared using a sine wave form set to an amplitude of 2.5 mm and a frequency of 0.5 for a duration of 10 cycles (Berry et al. 2018). Ten repetitions of each test condition were conducted for a total of 50 cyclic ring shear tests on SP soil. Figure 4 shows a typical saturated, anisotropic-consolidated undrained cyclic ring shear ($ACU_{CYC,RS}$) test specimen after construction (a) and during saturation (b).

Figure 4. Typical $ACU_{CYC,RS}$ specimen after construction (a) and during saturation (b).

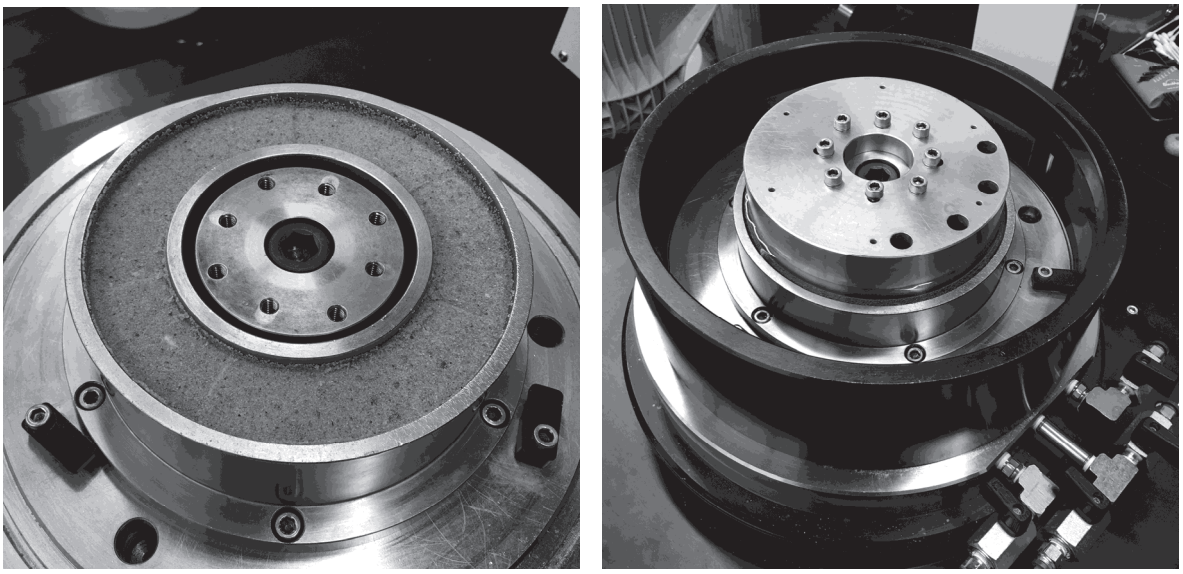

3 Results

The following sections contain a summary of the results of triaxial, simple shear, and cyclic ring shear testing. Details of each test are provided in the appendix.

3.1 Triaxial testing

Table 1 lists the confining pressures and average shear stresses at failure from the triaxial tests conducted for this study, for a total of 63 triaxial tests. Triaxial failure strength was determined at the point of maximum deviator stress.

Table 1. Triaxial testing summary for near-surface UD and ICD testing.

	Average shear stress at failure, kPa (n=3)		
Confining pressure	SP	SM	ML
UD	35	27	102
ICD 15 kPa	74	87	158
ICD 25 kPa	109	121	201
ICD 50 kPa	216	177	247
ICD 100 kPa	403	327	377
ICD 500 kPa	1560	1371	1225
ICD 1000 kPa	2304	2170	2018

The expected Mohr-Coulomb failure plane for each material was defined using test results of ICD_{TX} tests conducted with confining pressures of 100, 500, and 1,000 kPa, as shown in Figure 5 - Figure 7. A trendline was fit to the test results in p-q space assuming a cohesion intercept of zero, consistent with assumptions for granular materials (Lambe and Whitman 1969). These trendlines follow the form shown in Equation 2, with m set to zero (Das 2002).

$$q = m + p * tan\ (\alpha) \quad (2)$$

Which can be related back to traditional ϕ and c values of the form $\tau = c + \sigma * tan(\phi)$ using Equations 3 and 4 (Das 2002).

$$tan\,(\alpha) = sin\,(\phi) \quad (3)$$

$$m = c * cos\,(\phi) \quad (4)$$

The resulting friction angle, ϕ_f, was used for the subsequent analysis of the low-confinement test results.

Figure 5. SP high confinement triaxial testing.

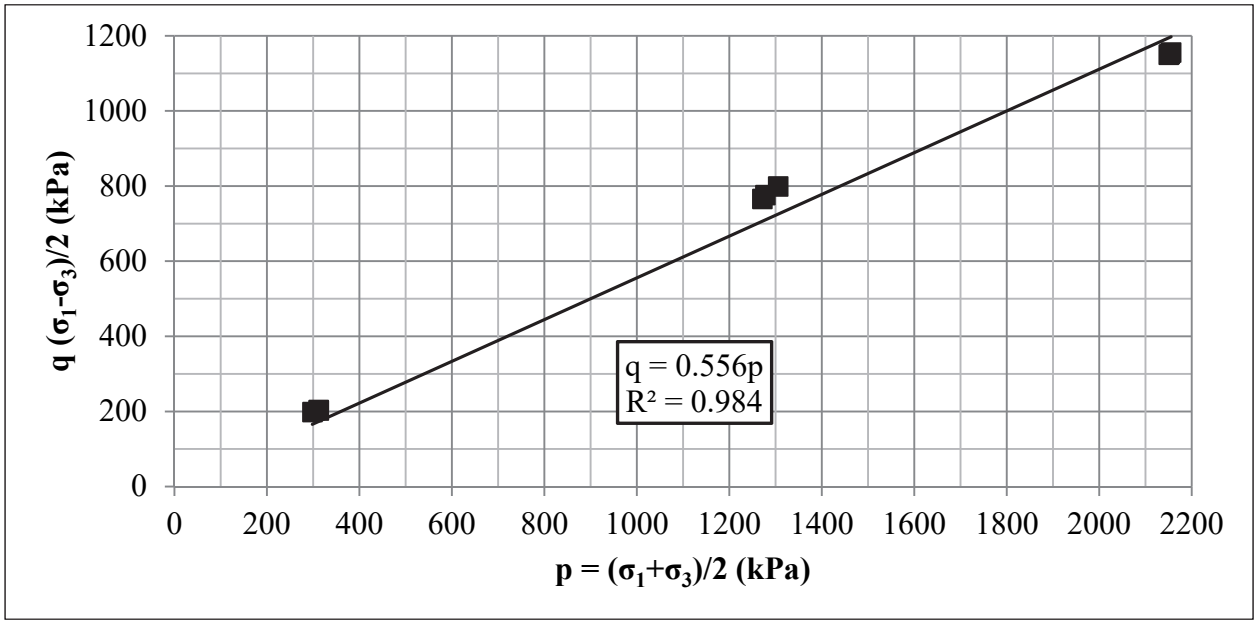

Figure 6. SM high confinement triaxial testing.

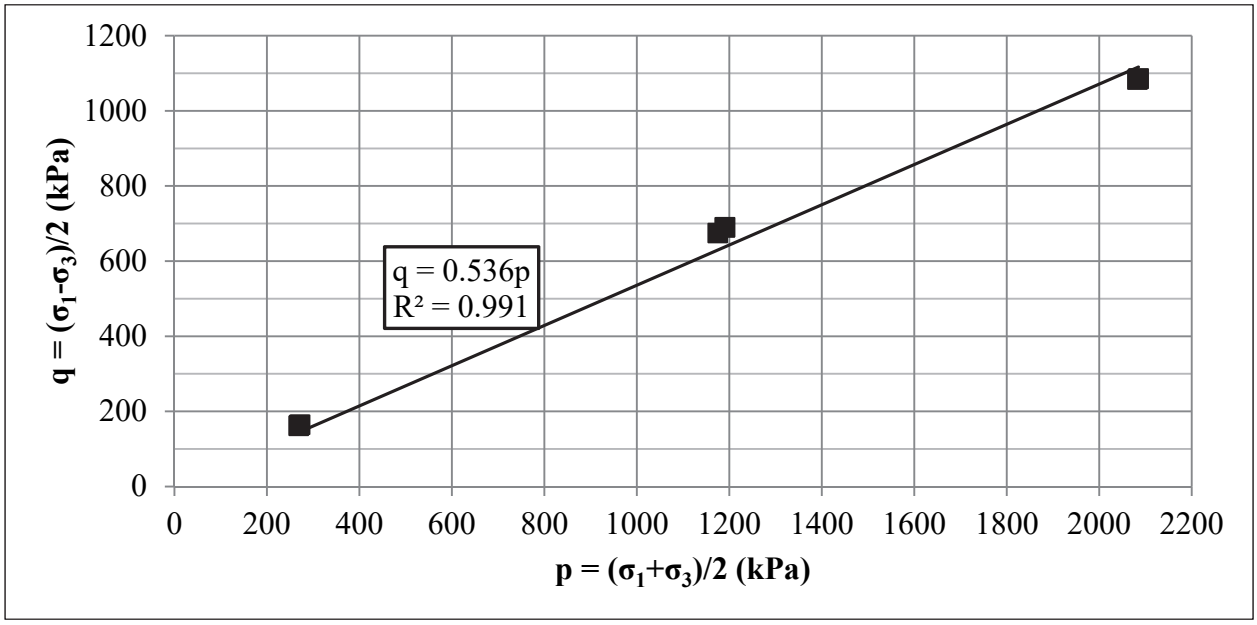

Figure 7. ML high confinement triaxial testing.

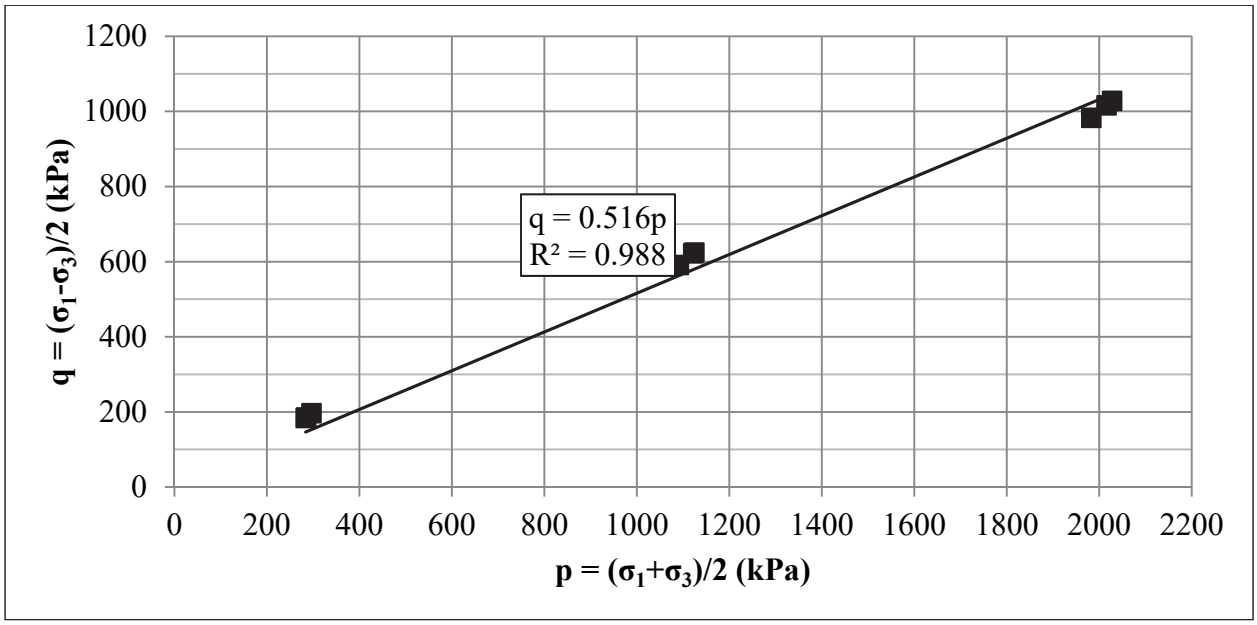

Figure 8 - Figure 10show the results of triaxial testing in p-q space for tests up to and including 50-kPa confining pressure. It can be seen that results of all of the triaxial tests plot above their respective theoretical failure envelopes. The dashed line represents the theoretical failure envelope expected from higher-confinement testing: ϕ_f = 33.8° for SP, ϕ_f = 32.4° for SM, and ϕ_f = 31.1° for ML. For each material, the test results under 50 kPa can better be represented by a steeper friction angle (ϕ_f,) and non-zero intercept (c) as calculated from Equations 3 and 4:

- SP- 38.9° line with a 6.05 kPa intercept.
- SM- 35.4° line with a 7.17 kPa intercept.
- ML- 36.5° line with a 27.2 kPa intercept.

Figure 8. SP triaxial results. Dashed line indicates the theoretical failure plane, and the solid line indicates the observational failure plane.

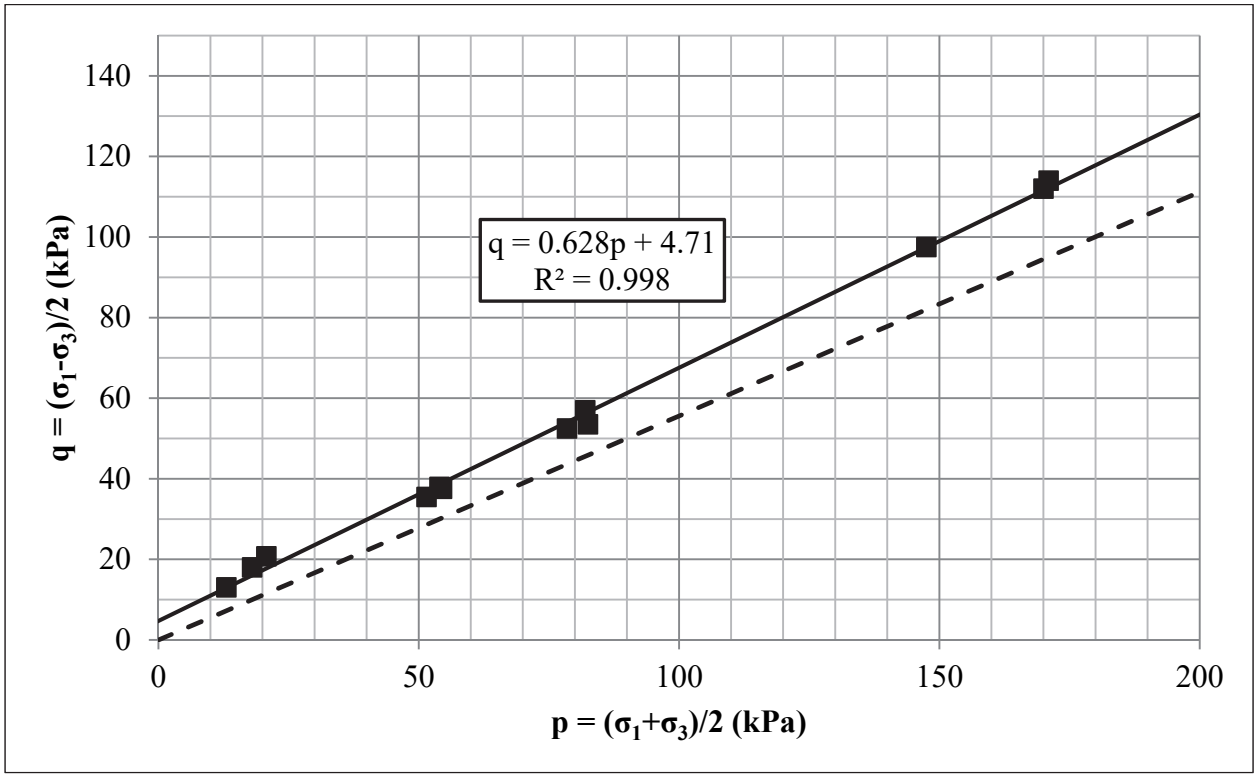

Figure 9. SM triaxial results. Dashed line indicates the theoretical failure plane, and the solid line indicates the observational failure plane.

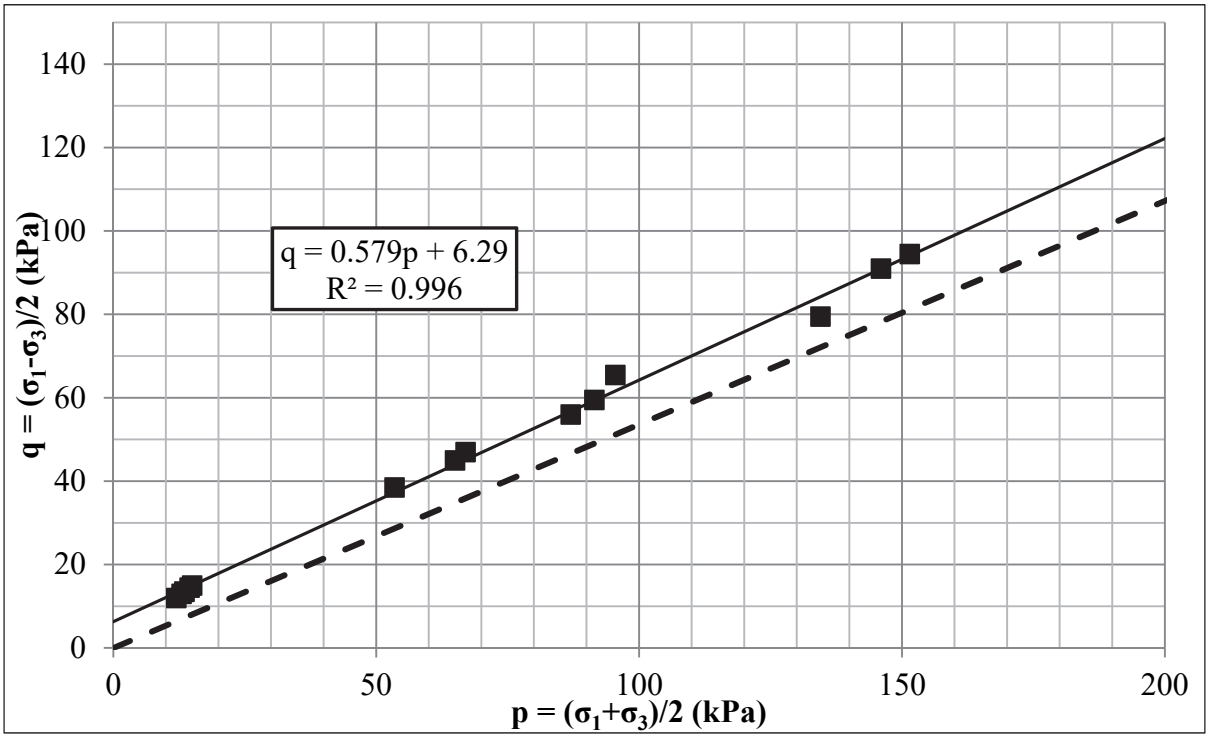

Figure 10. ML triaxial results. Dashed line indicates the theoretical failure plane, and the solid line indicates the observational failure plane.

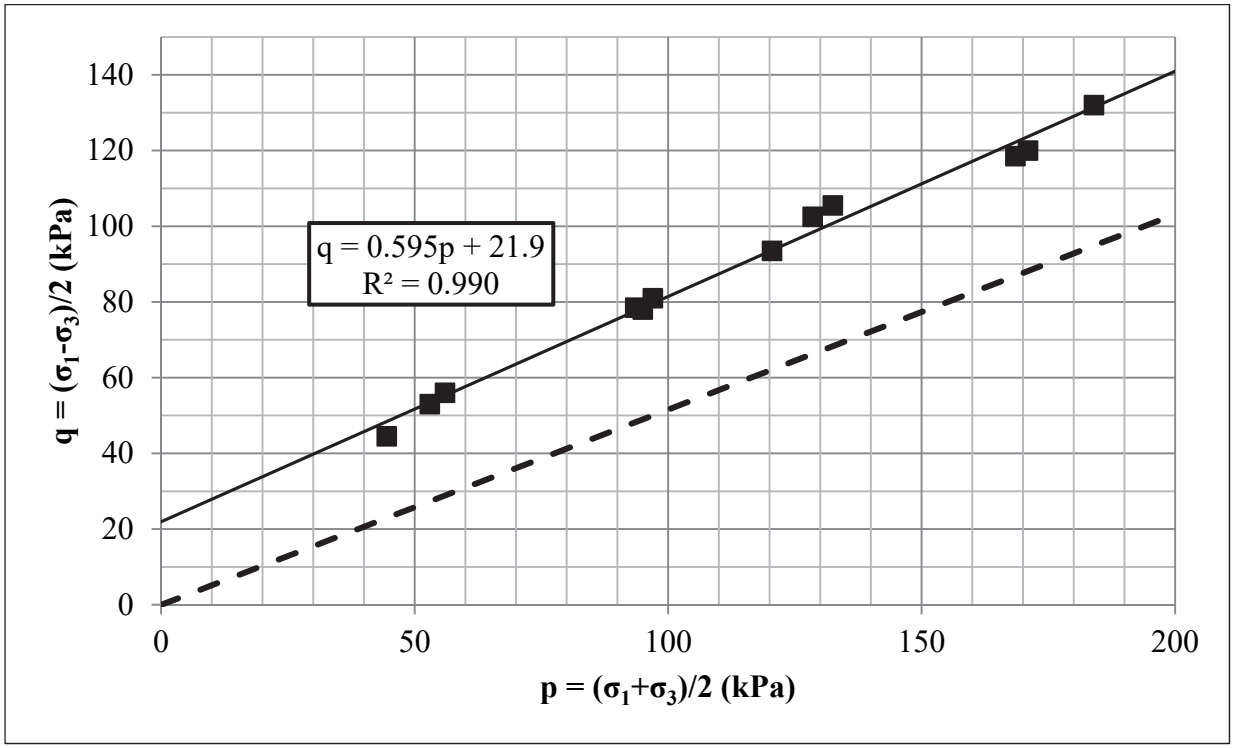

3.2 Simple shear

Table 2 lists the confining pressures and average shear stresses at failure from the simple shear tests conducted for this study, for a total of 81 simple shear tests. Simple shear failure strength was determined as the maximum shear stress at or below 3.5 percent shear strain for specimens tested at or below 100-kPa cell pressure, 7.5 percent shear strain for specimens tested at 250-kPa cell pressure, and 10.0 percent shear strain for specimens tested at 500-kPa cell pressure to correspond to observed plateauing of the shear stress relative to the shear strain.

Similar to the observations with the triaxial results, the failure envelope deviated from the theoretical failure plane at low confining pressures. Under near-surface confining pressures, the observational failure planes for the three materials can be best described by a second-order polynomials (R^2 = 0.981-0.988) that rejoin the theoretical failure envelope at or near 100 kPa.

Table 2. Simple shear testing summary for near-surface UD and ICD testing.

	Average shear stress at failure, kPa (n=3)		
Confining pressure	SP	SM	ML
UD, 2-kPa seating load	6.6	8.8	11.9
UD, 5-kPa seating load	7.4	10.8	14.5
ICD 15 kPa	16.1	22.5	19.0
ICD 25 kPa	23.4	31.3	26.0
ICD 50 kPa	45.4	39.3	38.4
ICD 75 kPa	57.3	55.2	49.1
ICD 100 kPa	64.7	64.4	56.4
ICD 250 kPa	176	160	142
ICD 500 kPa	305	301	266

For SP (Figure 11) and SM (Figure 12), the greatest difference between the theoretical plane and the observational envelope occur at about 50 kPa. The effects of the soil continuum fabric decrease with increasing confining pressure until the observational envelope rejoins the Mohr-Coulomb failure line at 100 kPa. For ML (Figure 13), the greatest difference between the theoretical plane and the observational envelope is seen when the soil is unconfined. The effects of the soil continuum fabric decrease with increasing confining pressure until the observational envelope joins the Mohr-Coulomb failure envelope between 75 and 100 kPa.

Figure 11. SP low confinement simple shear results.

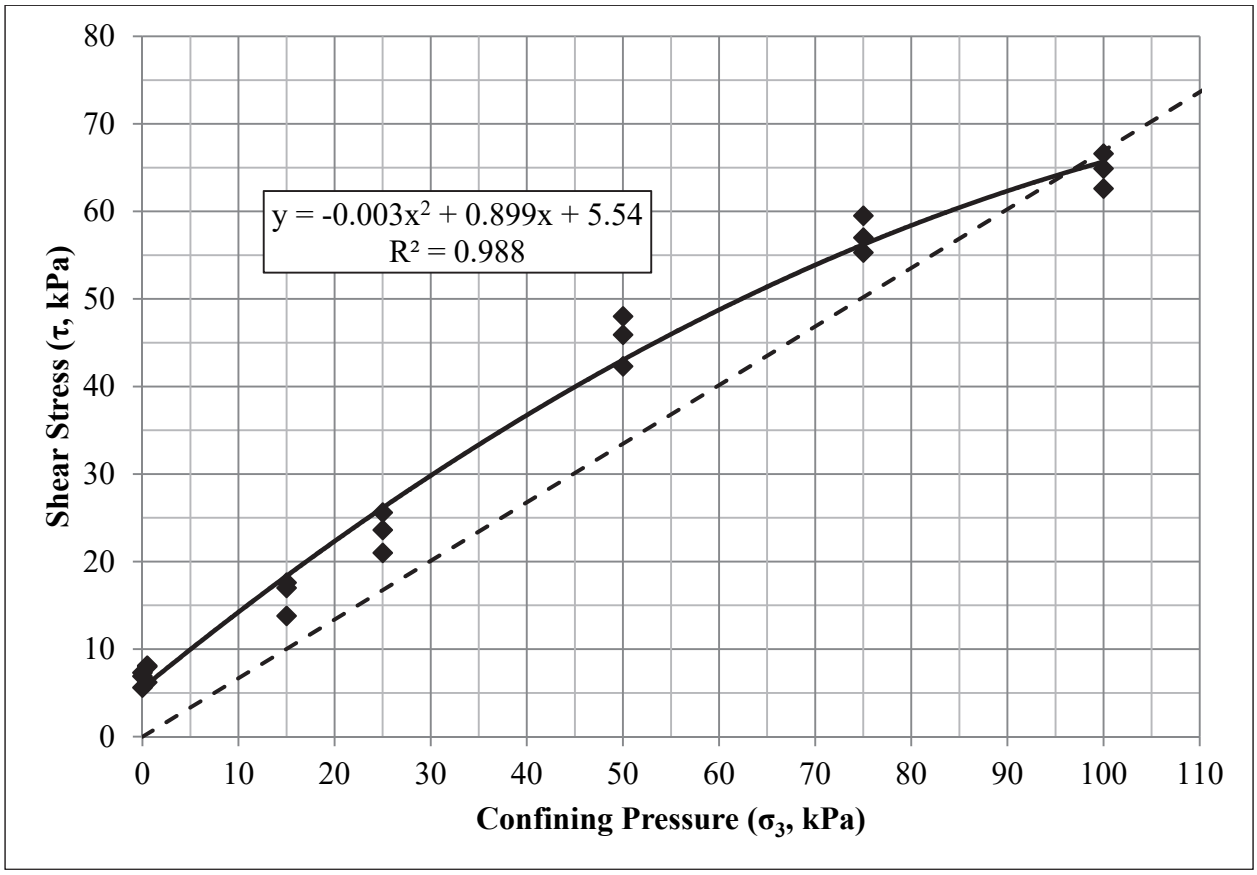

Figure 12. SM low confinement simple shear results.

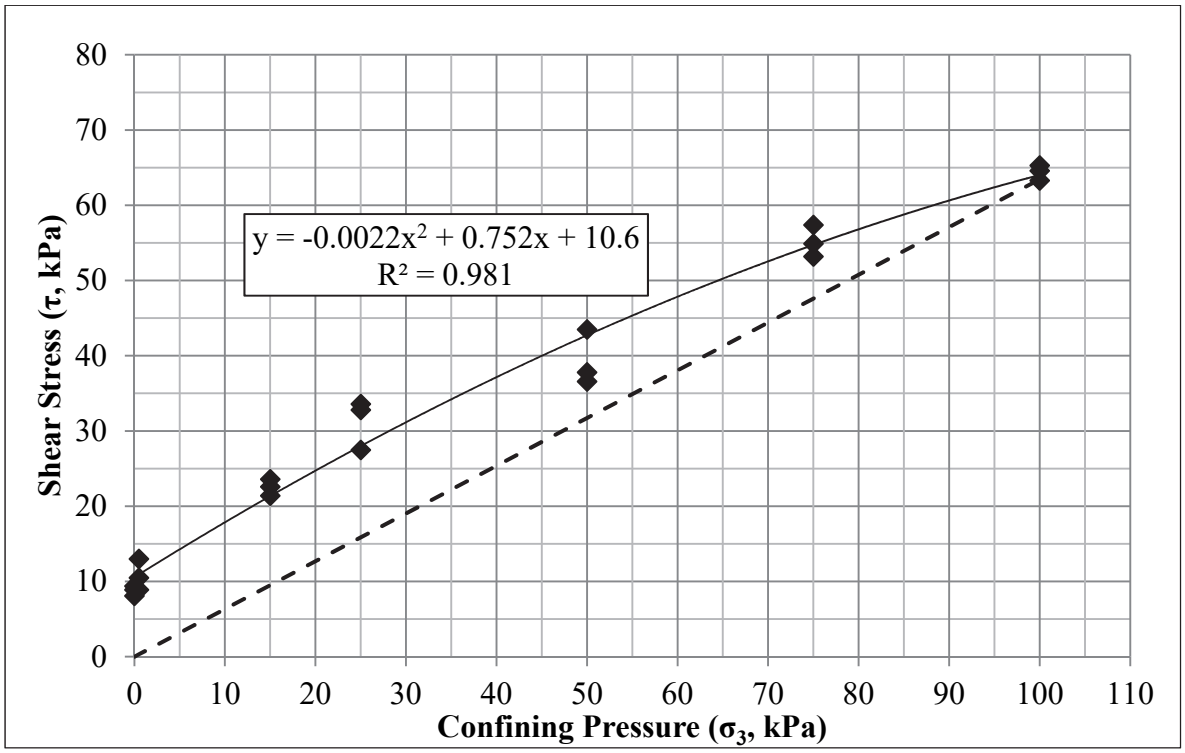

Figure 13. ML low confinement simple shear results.

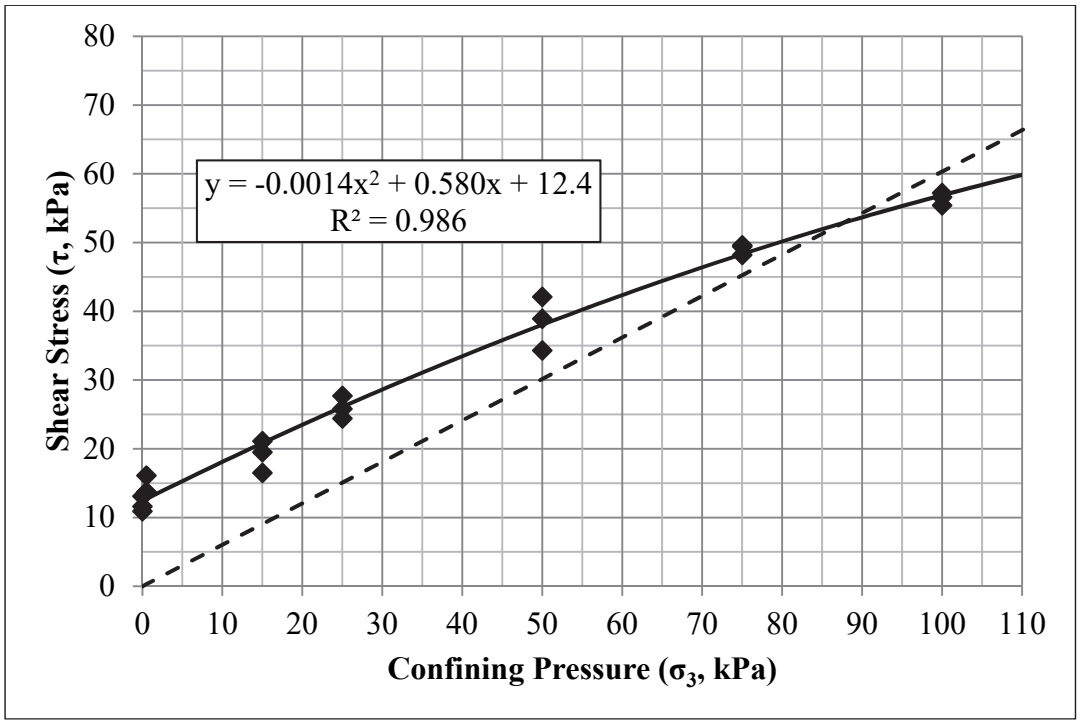

3.3 Cyclic ring shear

Table 3 lists the confining pressures, cyclic strain and shear stress at failure, and cyclic strain and shear stress at critical state from the SP cyclic ring shear tests performed for this study, for a total of 50 cyclic ring shear tests. Ten repetitions of each confining pressure were performed, and each test yielded both failure and critical state data. Failure strength was determined as the maximum shear stress and cyclic strain on the fourth cycle of testing. Critical state shear stress and cyclic strain were determined from the tenth cycle of testing.

Table 3. SP cyclic ring shear testing summary.

Confining pressure (kPa)	Failure		Critical state	
	Cyclic strain (%)	Shear stress (kPa)	Cyclic strain (%)	Shear stress (kPa)
10	0.213	16.86	0.211	20.64
25	0.212	31.29	0.211	38.17
50	0.213	50.38	0.210	60.51
75	0.212	69.40	0.210	81.18
100	0.212	86.29	0.210	99.83

Test data are plotted in Figure 14 and Figure 15. Both graphs show weak relationships between cyclic strain confining pressure. However, there are strong relationships between shear stress and confining pressure (R^2>0.96). Similar to triaxial and simple shear testing, these trendlines also contain non-zero intercepts.

Figure 14. SP cyclic ring-shear shear stress and cyclic strain at failure.

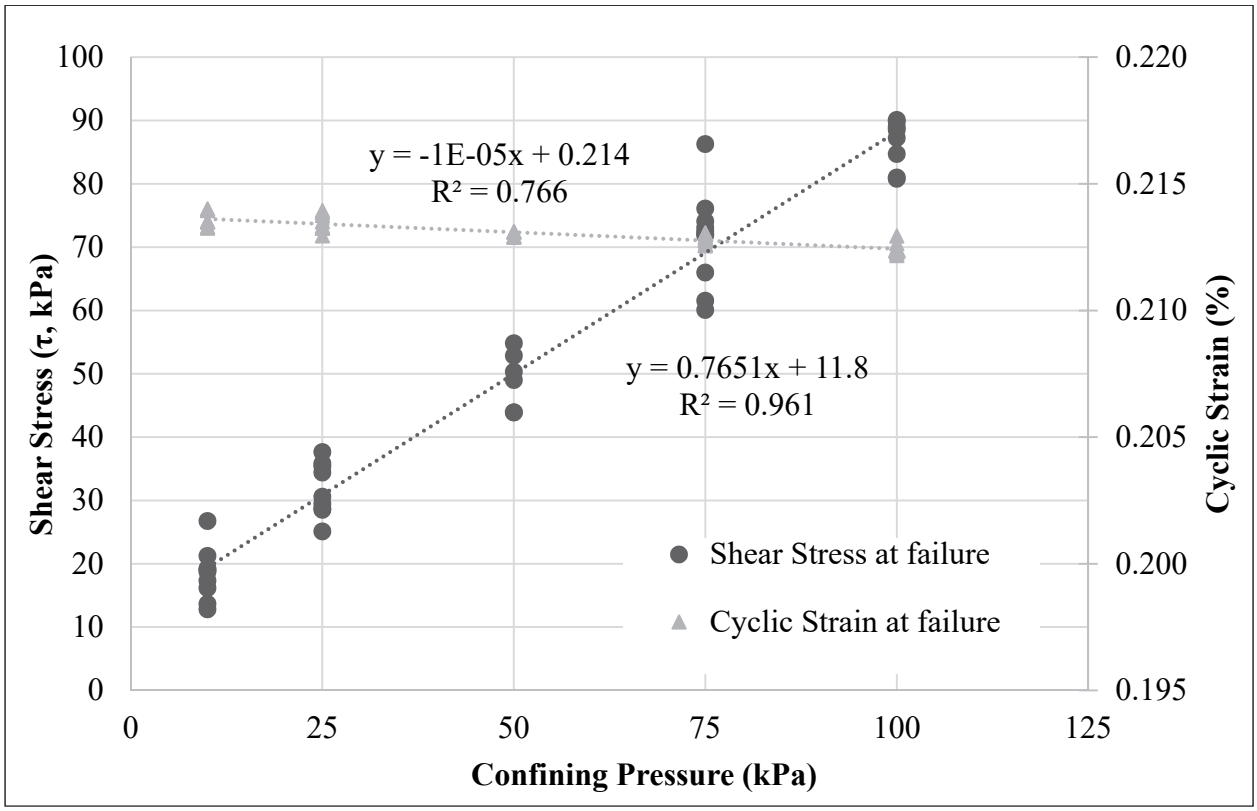

Figure 15. SP cyclic ring-shear shear stress and cyclic strain at critical state.

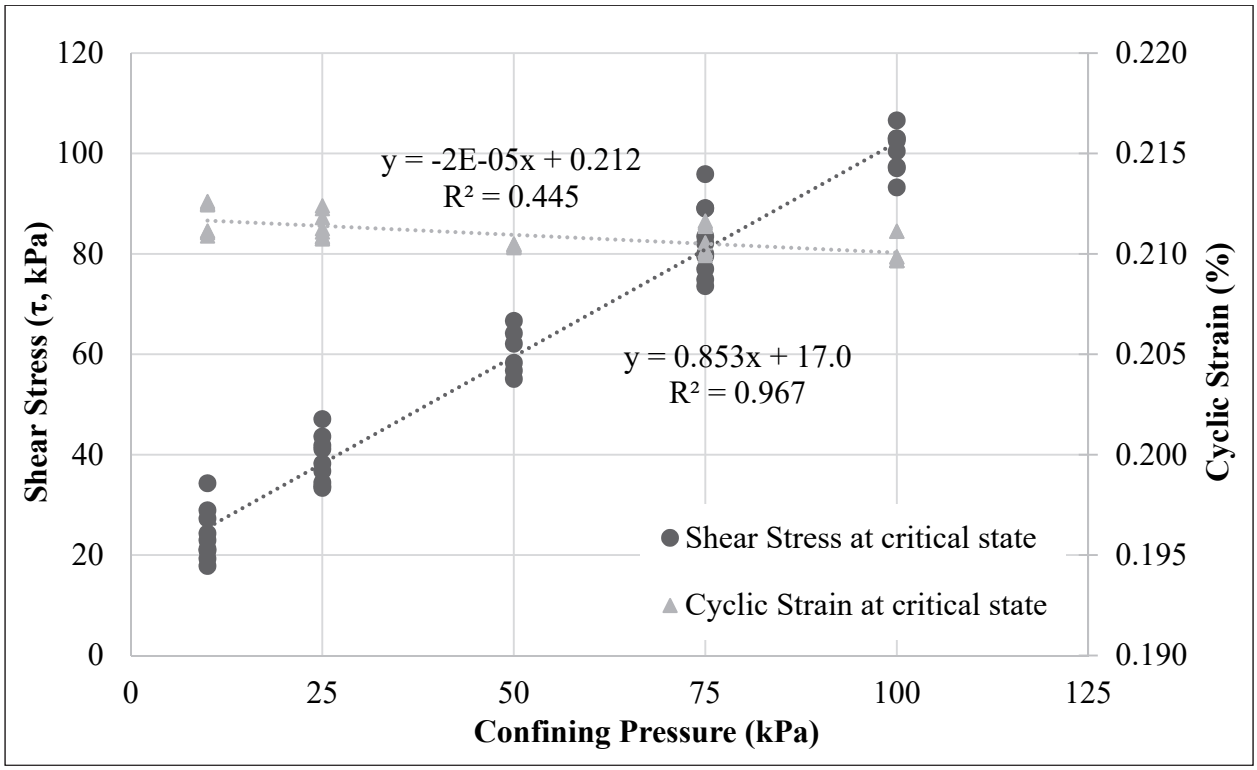

4 Discussion

The data indicate that cohesionless soils exhibit some strength due to the internal structure, not captured by the standard internal friction angle definition, as evidenced by the shear stress intercept of the trendlines. The variance in friction angle between the theoretical Mohr-Coulomb and observed data for axial loading conditions is relatively minor, 3 to 5 deg, and therefore would often be ignored in most geotechnical problems. This minor deviation in ϕ suggests that other failure mechanics that are influencing the overall strength are not captured in conventional Mohr-Coulomb failure plane derivation at near-surface conditions. At higher confining pressures, the data trend to the theoretical Mohr-Coulomb failure plane. This implies that the internal frictional component ϕ dominates the continuum strength and the inter-granular fabric contribution is negligible. However, under low confinement, the continuum fabric dominates the angle of the Mohr envelope.

Triaxial and simple shear tests are designed to test soil under different conditions and therefore yield different results, but the two can be compared (Budhu 1984). The data show that the soil continuum fabric, akin to cohesion in clays, dominates the shear resistance of the material for confining pressures below 100 kPa. At confining pressures above 100 kPa, the observational and theoretical Mohr-Coulomb failure planes are generally identical for simple shear. This implies that the internal friction caused by the confining pressure, not the internal fabric, provides the continuum strength. Additionally, this suggests that the contributing factors in near-surface failure mechanics is not well understood.

Of significant interest is the difference in the shape of the Mohr envelope between axial and shear loading. The linear nature of the axial loading is similar to the frictional roughness of quartz minerals and surface water tension. However, the non-linear behavior in shear loading implies that the fabric behavior, which dominates the soil strength in low-confinement regions, cannot be inferred by linear approximations and is far more complex mechanically.

The $ACU_{CYC,RS}$ data showed similar behavior to failure as both the triaxial and simple shear results, wherein at low confining stresses (less than 100 kPa), there is an increase over expected Mohr-Coulomb mechanics. Post failure, the SP material exhibited a small strain hardening increase in

shear stress to the critical state. While the magnitude of this increase is relatively minor, it represents a significant statistical increase (nearly 50 percent increase at no confinement) that is otherwise unaccounted for in the typical assumption of Mohr-Coulomb governance. As with the triaxial and simple shear results, the $ACU_{CYC,RS}$ critical state data imply that the governing mechanics in the near-surface environment are not simply controlled by the confining pressures and are more complex than approximated by Mohr-Coulomb mechanics.

In all loading cases, there is a *y*-intercept (*c*') suggesting that even a non-plastic cohesionless material will retain some degree of internal structure even without confining pressures. The magnitude of the *y*-intercept is relatively independent of the method of loading. This implies that the initial fabric strength is an intrinsic soil property, i.e., a function of the size of the grains and the ability of the granular friction to resist gravitational forces at the particle level, but is behaviorally variable as a function of both confining pressure and loading mechanism.

4.1 Sensor implications

While traditional geotechnical engineering often neglects near-surface soil behavior, it becomes critical in certain applications, including soil-sensor performances. These findings are particularly important as they relate to soil modulus values. The dynamic shear modulus is the principal soil property for evaluating wave propagation and dynamic response of soils. Although studies of dynamic soil properties within the laboratory environment, such as resonant column testing, have been performed for several decades, the effects of saturation, particle size and shape, gradation, and matrix suction were not investigated until the early 1980s (Wu et al. 1984; Qian et al. 1991; Wheeler et al. 2003; Biglari et al. 2012). Further, very little research has been performed on anisotropic shear moduli for unsaturated soils (Ng and Yung 2008; Ng et al. 2009). The near-surface stress-state is not considered in these recent studies where the effects of the internal soil continuum fabric-structure have a more significant role in soil behavior and soil-structure interactions, e.g., the effects of near-surface conditions on geophysical system performance.

The magnitude of hysteretic damping, or signal loss, is controlled through volumetric and distortional elastic deformations, which are governed by the bulk (*K*) and shear (*G*) moduli (Wood 1990). In the case of non-linear elastic materials such as soil, as the fabric yields, degradation of *G* occurs,

and energy is lost through hysteretic damping. Over the past four decades, extensive research into determining accurate magnitudes of *G* has shown that the shear modulus is dependent on four main factors: (1) mean confining pressure (σ'_m); (2) strain amplitude; (3) void ratio; and (4) in dry and water-saturated sands, *G* is not influenced by the oscillating frequencies up to 100 Hz (Hardin and Richart 1963; Seed and Idriss 1970; Richart et al. 1970; Hardin and Drnevich 1972; Iwasaki et al. 1974; Tatsuoka et al. 1978; Seed et al. 1986; Bolton and Wilson 1990). None of these studies investigated the low confining environments of the near surface yet are used to infer behavior.

For monotonic axial strength, none of the materials rejoin the Mohr-Coulomb failure line until the confining pressures exceed the depths of sensor placement. This would signify an increase in bulk modulus, *K*. However, in shear, the material rejoins the Mohr-Coulomb failure line much sooner. This illustrates a non-linearity between the shear modulus, *G*, and the bulk modulus, *K*, relationship within the near-surface environment. This *G-K* relationship has first-order impact on signal processing and sensor performance and can explain, in part, the phenomena observed in Taylor et al. (2014). These impacts are not limited to sensor performance, as internal erosion, dam and levee sloughing, and environmental contamination cap designs are all influenced by near-surface soil behavior.

4.2 Summary

The near-surface, low-confinement environment has been largely ignored by geotechnical engineers. Classic theories, such as Mohr-Coulomb failure mechanics and the presumption that cohesionless materials have no unconfined strength, do not hold true when subjected to detailed study. Namely, triaxial and simple shear testing of three materials (SP, SM, and ML) at confining pressures under 100 kPa showed significant increases in strength over the expected strengths from Mohr-Coulomb failure mechanics.

Lambe and Whitman (1969) acknowledge that the difference between the observational failure envelope and the theoretical failure plane can be small (less than 5 deg) and therefore insignificant for many applications. However, these studies were conducted predominately with triaxial and direct shear devices. The direct shear apparatus forces a horizontal failure plane while the simple shear apparatus allows the soil to fail along a true

failure plane. Therefore, to study shear loading at low confinement, simple shear testing was performed.

In respect to triaxial testing, the variance from the theoretical is relatively minor and follows a failure envelope in accordance with the mineralogical granular friction angle. However, in simple shear testing, it is evident that the internal fabric behavior dominates the shear resistance in low-confining-stress environments. Moreover, the shape of the simple shear failure envelope is non-linear and significantly stronger than the theoretical limit of Mohr-Coulomb mechanics for a cohesionless material. In both the triaxial and simple shear cases, the internal unconfined fabric strengths are in relatively close agreement for each material. This suggests that, in near-surface or low-confinement regions, cohesionless materials behave similarly to overly-consolidated clays, just at a reduced cohesion value. While the SM material did contain 1.7 percent clay, the clay fraction is insufficient to influence the activity of the soil. Additionally, this clay fraction does not yield a plastic limit as defined in ASTM Standard D4318 (ASTM International 2010). The significant difference in the Mohr envelope shape illustrates that the internal fabric's ability to resist different loading mechanisms cannot be assumed by a linear approximation. However, the boundaries and physics of these observations, as well as further study into changes in soil moduli, are the subject of ongoing research.

References

Aki, K., and P.G. Richards. 1980. *Quantitative seismology: Theory and methods, vols. I and II*. San Francisco: W.H. Freeman.

ASTM International. 2010. *Standard test methods for liquid limit, plastic limit, and plasticity index of soils*. Designation: D4318. West Conshohocken, PA: ASTM International.

Berry, W.W., O.-D.S. Taylor, K.E. Winters, A.L. Cunningham, W.R. Rowland, and M.D. Antwine. 2018. *Near surface laboratory testing protocol development*. ERDC/GSL TR-18-12. Vicksburg, MS: U.S. Army Engineer Research and Development Center.

Biglari, M., A. d'Onofrio, C. Mancuso, M.K. Jafari, A. Shafiee, and I. Ashayeri. 2012. Small-strain stiffness of Zenoz kaolin in unsaturated conditions. *Canadian Geotechnical Journal* 49: 311-322.

Bolton, M.D., and J.M.R. Wilson. 1990. Soil stiffness and damping. In Structural dynamics, ed. Kratzig et al., 209-216. Balkema, Rotterdam.

Bonner, J., R. Waxler, Y. Gitterman, and R. Hofstetter. 2013. Seismo-acoustic energy partitioning at near-source and local distances from the 2011 sayarim explosions in the Negev Desert, Israel. *Bulletin of the Seismological Society of America* April 2013. 103 (2A): 741-758.

Bradshaw, A., and C. Baxter. 2007. Sample preparation of silts for liquefaction testing. *Geotech. Testing Journal 30*(4): 324.

Budhu, M. 1984. On comparing simple shear and triaxial test results. *J. of Geotech. Engineering 110*(12): 1809-1814.

Chapman, M. April 2013. On the rupture process of the 23 August 2011 Virginia Earthquake. *Bulletin of the Seismological Society of America* 103(2A): 613-628.

Das, B.M. 2002. *Principles of Geotechnical Engineering*. Pacific Grove, CA: Brooks/Cole.

Fannin, R.J., A. Eliadorani, and J.M.T. Wilkinson. 2005. Shear strength of cohesionless soils at low stress. *Geotechnique 55*(6): 467-478.

Graham, S.S., S.A. Akers, K.J. Ratliff, and T.A. Waddell. 2014. *Laboratory characterization of Aberdeen test center engineered roadway soil*. ERDC/GSL TR-14-36. Vicksburg, MS: U.S. Army Engineer Research and Development Center.

Hardin, B.O., and V.P. Drnevich. 1972. Shear modulus and damping in soils: Design equations and curves. *Journal of the Soil Mechanics and Foundation Division* (ASCE) 98 (SM7): 667-692.

Hardin, B.O., and F.E. Richart. 1963. Elastic wave velocities in granular soils. *Journal of the Soil Mechanics and Foundation Division* (ASCE) 89: 33-65.

Huang, Y., H. Cheng, T. Osada, A. Hosoya, and F. Zhang. 2015. Mechanical behavior of clean sand at low confining pressure: Verification with element and model tests. *J. of Geotech*. and Geoenvironmental Engineering 06015005-1-06015005-6.

Iwasaki, T., F. Tatsuoka, and Y. Takagi. 1974. Shear moduli of sands under cyclic torsional shear loading. *Soils and Foundations* (JSSMFE) 18(1:39-56).

Koper, K.D., T.C. Wallace, and R.C. Aster. 2003. Seismic recordings of the Carlsbad, New Mexico, pipeline explosion of 19 August 2000. *Bulletin of the Seismological Society of America* 93(4): 1427-1432.

Koustuvee, K., A. Sridharan, and M. Chetia. 2014. Investigation into the influence of grain shape and size on shear strength of cohesionless soils. Proc. GeoCongress 2014, GSP 234, ASCE, Atlanta, GA: 84-92.

Lambe, T.W., and R.V. Whitman. 1969. Soil mechanics. New York: John Wiley & Sons.

Lancelot, L., I. Shahrour, and M. Al Mahmoud. 2006. Failure and dilatancy properties of sand at relatively low stresses. *J. of Engineering Mechanics* 132(12): 1396-1399.

Mitchell, J.K., and K. Soga. 2005. Fundamentals of soil behavior. Hoboken, NJ: John Wiley & Sons.

Mykkeltveit, S., F. Ringdal, T. Kvoerna, and R.W. Alewine. 1990. Application of regional arrays in seismic verification. *Bulletin of Seismological Society of America* 80b: 1777-1800.

Ng, C.W.W., and S.Y. Yung. 2008. Determination of the anisotropic shear stiffness of an unsaturated decomposed soil. *Geotechnique* 58(1): 23-35.

Ng, C.W.W., J. Xu, and S.Y. Yung. 2009. Effects of wetting-drying and stress ratio on anisotropic stiffness of an unsaturated soil at very small strains. *Canadian Geotechnical Journal* 46: 1062-1076.

Qian, X., D.H. Gray, and R.D. Woods. 1991. Resonant Column Tests on Partially Saturated Sands. *Geotechnical Testing Journal* GTJODJ 14(3): 266-275.

Richart, F.E., J.R. Hall, and R.D. Woods. 1970. Vibrations of soil and foundations. Englewood Cliffs, NJ: Prentice-Hall Inc.

Ringdal, F., and E.S. Husebye. 1982. Application of arrays in the detection, location, and identification of seismic events. *Bulletin of the Seismological Society of America* 72(6): S201-S224.

Seed, H.B., and I.M. Idriss. 1970. Soil moduli and damping factors for dynamic response analysis. Report No. EERC 70-10. Berkeley, CA: Earthquake Engineering Research Center, University of California.

Seed, H.B., R.T. Wong, I.M. Idriss, and K. Tokimatsu. 1986. Moduli and damping factors for dynamic analyses of cohesionless soils. *Journal of Geotechnical Engineering* (ASCE) 112(11): 1016-1032.

Sheriff, R.E., and L.P. Geldhart. 1995. Exploration seismology, second edition. New York: Cambridge University Press.

Stump, B.W., D.C. Pearson, and R.E. Reinke. 1999. Source comparisons between nuclear and chemical explosions detonated at Rainier Mesa, Nevada Test Site. *Bulletin of the Seismological Society of America* 89(2)409-422.

Tatsuoka, F., T. Iwasaki, and Y. Takagi. 1978. Hysteretic damping of sands under cyclic loading and its relation to shear modulus. *Soils and Foundations* (JSSMFE) 18(2): 25-40.

Taylor, O.-D. S. 2011. Use of an energy-based liquefaction approach to predicting deformation in silts due to pile driving. PhD diss., University of Rhode Island, 303 p.

Taylor, O.-D.S., C.D. Baxter, A.S. Bradshaw, and A.C. Morales. 2012. New density normalization approach for evaluation of the cyclic resistance of silts. *GeoCongress* 2012 (809-818).

Taylor, O.-D.S., M.H. McKenna, J.R. Kelley, B.G. Quinn, and J. McKenna. 2014. Partially saturated soil causing significant variability in near surface seismic signals. *Near Surface Geophysics* 12(4): 467-480.

Taylor, O.-D.S, W.W. Berry, K.E. Winters, W.R. Rowland, M.D. Antwine, and A.L. Cunningham. 2016. Protocol for cohesionless sample preparation for physical experimentation. ERDC/GSL Technical Report TR-16-11. Vicksburg, MS: U.S. Army Engineer Research and Development Center.

Tsoflias, G.P., D.W. Steeples, G.P. Czarnecki, S.D. Sloan, and R.C. Eslick. 2006. Automatic deployment of a 2-D geophone array for efficient ultra-shallow seismic imaging. *Geophys. Res. Lett.* 33: L09301.

Wheeler, S.J., R.S. Sharma, and M.S.R. Buisson. 2003. Coupling of hydraulic hysteresis and stress-strain behavior in unsaturated soils. *Geotechnique* 53(1): 41-54.

Winters, K.E., O.-D.S. Taylor, W.W. Berry, W.R. Rowland, M.D. Antwine, and A.L. Cunningham. 2016. Cohesionless soil fabric and shear strength at low confining pressures. ASCE GeoChicago.

Wood, D.M. 1990. Soil behaviour and critical state soil mechanics. New York: Cambridge University Press.

Wu, S., D.H. Gray, and F.E. Richart. 1984. Capillary effects on dynamic modulus of sands and silts. *Journal of the Geotechnical Engineering Division* (ASCE) 110 (GT9): 1188-1203.

Appendix A: Test Data

Triaxial test data

SP triaxial test data

Target Cell Pressure (kPa)	Cell Pressure at σ_d Max (kPa)	Maximum Deviator Stress (σ_d, kPa)	Test Name
1000	1000	2311	20150722 A
1000	1001	2303	20150722 C
1000	1001	2299	20150916 B
500	506	1531	20150724 A
500	507	1598	20150724 B
500	502	1552	20150916 A
100	108	408	20150617 A
100	110	405	20150630 A
100	100	397	20150706 A
50	58	224	20150729 A
50	57	228	20150730 A
50	50	195	20150921 A
25	26	105	20150921 B
25	25	114	20150922 A
25	29	107	20150922 B
15	16	71	20150923 A
15	16	76	20150928 A
15	17	75	20150928 B
0	0	26	20150929 A
0	0	36	20150929 B
0	0	42	20150929 C

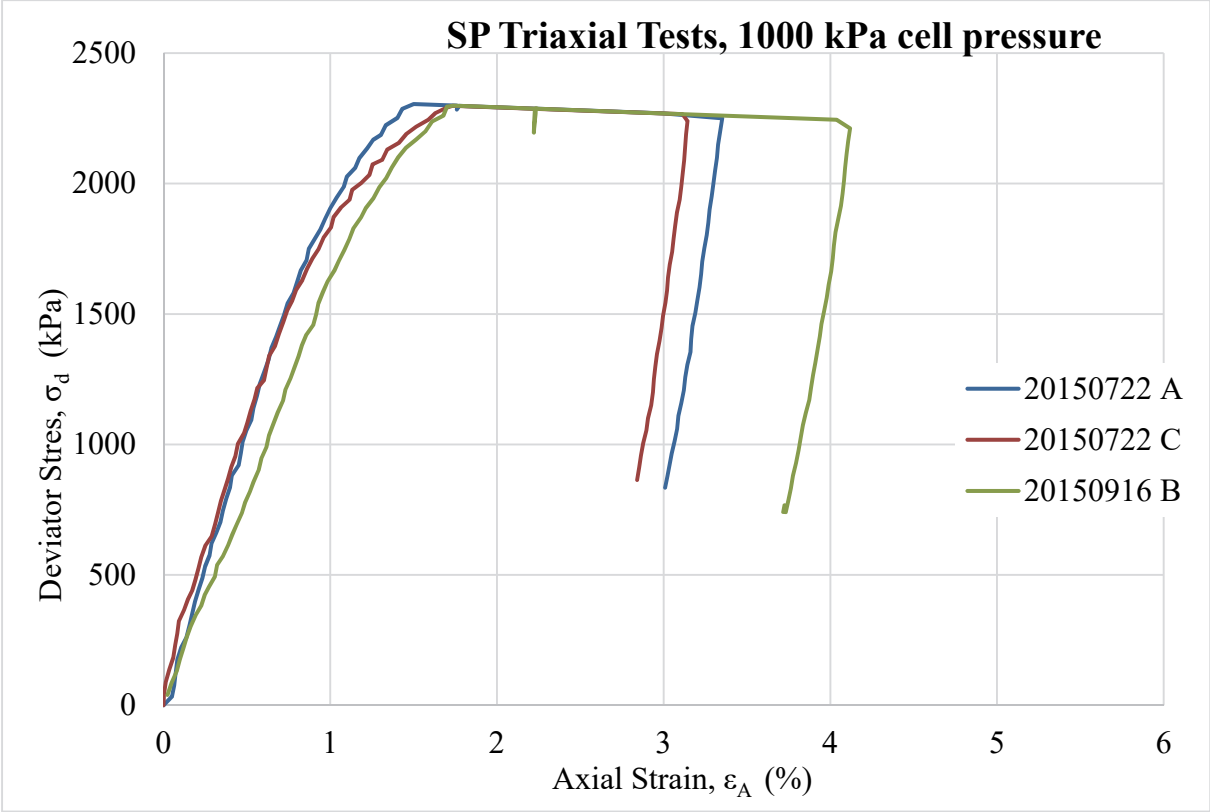
SP Triaxial Tests, 1000 kPa cell pressure
Deviator Stres, σd (kPa)
2500
2000
1500
1000
500
0
0
1
2
3
4
5
6
Axial Strain, εA (%)
20150722 A
20150722 C
20150916 B

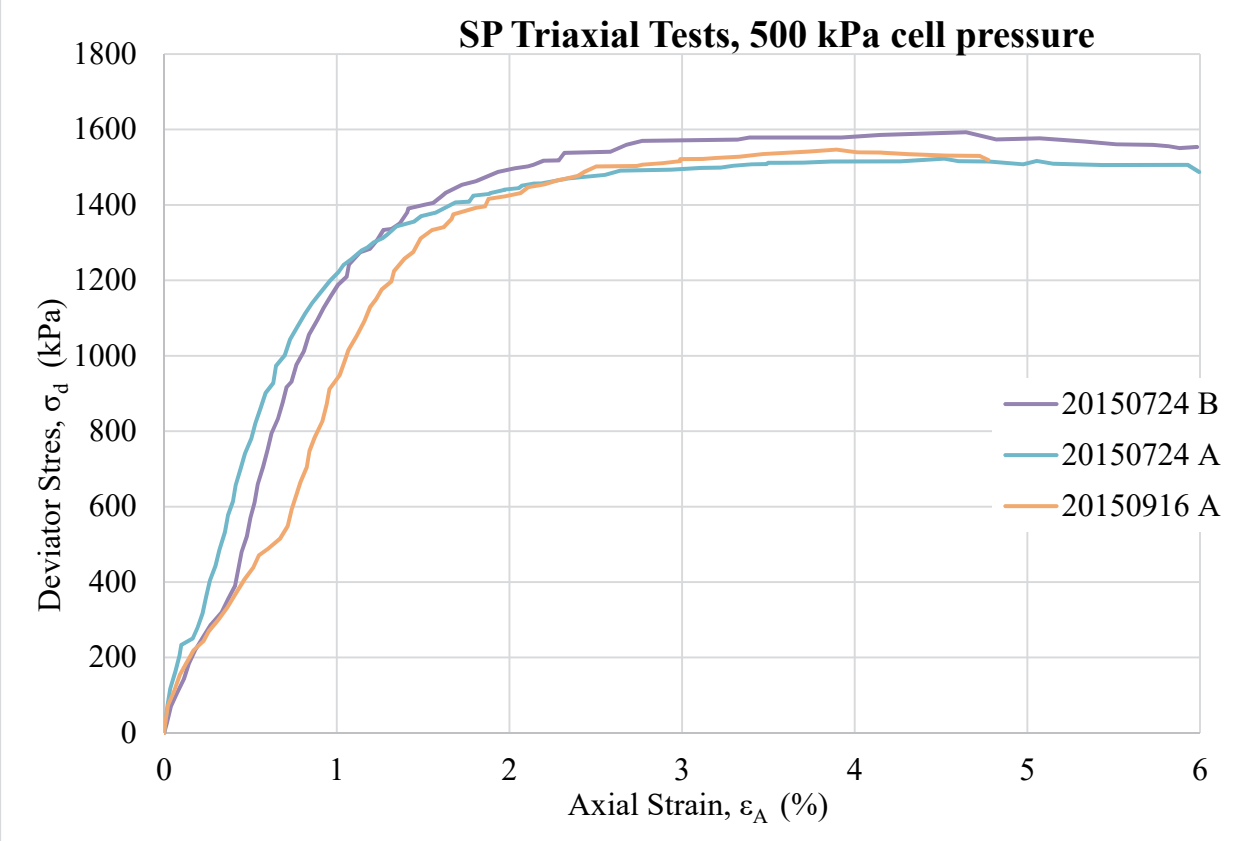
SP Triaxial Tests, 500 kPa cell pressure
Deviator Stres, σd (kPa)
1800
1600
1400
1200
1000
800
600
400
200
0
0
1
2
3
4
5
6
Axial Strain, εA (%)
20150724 B
20150724 A
20150916 A

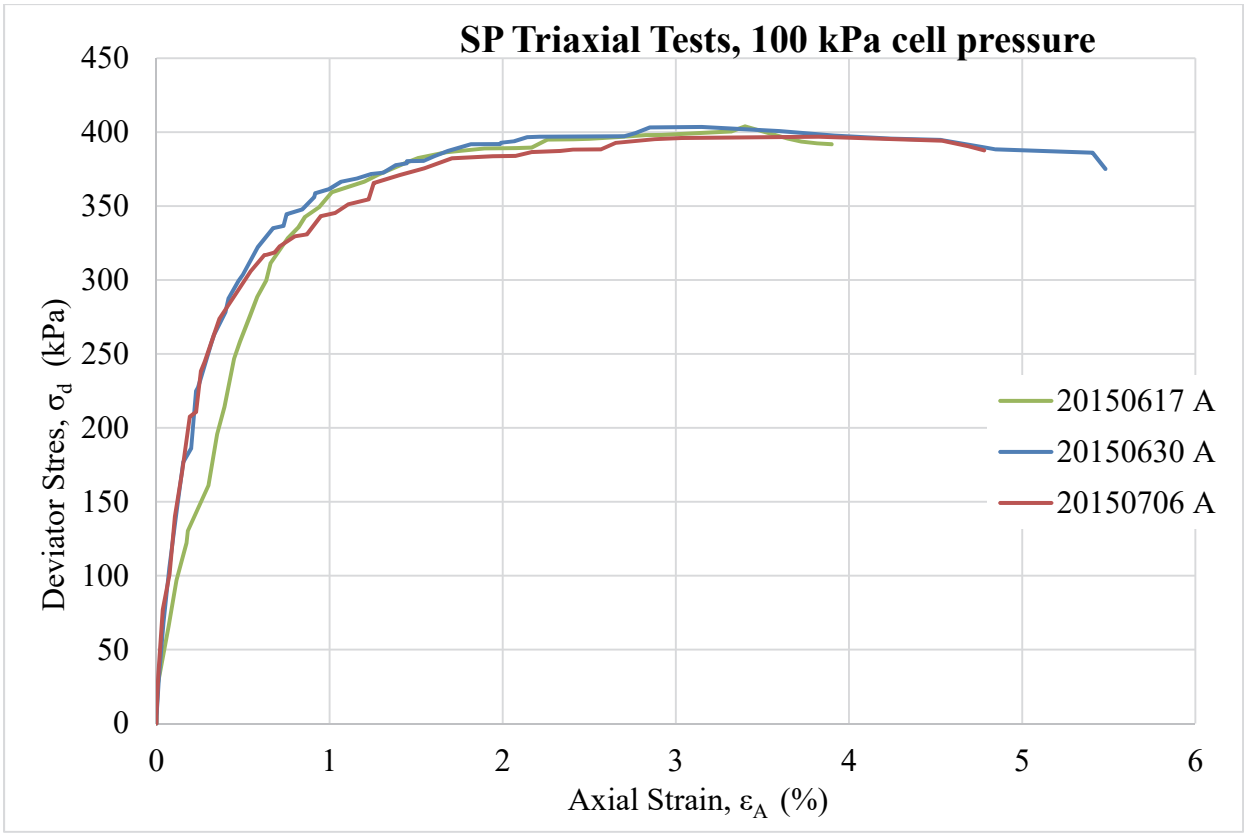
SP Triaxial Tests, 100 kPa cell pressure
Deviator Stres, σd (kPa)
Axial Strain, εA (%)
0
50
100
150
200
250
300
350
400
450
0
1
2
3
4
5
6
20150617 A
20150630 A
20150706 A

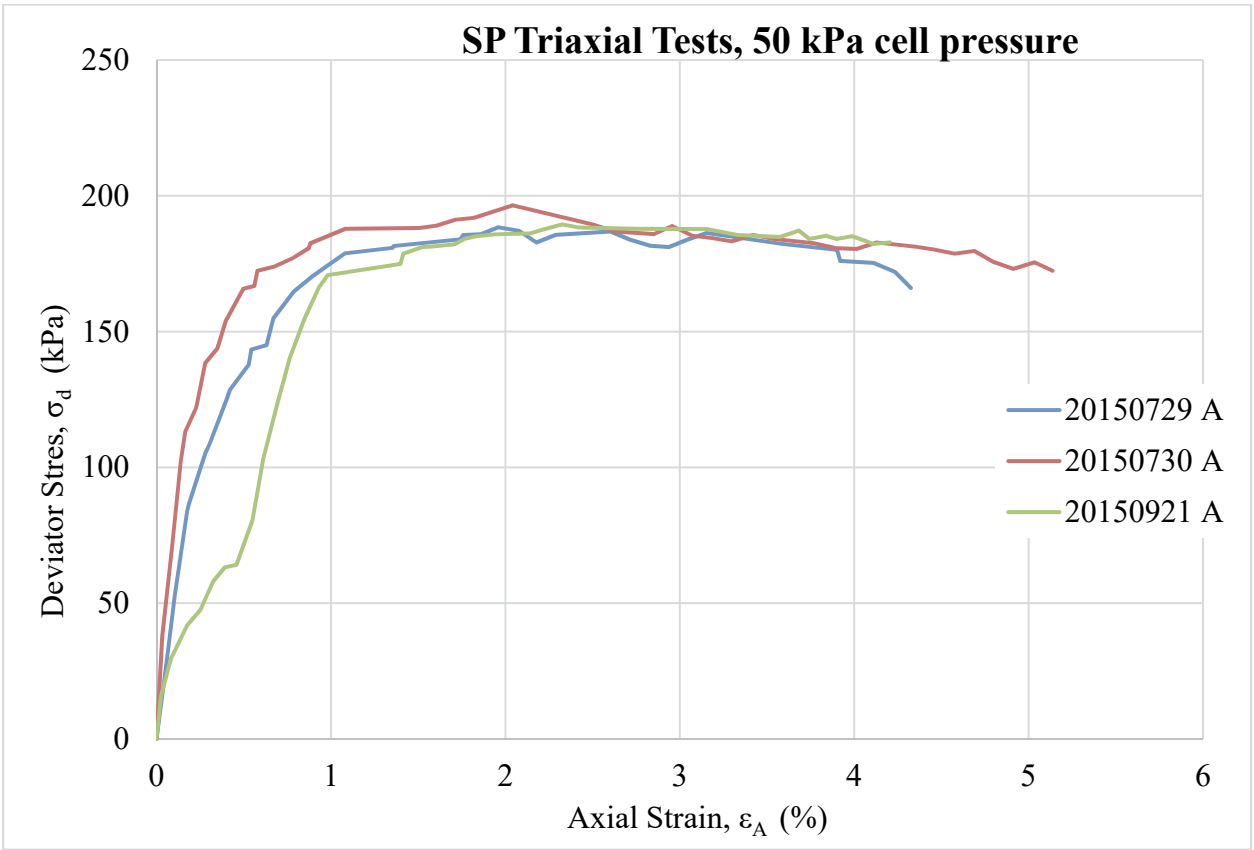
SP Triaxial Tests, 50 kPa cell pressure
Deviator Stres, σd (kPa)
Axial Strain, εA (%)
0
50
100
150
200
250
0
1
2
3
4
5
6
20150729 A
20150730 A
20150921 A

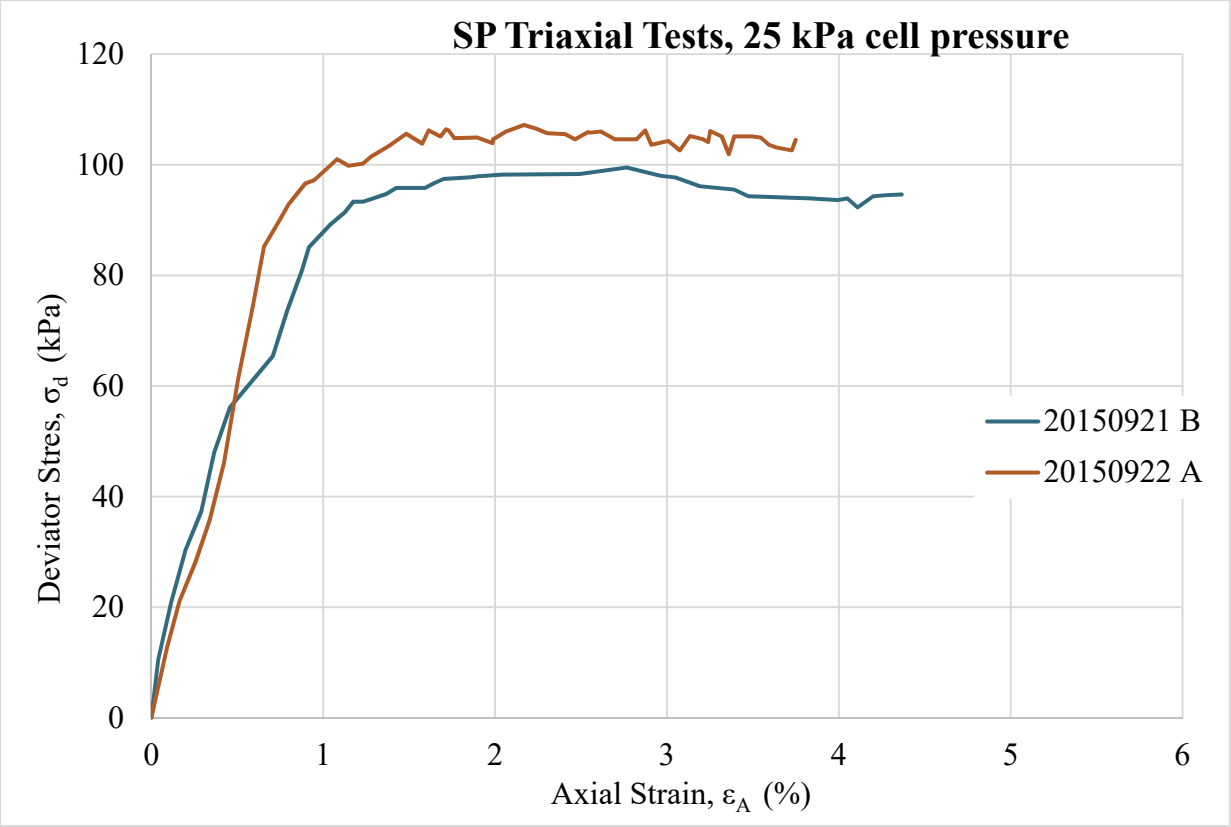
SP Triaxial Tests, 25 kPa cell pressure
Deviator Stres, σd (kPa)
Axial Strain, εA (%)
0
20
40
60
80
100
120
0
1
2
3
4
5
6
20150921 B
20150922 A

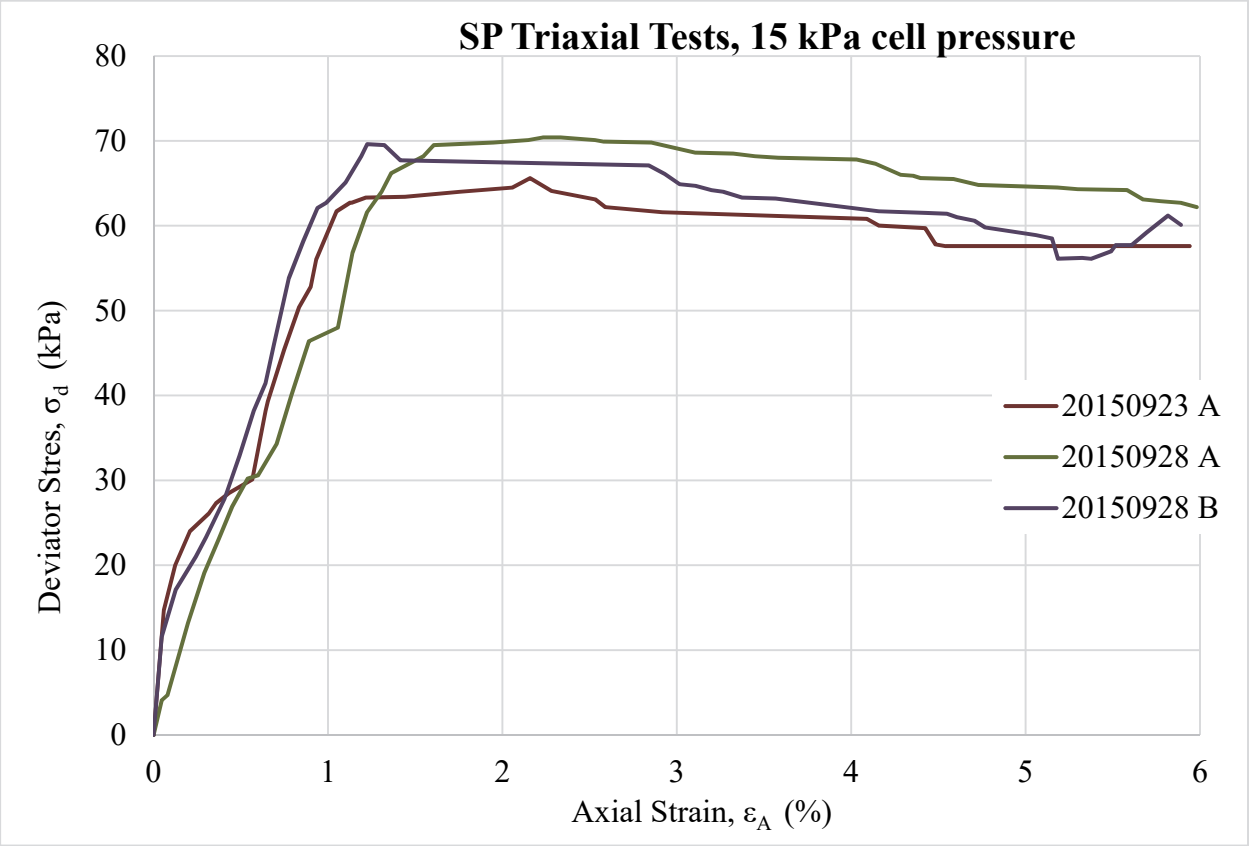
SP Triaxial Tests, 15 kPa cell pressure
Deviator Stres, σd (kPa)
Axial Strain, εA (%)
0
10
20
30
40
50
60
70
80
0
1
2
3
4
5
6
20150923 A
20150928 A
20150928 B

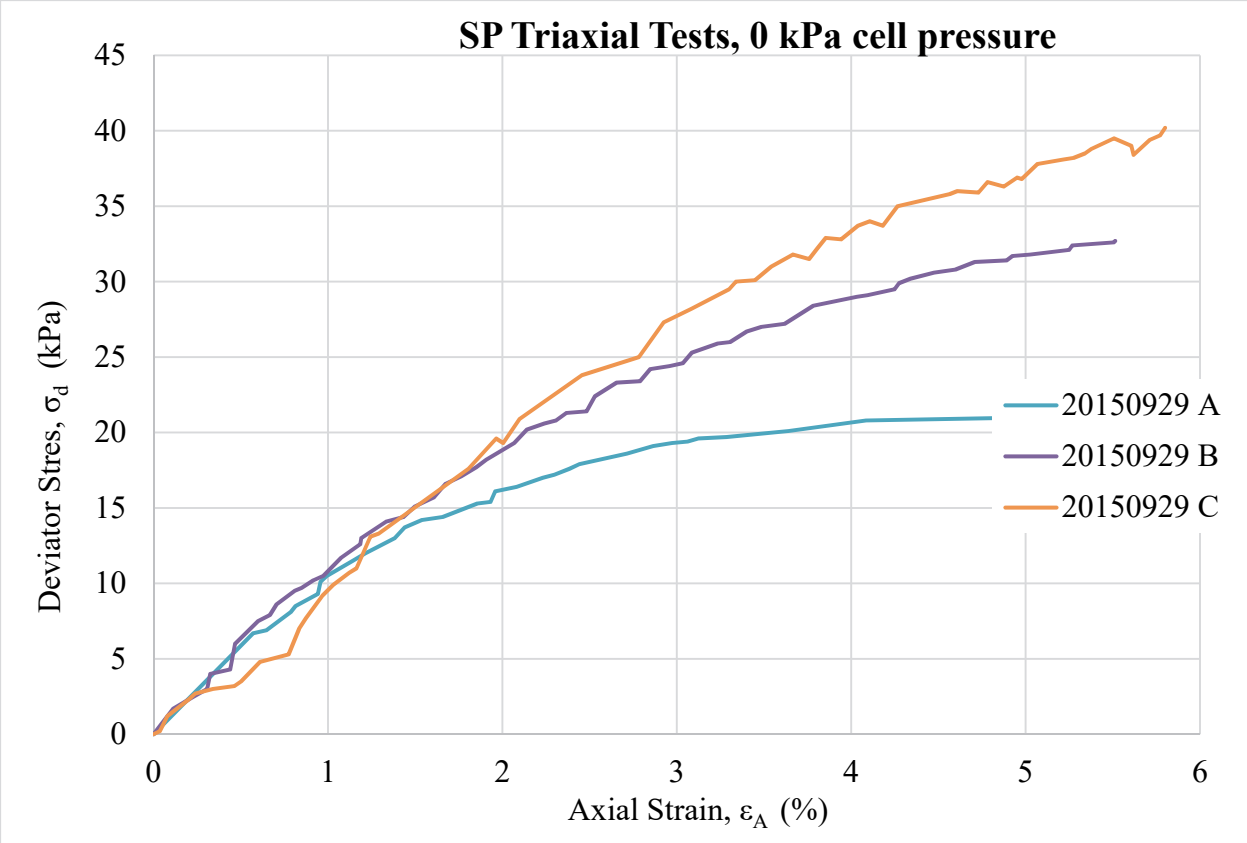
SP Triaxial Tests, 0 kPa cell pressure
Deviator Stres, σd (kPa)
Axial Strain, εA (%)
0
5
10
15
20
25
30
35
40
45
0
1
2
3
4
5
6
20150929 A
20150929 B
20150929 C

SM triaxial test data

Target Cell Pressure (kPa)	Cell Pressure at σ_d Max (kPa)	Maximum Deviator Stress (σ_d, kPa)	Test Name	Membrane
1000	999	2167	20160728 A	Yes
1000	999	2172	20160729 A	Yes
1000	999	2172	20160802 A	Yes
500	500	1381	20160229 A	Yes
500	500	1350	20160229 B	Yes
500	500	1381	20160302 A	Yes
100	106	328	20150501 A	Yes
100	107	330	20150504 A	Yes
100	107	324	20150511 A	Yes
50	55	159	20150505 A	Yes
50	55	182	20150505 B	Yes
50	57	189	20150506 A	Yes
25	32	119	20150507 A	Yes
25	31	112	20150508 A	Yes
25	30	131	20150513 A	Yes
15	15	77	20150625 B	Yes
15	20	94	20150626 A	Yes
15	20	90	20150629 B	Yes
0	0	27	20150507 B	Yes
0	0	27	20150507 C	Yes
0	0	29	20150507 D	Yes
0	0	24	20150508 B	No
0	0	30	20150514 A	No
0	0	26	20150514 B	No

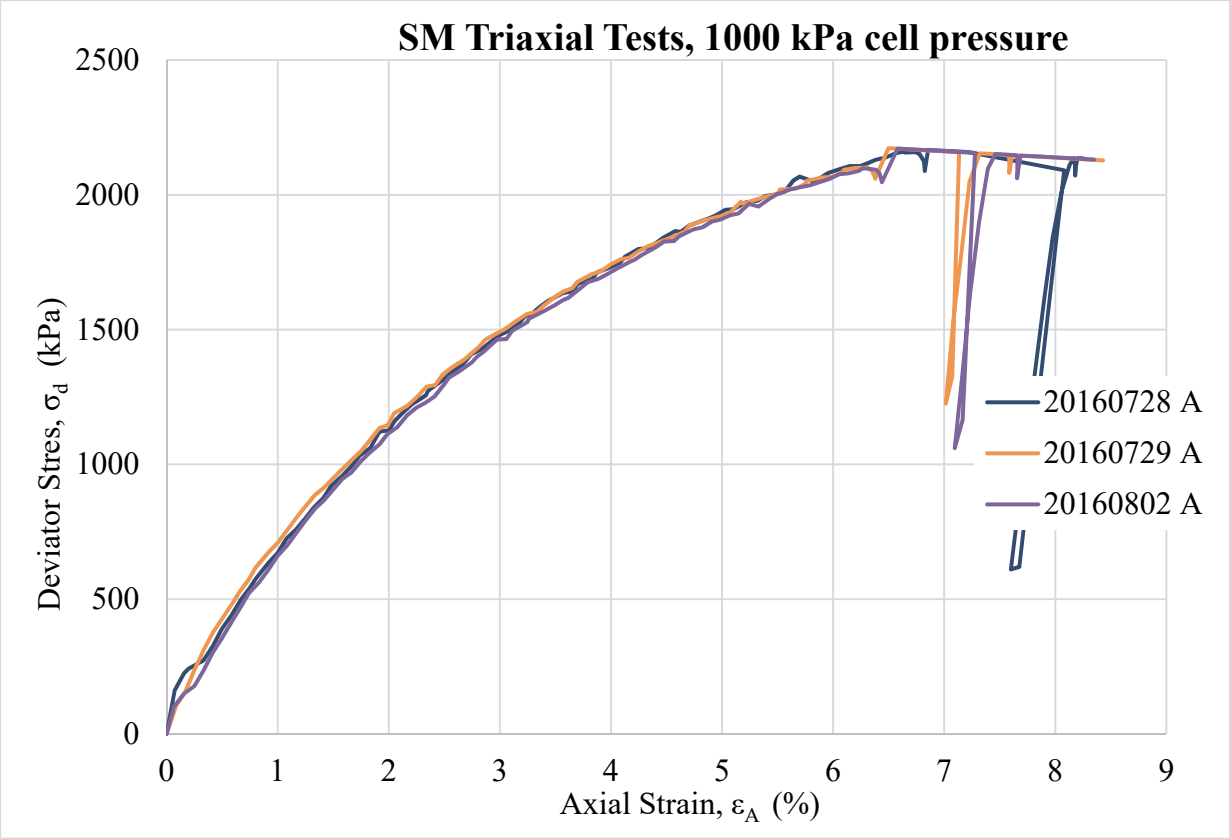
SM Triaxial Tests, 1000 kPa cell pressure
Deviator Stres, σd (kPa)
Axial Strain, εA (%)
20160728 A
20160729 A
20160802 A

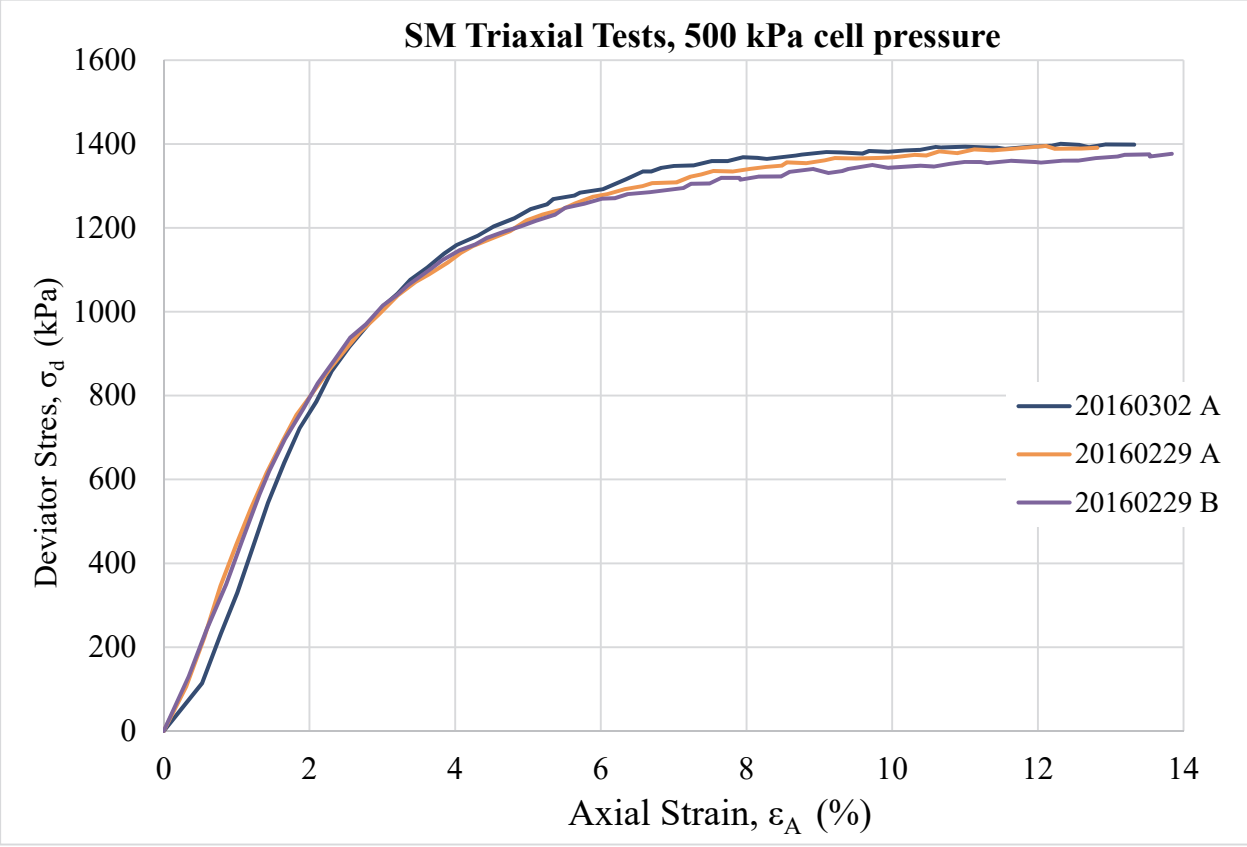
SM Triaxial Tests, 500 kPa cell pressure
Deviator Stres, σd (kPa)
Axial Strain, εA (%)
20160302 A
20160229 A
20160229 B

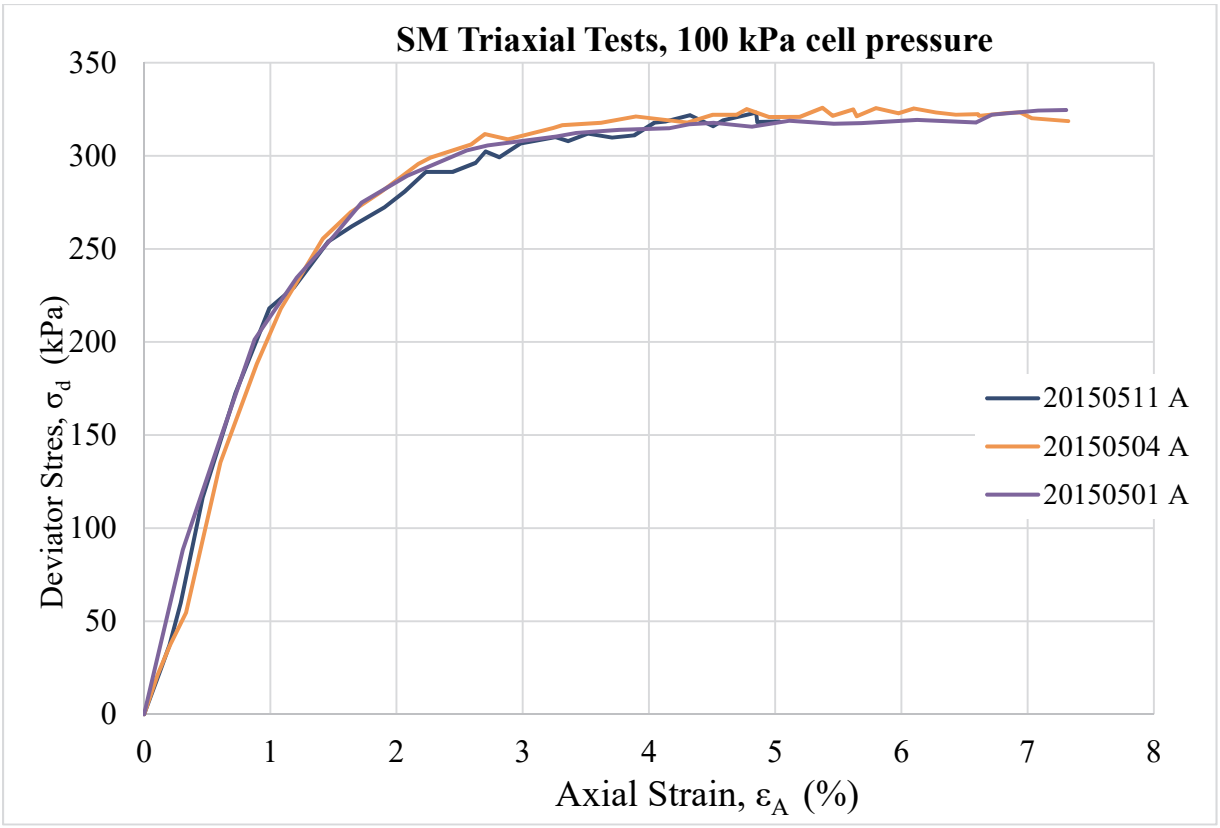
SM Triaxial Tests, 100 kPa cell pressure
Deviator Stres, σd (kPa)
Axial Strain, εA (%)
0
50
100
150
200
250
300
350
0
1
2
3
4
5
6
7
8
20150511 A
20150504 A
20150501 A

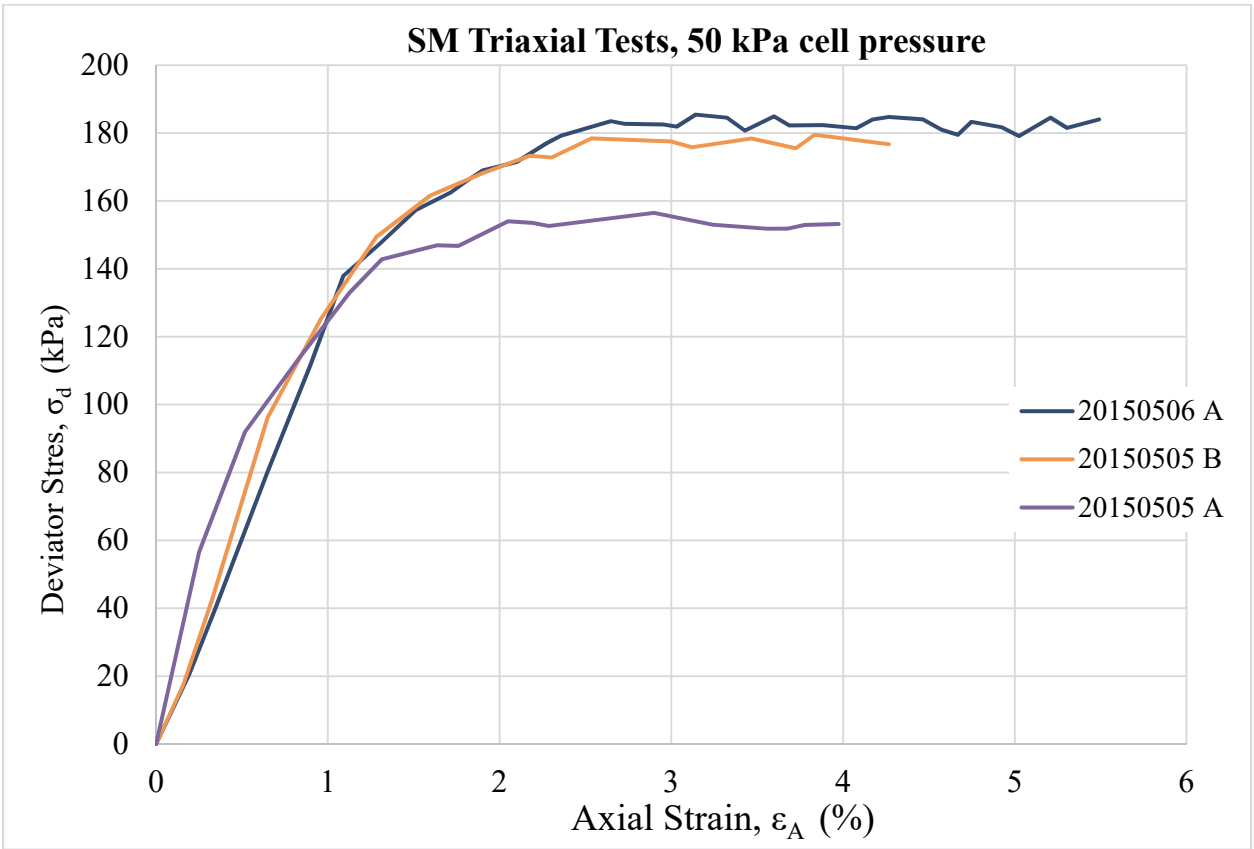
SM Triaxial Tests, 50 kPa cell pressure
Deviator Stres, σd (kPa)
Axial Strain, εA (%)
0
20
40
60
80
100
120
140
160
180
200
0
1
2
3
4
5
6
20150506 A
20150505 B
20150505 A

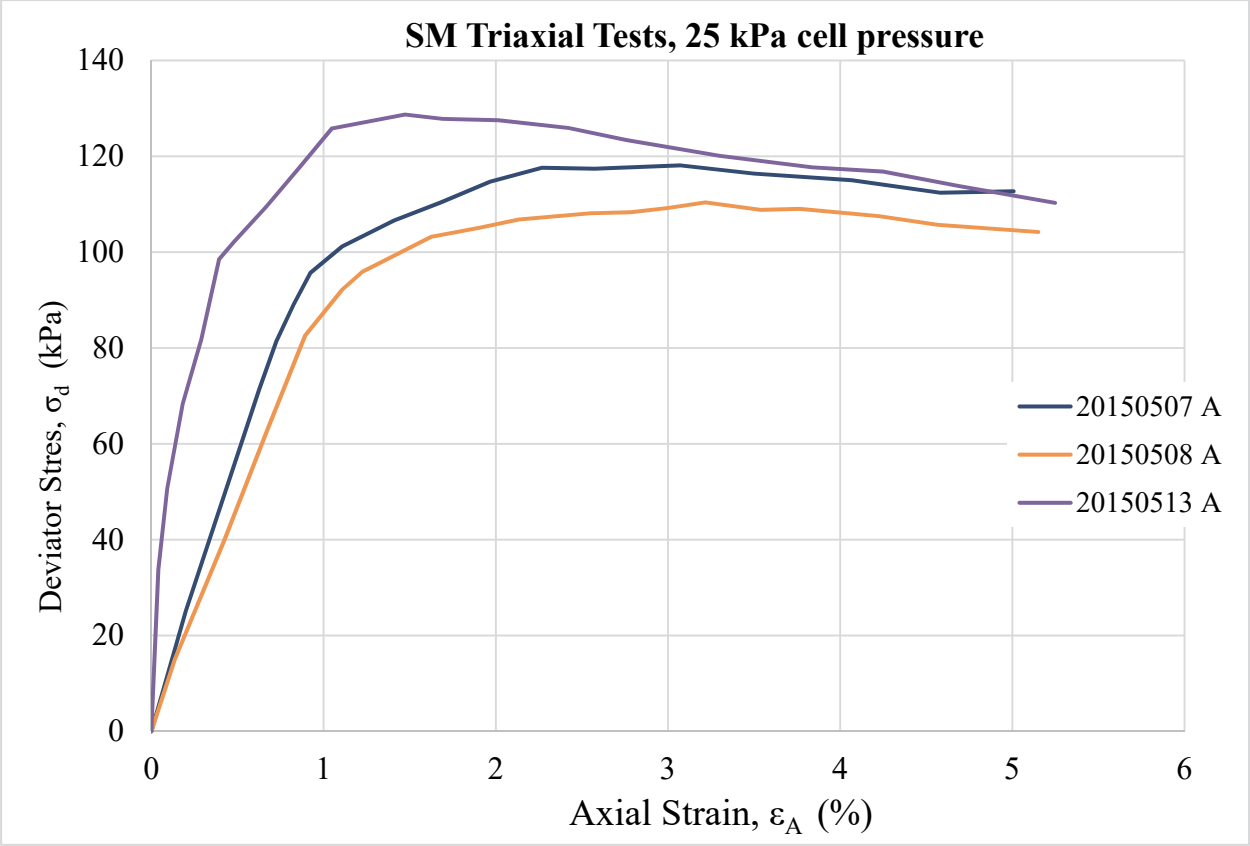
SM Triaxial Tests, 25 kPa cell pressure
Deviator Stres, σd (kPa)
Axial Strain, εA (%)
0
20
40
60
80
100
120
140
0
1
2
3
4
5
6
20150507 A
20150508 A
20150513 A

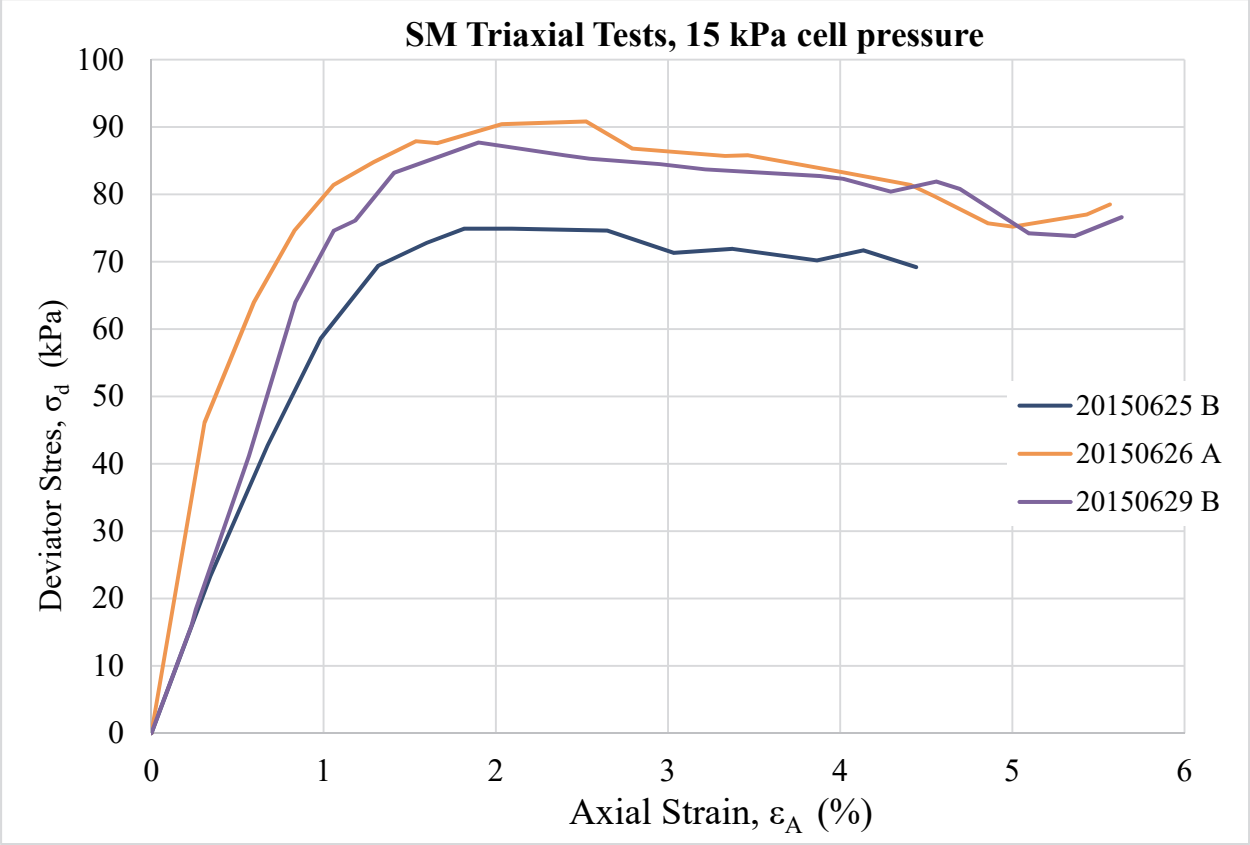
SM Triaxial Tests, 15 kPa cell pressure
Deviator Stres, σd (kPa)
Axial Strain, εA (%)
0
10
20
30
40
50
60
70
80
90
100
0
1
2
3
4
5
6
20150625 B
20150626 A
20150629 B

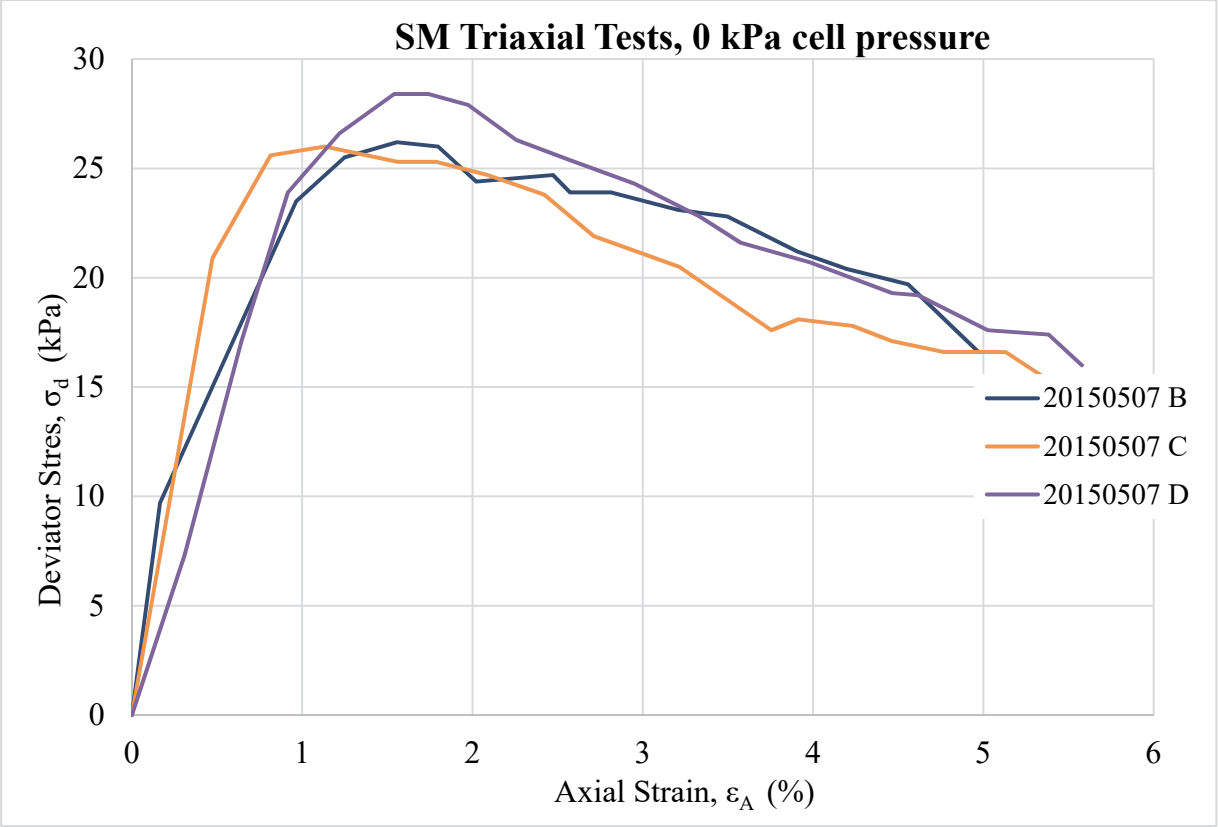
SM Triaxial Tests, 0 kPa cell pressure
Deviator Stres, σd (kPa)
Axial Strain, εA (%)
0
5
10
15
20
25
30
0
1
2
3
4
5
6
20150507 B
20150507 C
20150507 D

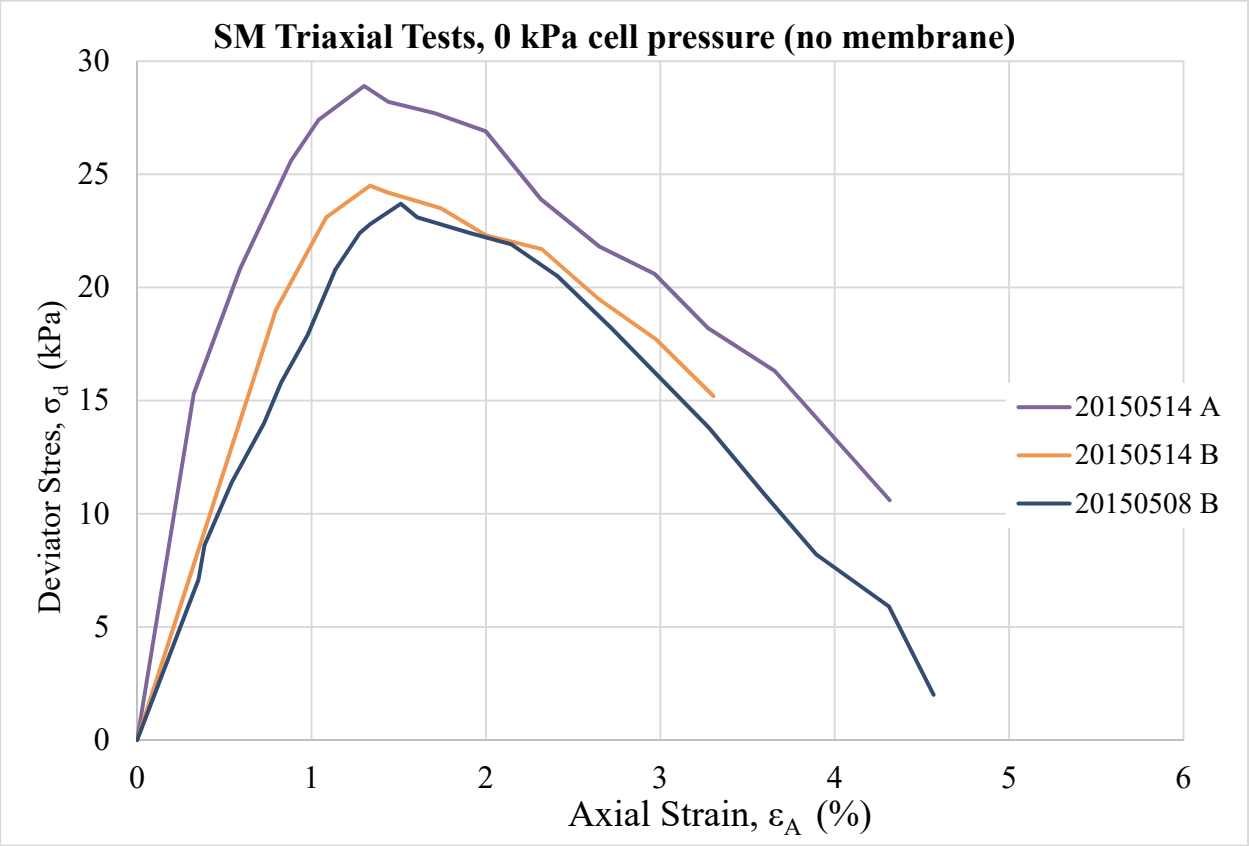
SM Triaxial Tests, 0 kPa cell pressure (no membrane)
Deviator Stres, σd (kPa)
Axial Strain, εA (%)
0
5
10
15
20
25
30
0
1
2
3
4
5
6
20150514 A
20150514 B
20150508 B

ML triaxial test data

Target Cell Pressure (kPa)	Cell Pressure at σ_d Max (kPa)	Maximum Deviator Stress (σ_d, kPa)	Test Name
1000	1000	2032	20151116 A
1000	1000	2056	20151117 A
1000	1000	1966	20151117 B
500	500	1249	20151109 A
500	500	1182	20151109 B
500	500	1244	20151113 A
100	100	393	20151103 A
100	100	368	20151104 A
100	100	370	20151104 B
50	50	237	20151105 A
50	52	264	20151105 B
50	51	240	20151106 A
25	27	211	20151110 A
25	26	205	20151110 B
25	27	187	20151112 B
15	15	157	20151123 A
15	16	162	20151124 A
15	17	156	20151124 B
0	0	106	20151028 A
0	0	89	20151130 B
0	0	112	20151201 A

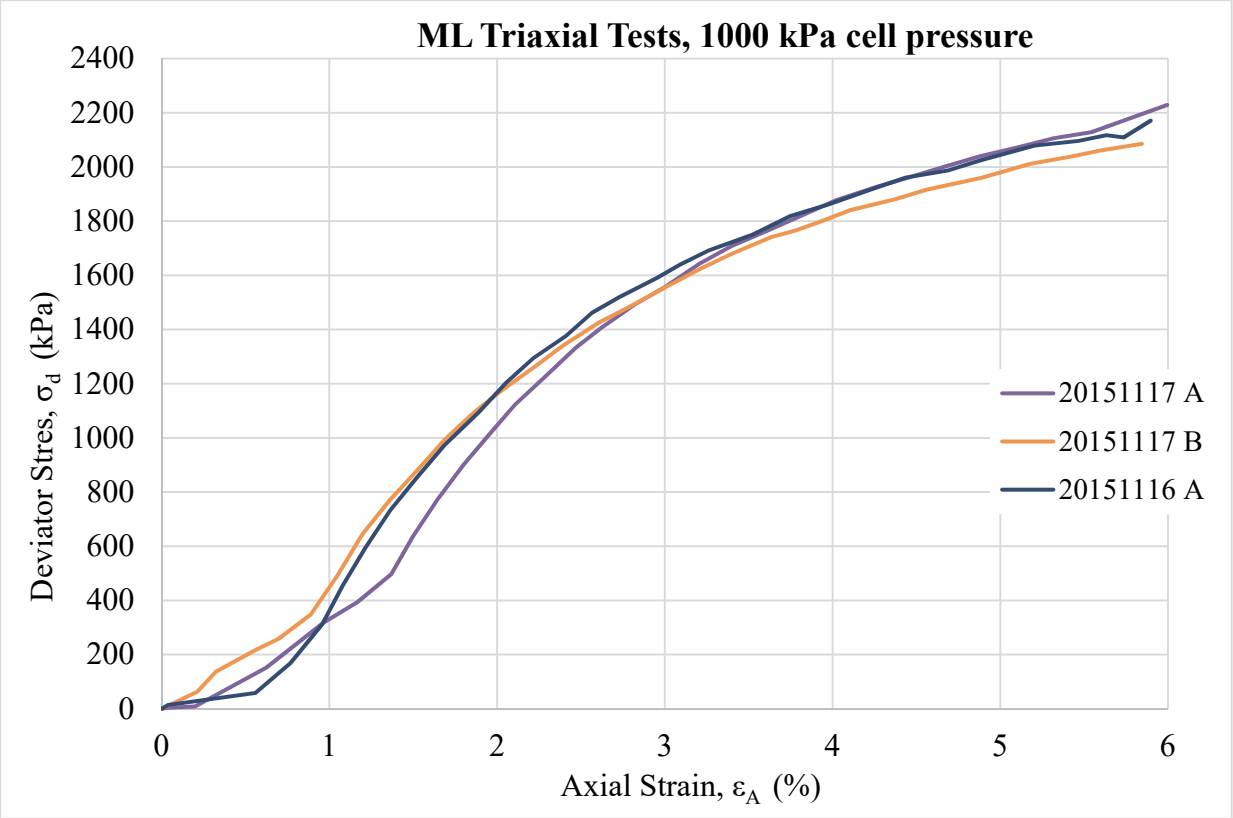
ML Triaxial Tests, 1000 kPa cell pressure
Deviator Stres, σd (kPa)
Axial Strain, εA (%)
20151117 A
20151117 B
20151116 A

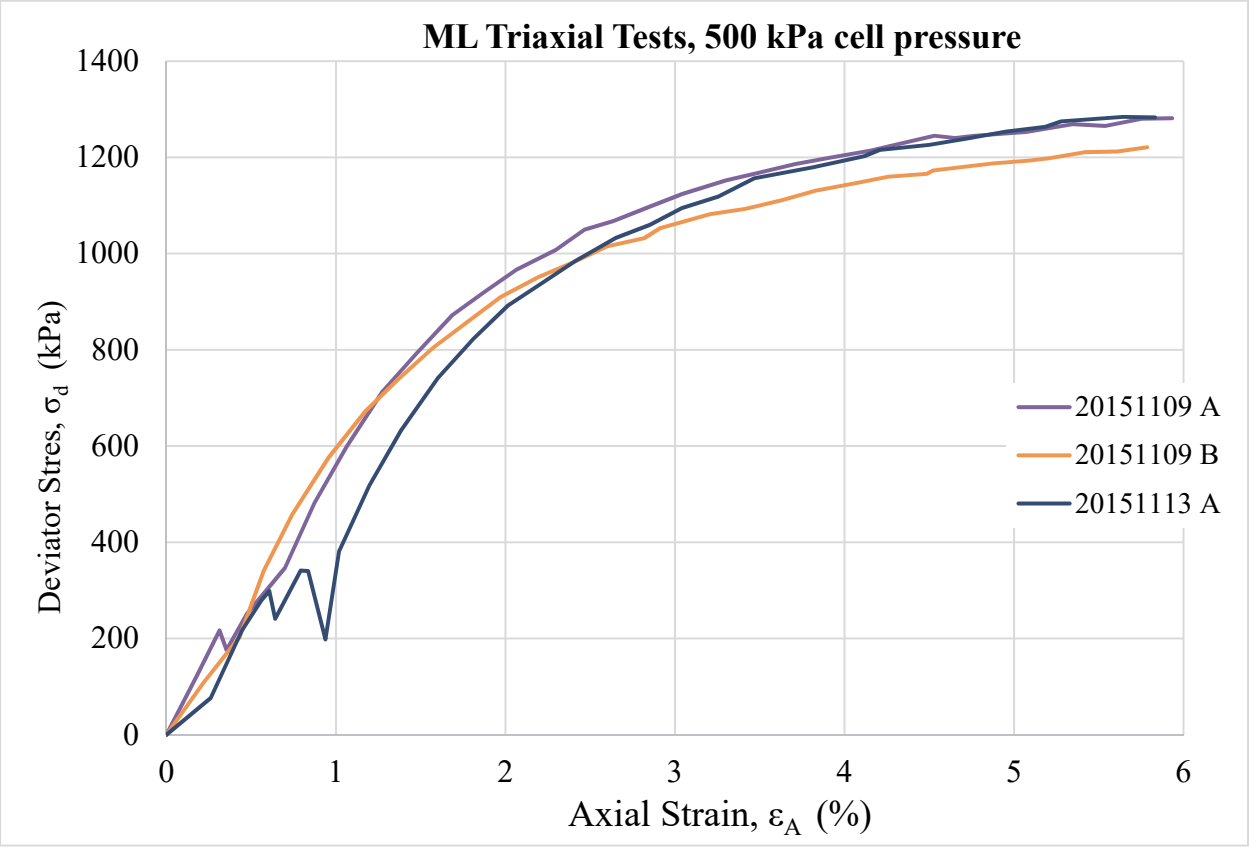
ML Triaxial Tests, 500 kPa cell pressure
Deviator Stres, σd (kPa)
Axial Strain, εA (%)
20151109 A
20151109 B
20151113 A

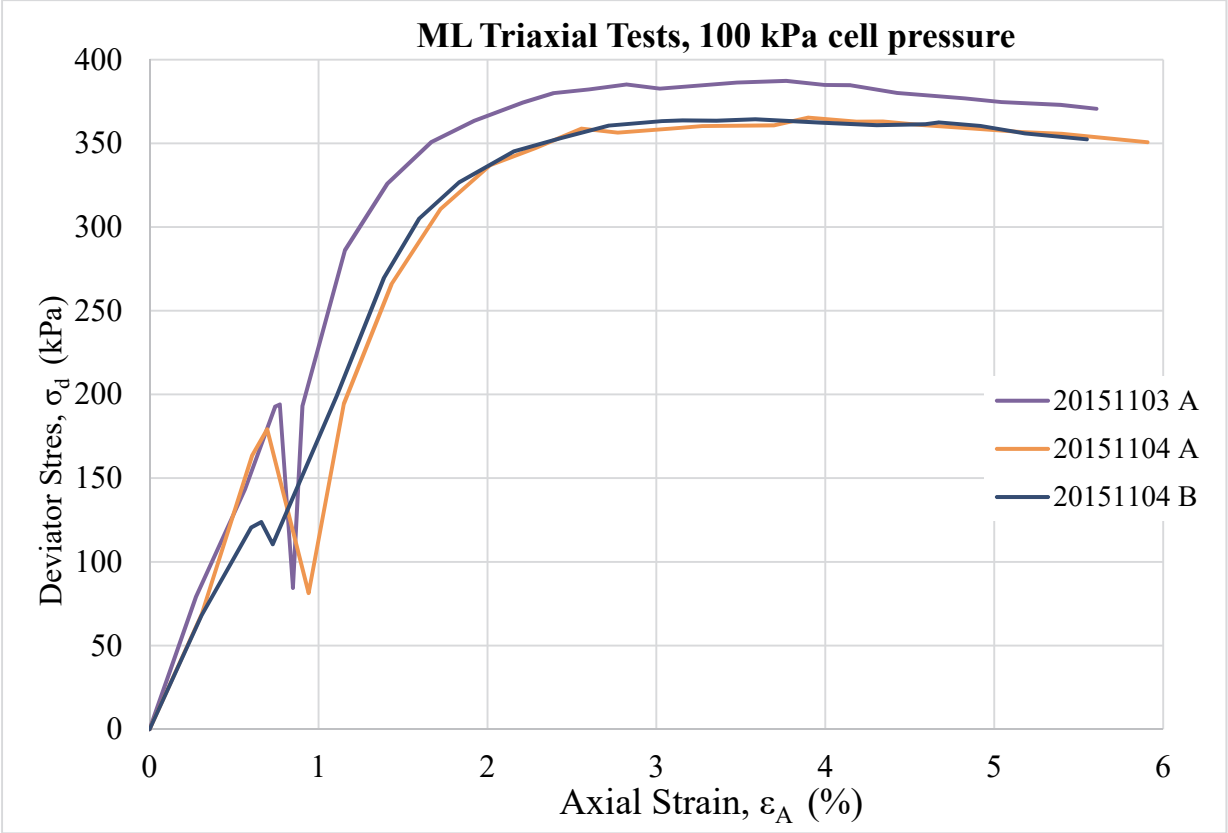
ML Triaxial Tests, 100 kPa cell pressure
Deviator Stres, σd (kPa)
Axial Strain, εA (%)
0
50
100
150
200
250
300
350
400
0
1
2
3
4
5
6
20151103 A
20151104 A
20151104 B

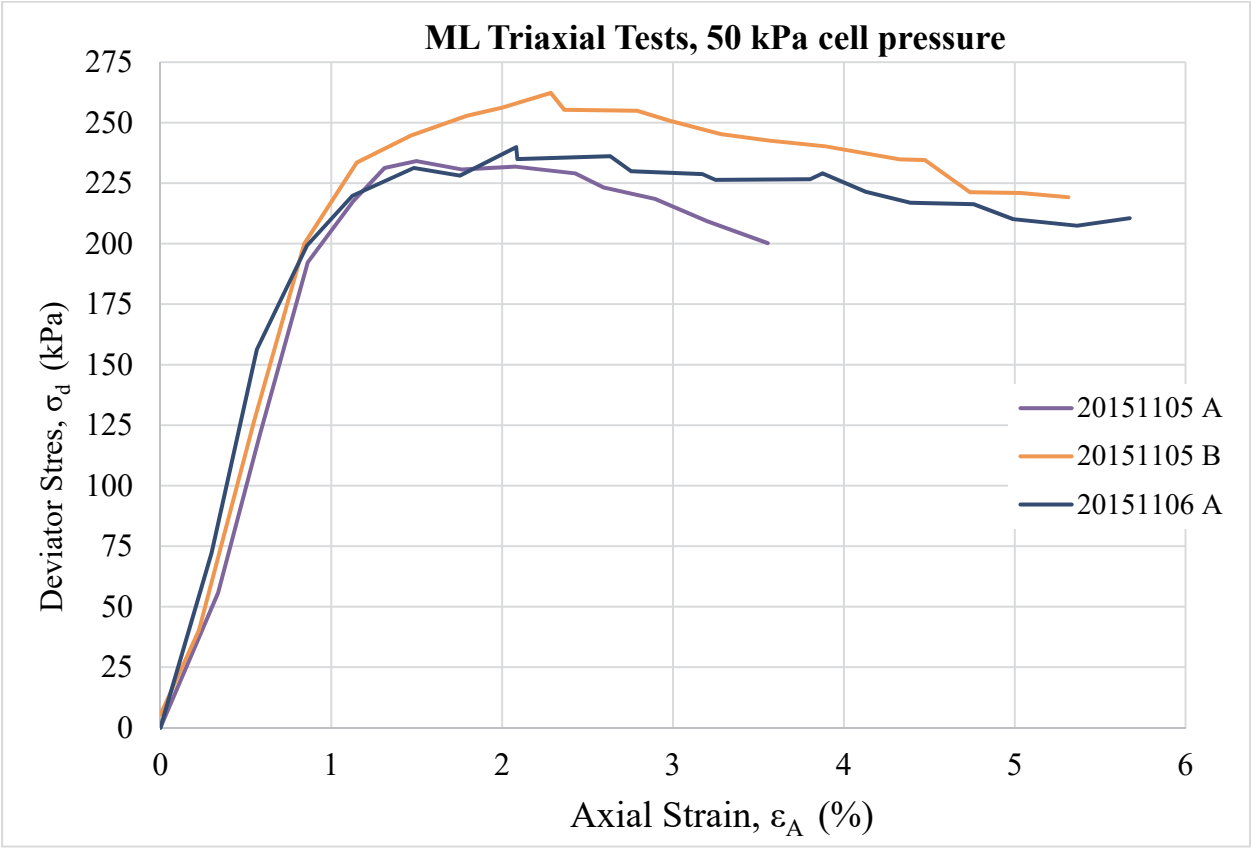
ML Triaxial Tests, 50 kPa cell pressure
Deviator Stres, σd (kPa)
Axial Strain, εA (%)
0
25
50
75
100
125
150
175
200
225
250
275
0
1
2
3
4
5
6
20151105 A
20151105 B
20151106 A

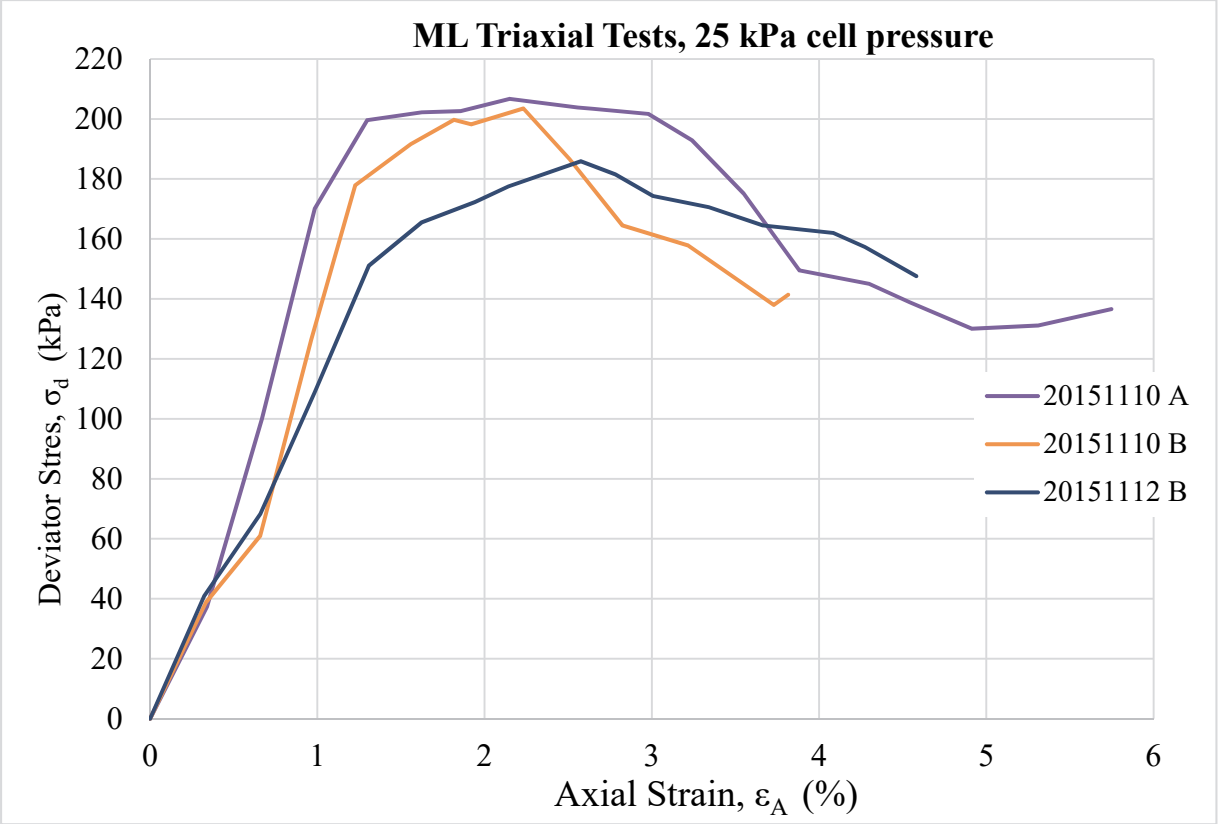
ML Triaxial Tests, 25 kPa cell pressure
Deviator Stres, σd (kPa)
Axial Strain, εA (%)
0
20
40
60
80
100
120
140
160
180
200
220
0
1
2
3
4
5
6
20151110 A
20151110 B
20151112 B

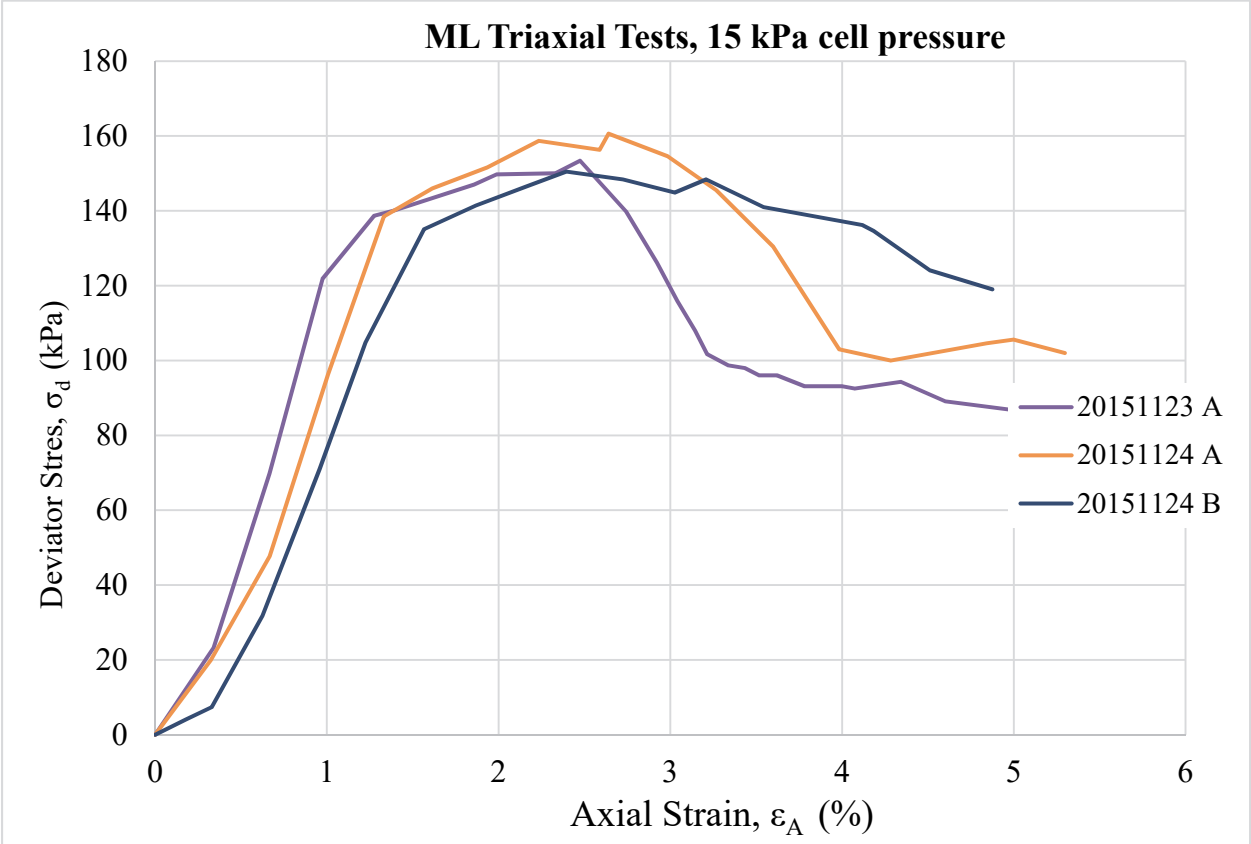
ML Triaxial Tests, 15 kPa cell pressure
Deviator Stres, σd (kPa)
Axial Strain, εA (%)
0
20
40
60
80
100
120
140
160
180
0
1
2
3
4
5
6
20151123 A
20151124 A
20151124 B

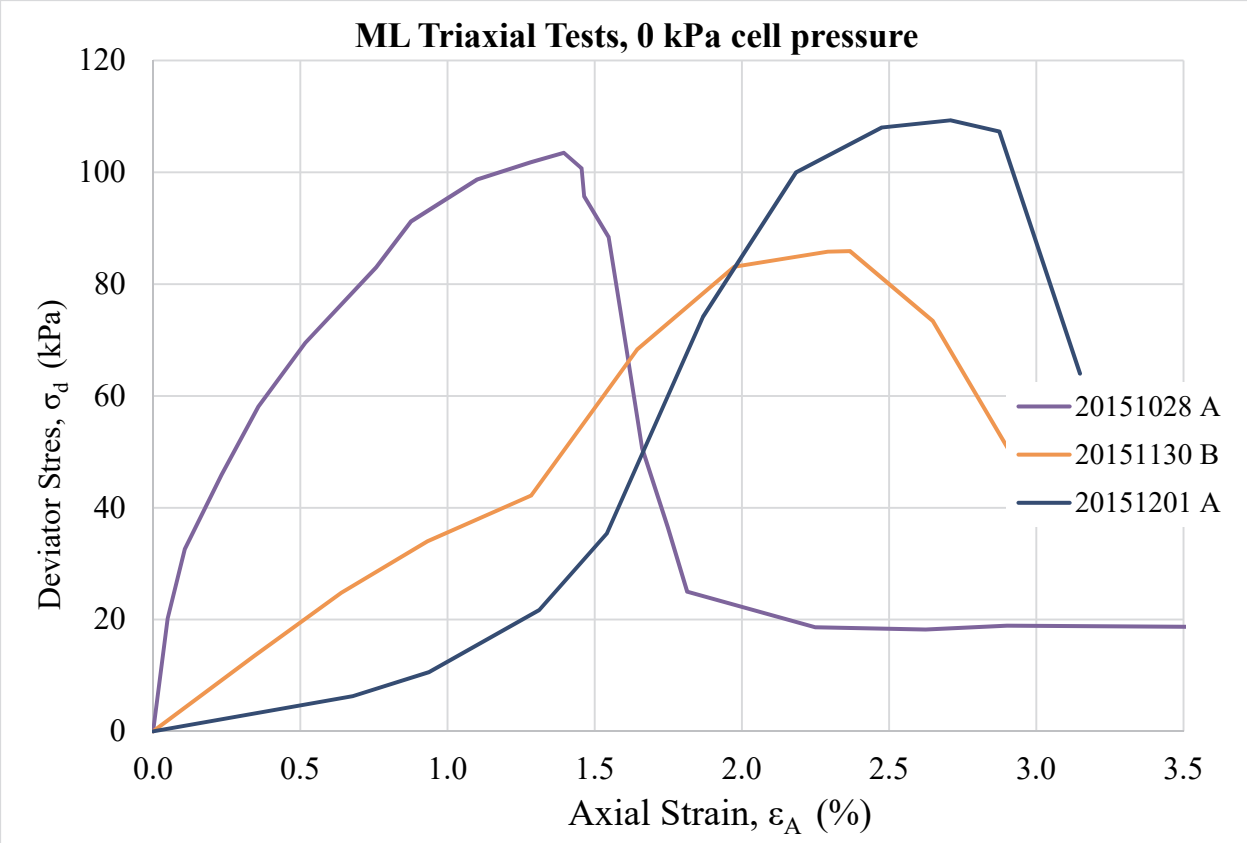
ML Triaxial Tests, 0 kPa cell pressure
120
100
80
60
40
20
0
Deviator Stres, σd (kPa)
0.0
0.5
1.0
1.5
2.0
2.5
3.0
3.5
Axial Strain, εA (%)
20151028 A
20151130 B
20151201 A

Simple shear test data

SP simple shear test data

Cell Pressure (kPa)	Shear Stress at Failure τ (kPa)	Test Name
500	307.9	20160427aCP500
500	300.9	20160428aCP500
500	307.0	20160519aCP500
250	174.1	20160127aCP250
250	173.8	20160128aCP250
250	180.0	20160201aCP250
100	62.6	Jan27B
100	66.6	Jan28A
100	64.9	Jan30A
75	57.0	20150721CP75
75	59.5	20150819aCP75
75	55.3	20150724CP75
50	48.0	20150722aCP50
50	42.3	20150819bCP50
50	45.9	20150924bCP50
25	21.0	20150722bCP25
25	25.6	20150914aCP25
25	23.6	20150922aCP25
15	17.6	20160406CP15
15	13.8	20160407CP15
15	17.0	20160414CP15
0	6.2	20150924cD5
0	8.1	20150928aD5
0	8.0	20150928bD5
0	5.6	20150918aD2
0	6.9	20150918bD2
0	7.3	20150924aD2

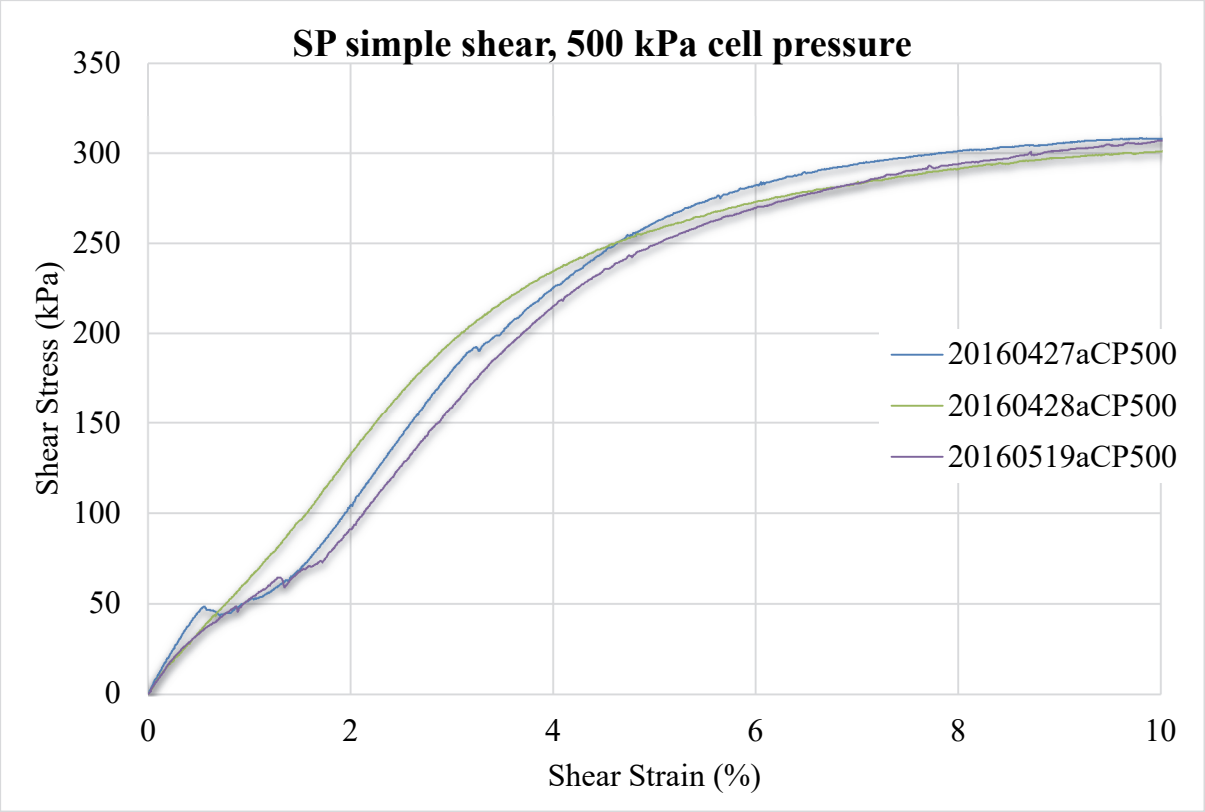
SP simple shear, 500 kPa cell pressure
Shear Stress (kPa)
Shear Strain (%)
0
50
100
150
200
250
300
350
0
2
4
6
8
10
20160427aCP500
20160428aCP500
20160519aCP500

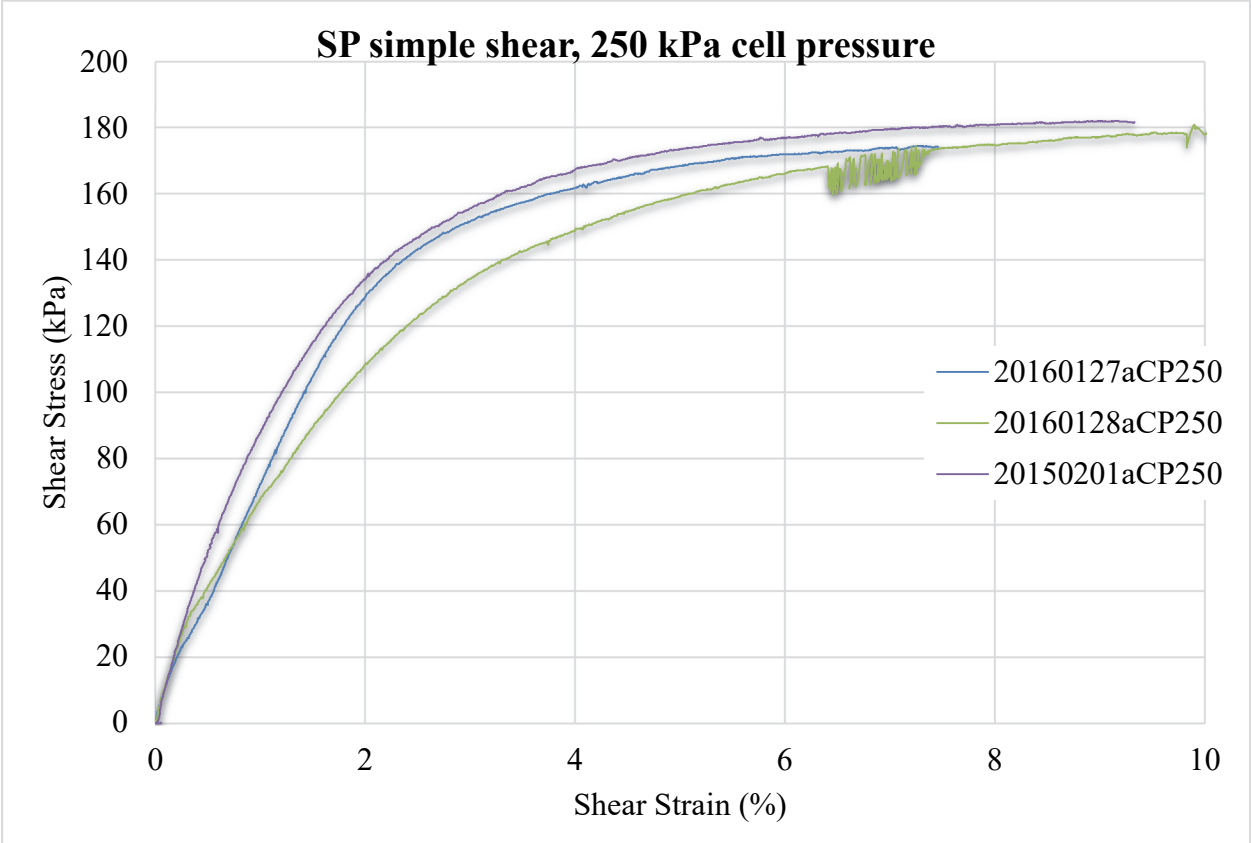
SP simple shear, 250 kPa cell pressure
Shear Stress (kPa)
Shear Strain (%)
0
20
40
60
80
100
120
140
160
180
200
0
2
4
6
8
10
20160127aCP250
20160128aCP250
20150201aCP250

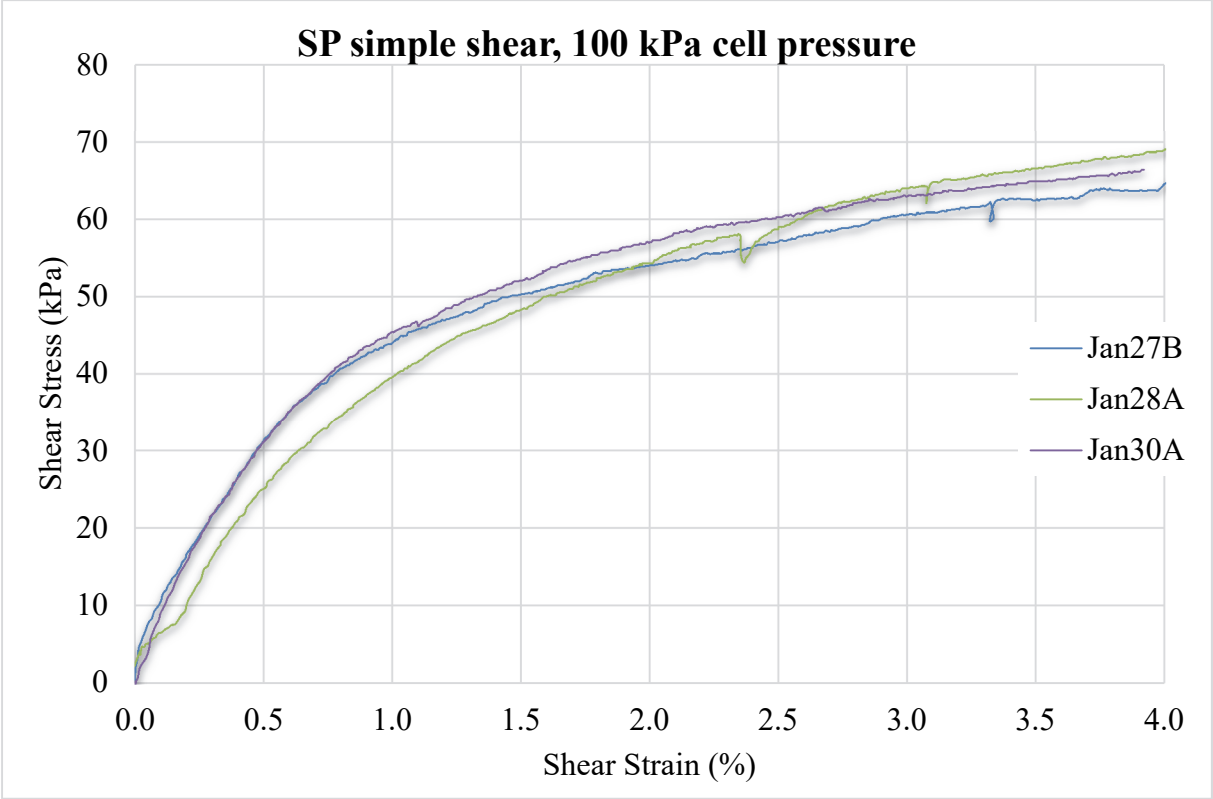
SP simple shear, 100 kPa cell pressure
Shear Stress (kPa)
Shear Strain (%)
0
10
20
30
40
50
60
70
80
0.0
0.5
1.0
1.5
2.0
2.5
3.0
3.5
4.0
Jan27B
Jan28A
Jan30A

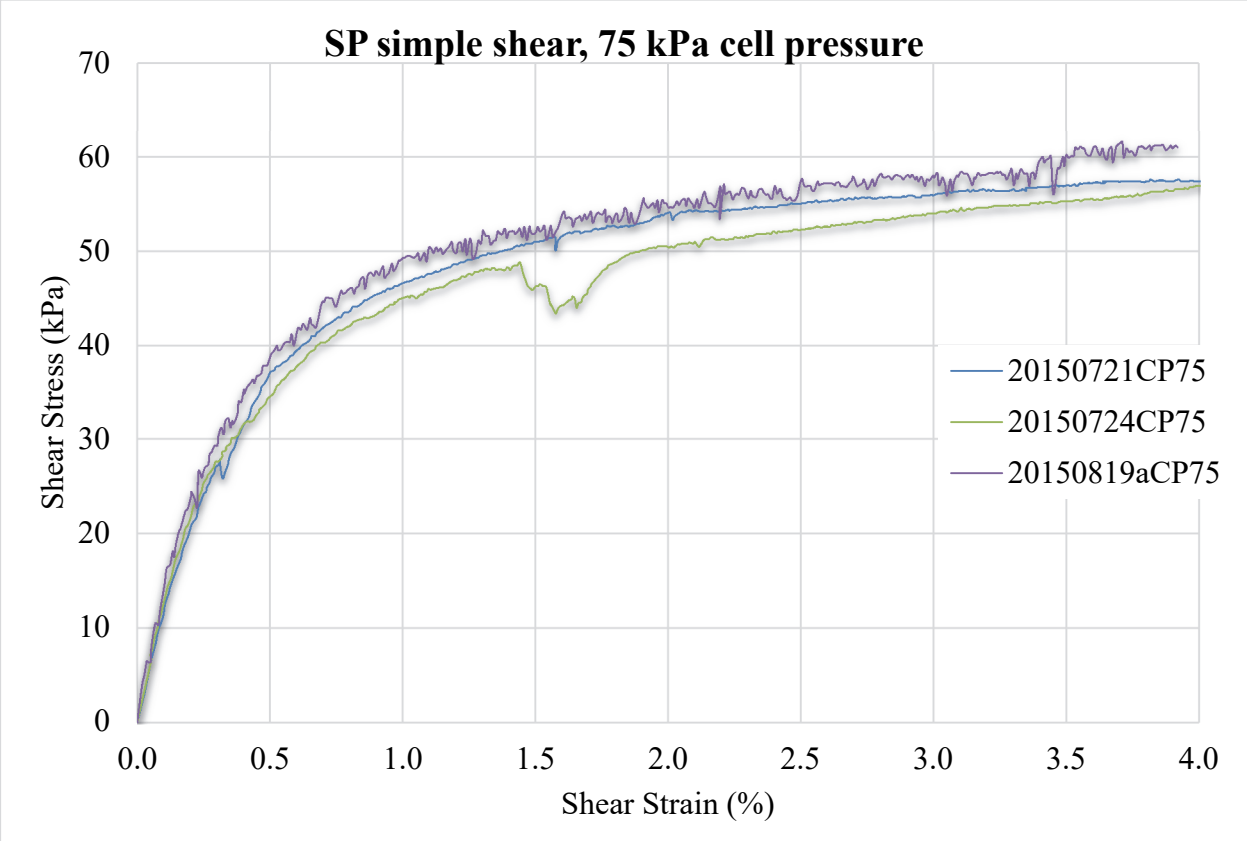
SP simple shear, 75 kPa cell pressure
Shear Stress (kPa)
Shear Strain (%)
0
10
20
30
40
50
60
70
0.0
0.5
1.0
1.5
2.0
2.5
3.0
3.5
4.0
20150721CP75
20150724CP75
20150819aCP75

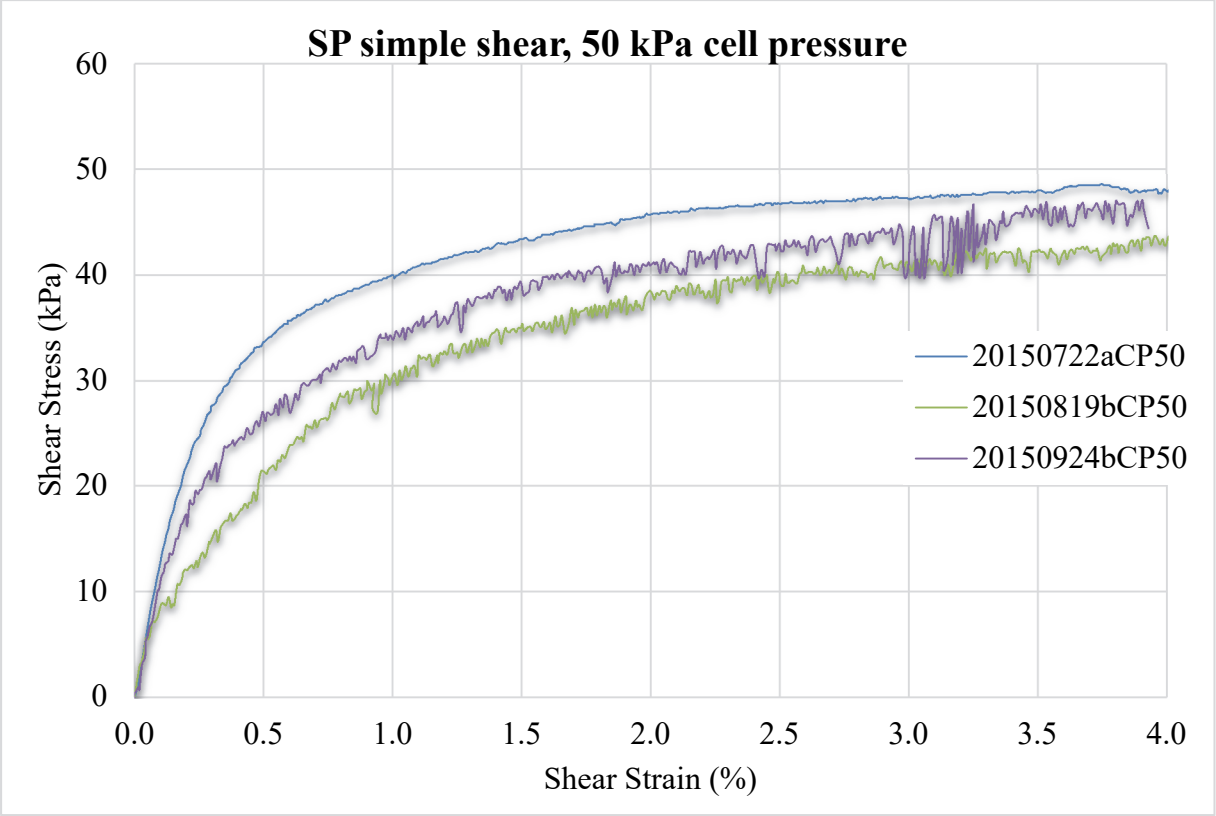
SP simple shear, 50 kPa cell pressure
Shear Stress (kPa)
Shear Strain (%)
0
10
20
30
40
50
60
0.0
0.5
1.0
1.5
2.0
2.5
3.0
3.5
4.0
20150722aCP50
20150819bCP50
20150924bCP50

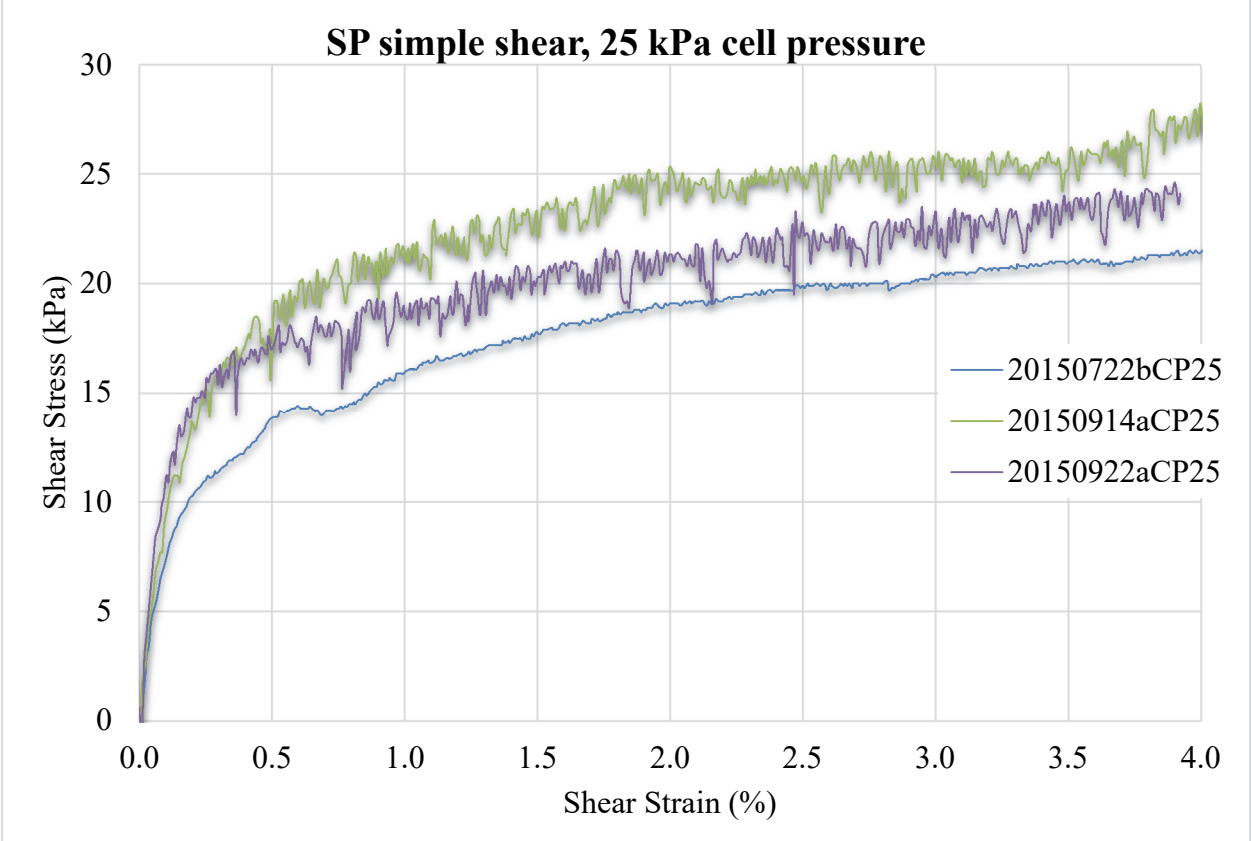
SP simple shear, 25 kPa cell pressure
Shear Stress (kPa)
Shear Strain (%)
0
5
10
15
20
25
30
0.0
0.5
1.0
1.5
2.0
2.5
3.0
3.5
4.0
20150722bCP25
20150914aCP25
20150922aCP25

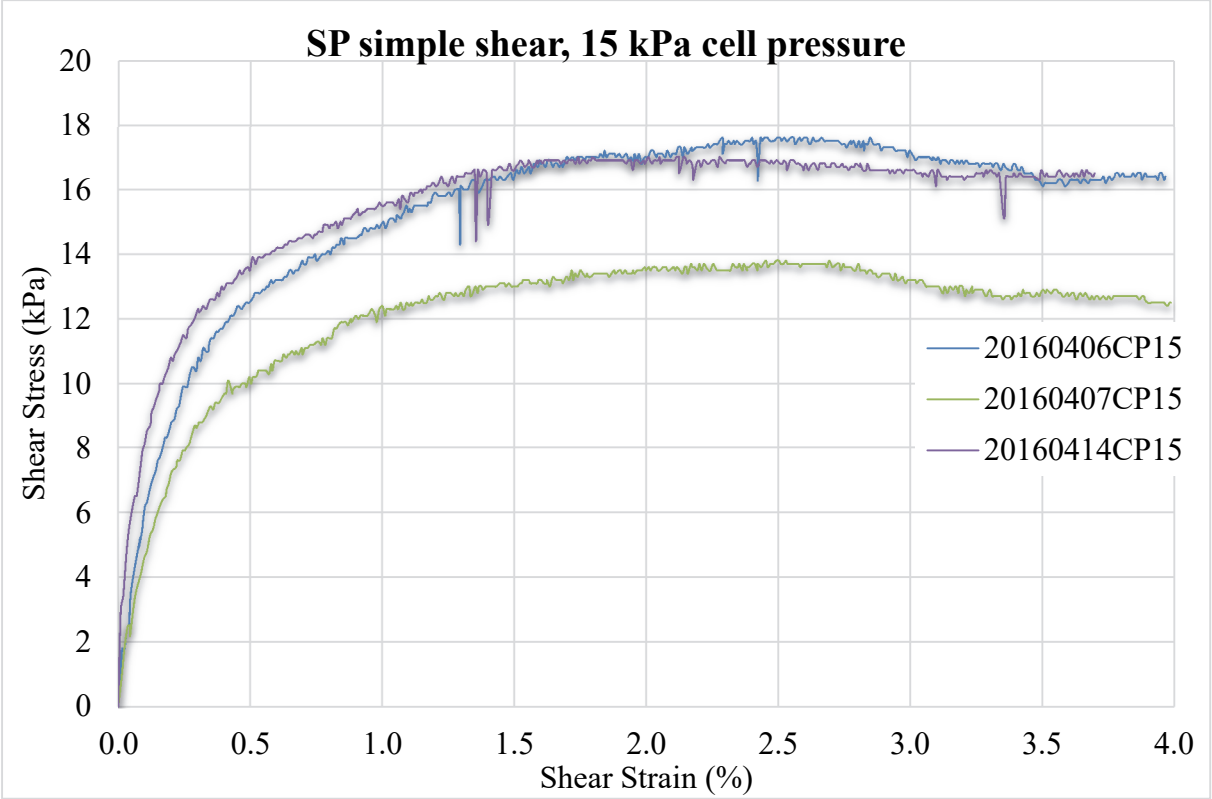
SP simple shear, 15 kPa cell pressure
Shear Stress (kPa)
Shear Strain (%)
20160406CP15
20160407CP15
20160414CP15

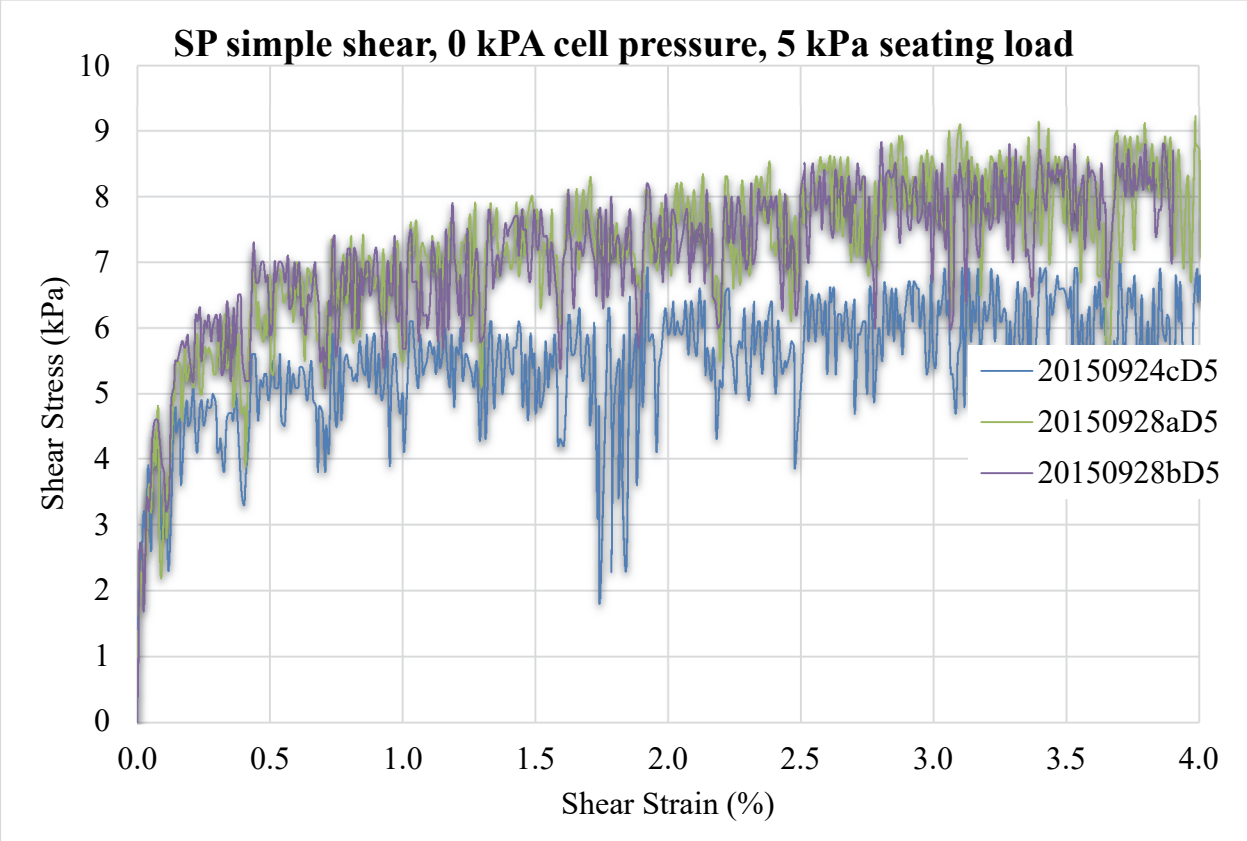
SP simple shear, 0 kPA cell pressure, 5 kPa seating load
Shear Stress (kPa)
Shear Strain (%)
20150924cD5
20150928aD5
20150928bD5

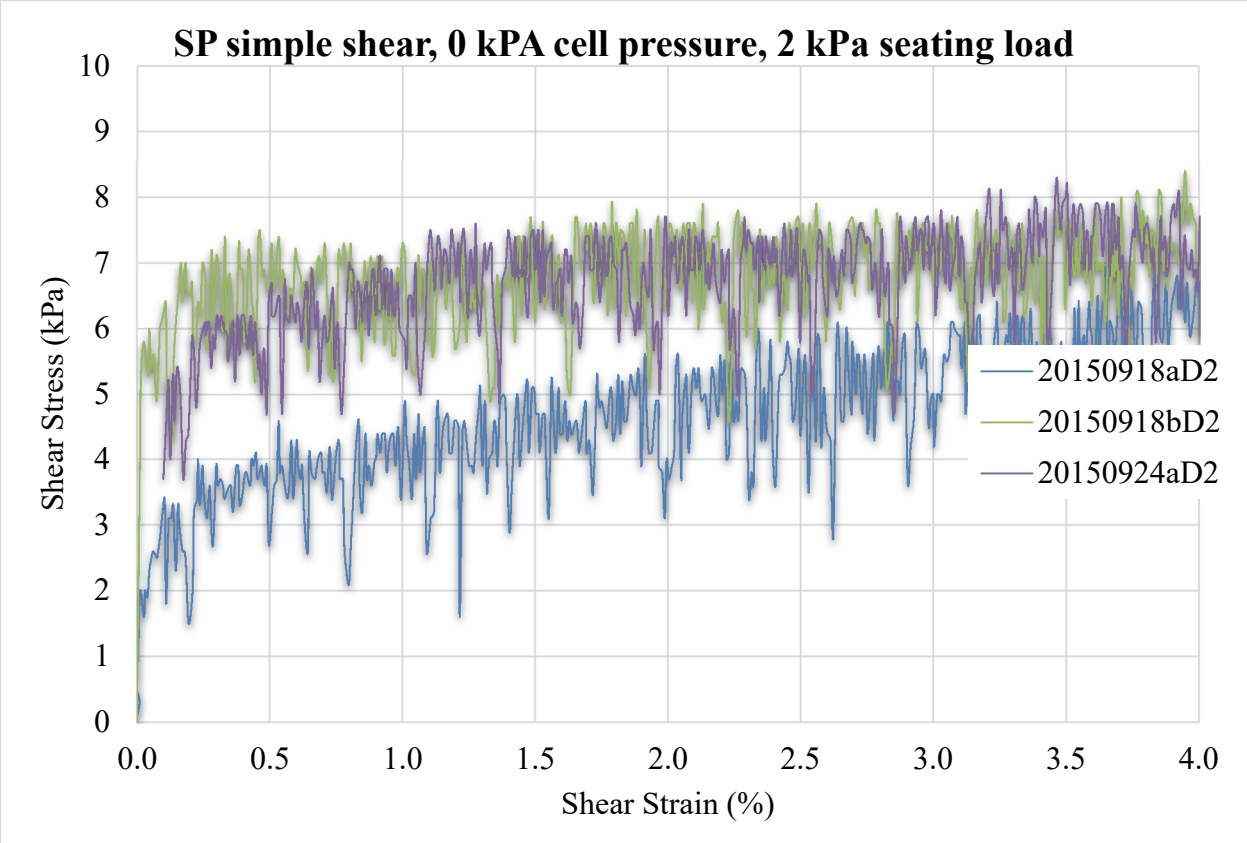
SP simple shear, 0 kPA cell pressure, 2 kPa seating load
Shear Stress (kPa)
Shear Strain (%)
0
1
2
3
4
5
6
7
8
9
10
0.0
0.5
1.0
1.5
2.0
2.5
3.0
3.5
4.0
20150918aD2
20150918bD2
20150924aD2

SM simple shear test data

Cell Pressure (kPa)	Shear Stress at Failure τ (kPa)	Test Name
500	300.8	20160211bCP500
500	299.1	20160212aCP500
500	301.8	20160217aCP500
250	164.7	20160202aCP250
250	158.4	20160209aCP250
250	155.9	20160211aCP250
100	64.6	20150316cCP100
100	65.3	20150318bCP100
100	63.3	20150323aCP100
75	53.2	20150622bCP75
75	54.9	20150622cCP75
75	57.4	20150623aCP75
50	36.6	20150312cCP50
50	37.8	20150318cCP50
50	43.5	20150319cCP50
25	33.6	20150312aCP25
25	32.8	20150312bCP25
25	27.5	20150318aCP25
15	23.6	20150617aCP15
15	21.4	20150618aCP15
15	22.6	20150618bCP15
0	8.9	20150318aCP0d5
0	10.5	20150324aCP0d5
0	13.0	20150324bCP0d5
0	9.4	20150319bCP0d2
0	8.1	20150320bCP0d2
0	8.9	20150323bCP0d2

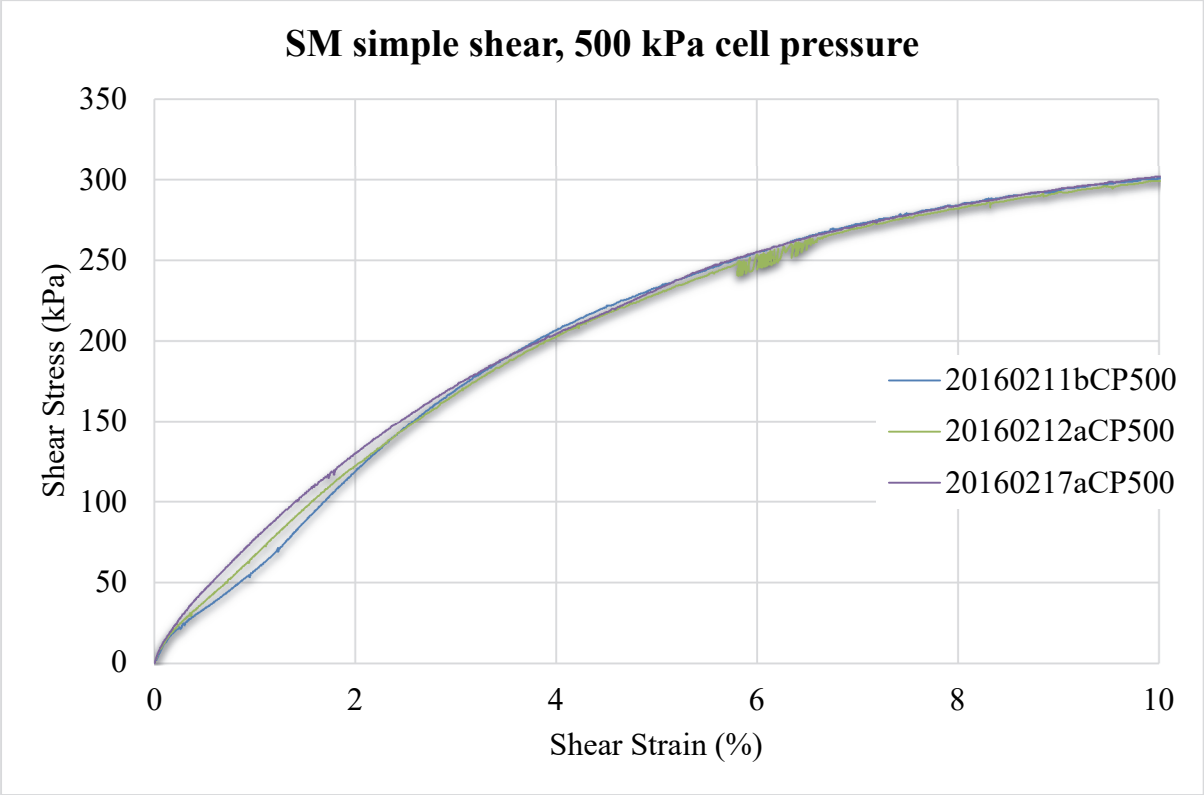
SM simple shear, 500 kPa cell pressure
Shear Stress (kPa)
Shear Strain (%)
0
50
100
150
200
250
300
350
0
2
4
6
8
10
20160211bCP500
20160212aCP500
20160217aCP500

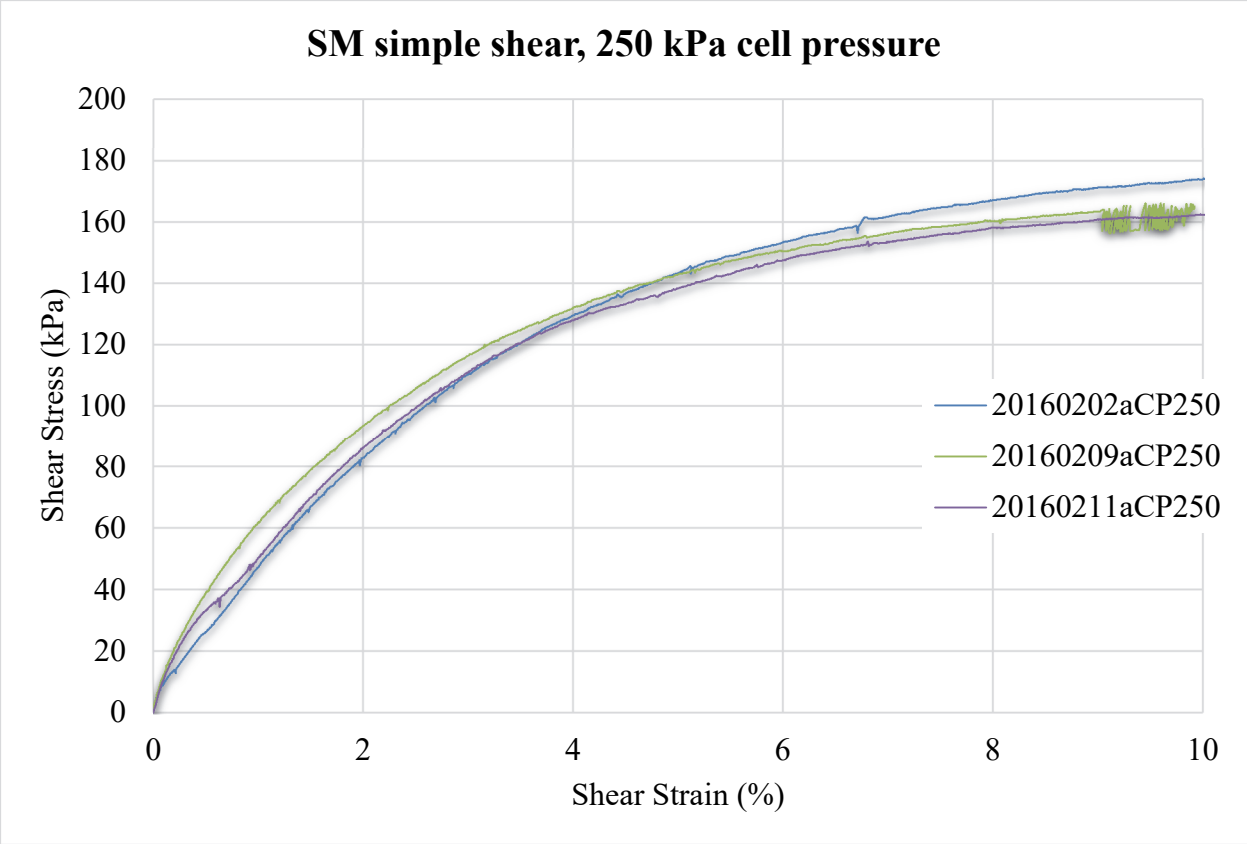
SM simple shear, 250 kPa cell pressure
Shear Stress (kPa)
Shear Strain (%)
0
20
40
60
80
100
120
140
160
180
200
0
2
4
6
8
10
20160202aCP250
20160209aCP250
20160211aCP250

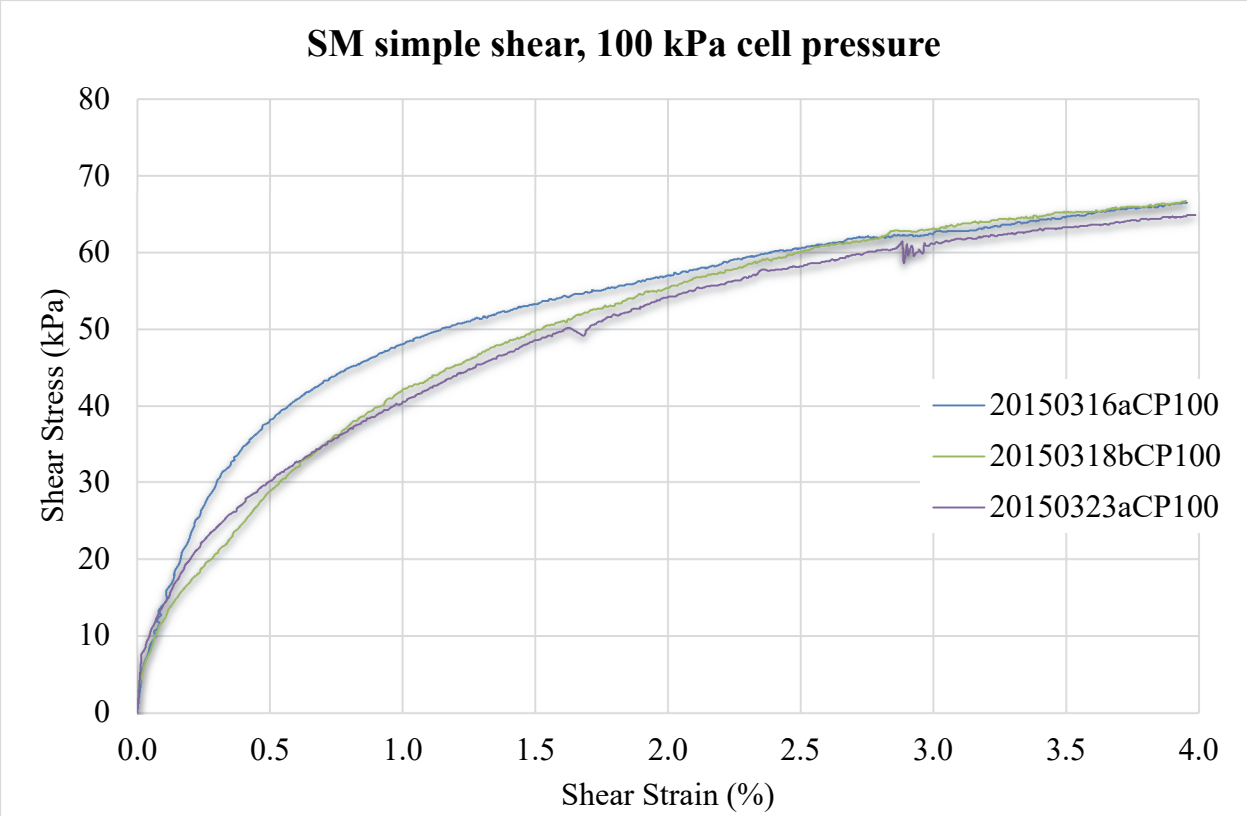
SM simple shear, 100 kPa cell pressure
Shear Stress (kPa)
Shear Strain (%)
0
10
20
30
40
50
60
70
80
0.0
0.5
1.0
1.5
2.0
2.5
3.0
3.5
4.0
20150316aCP100
20150318bCP100
20150323aCP100

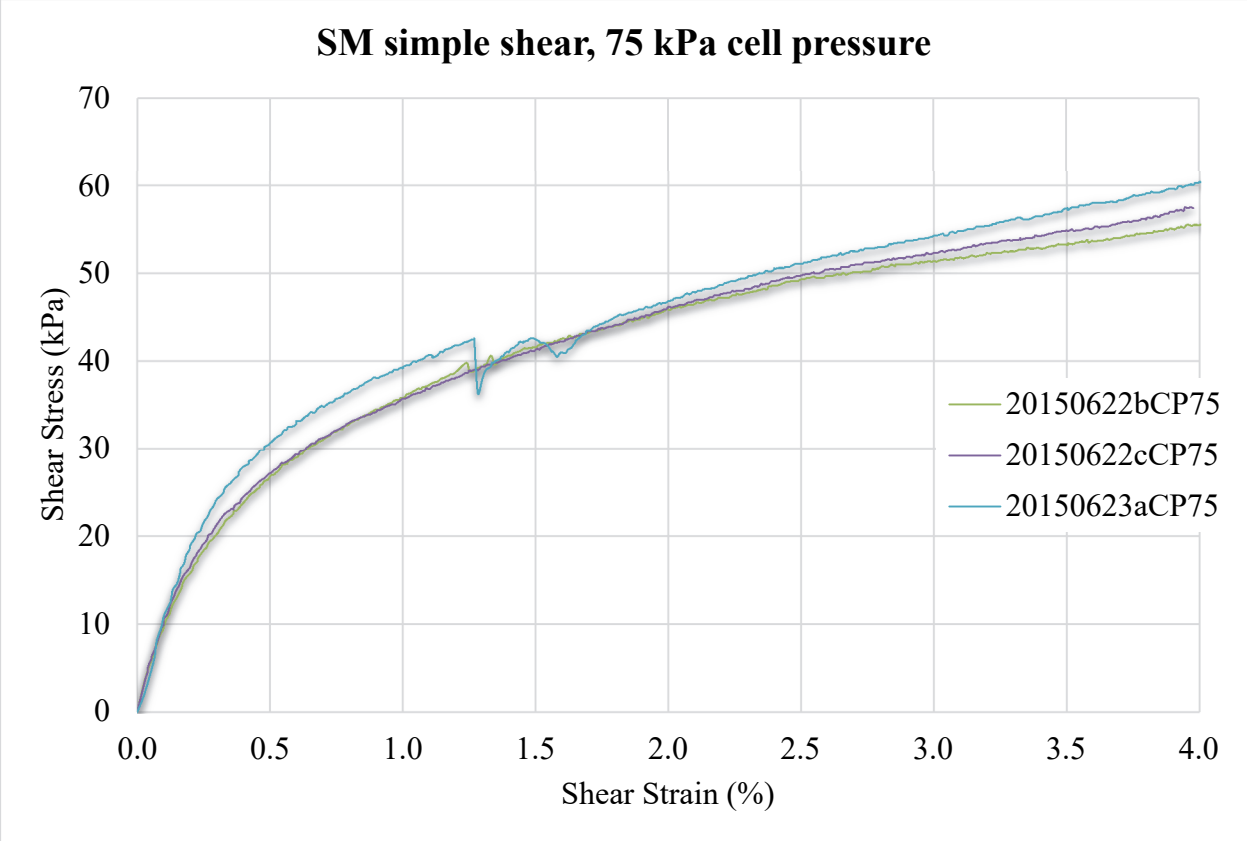
SM simple shear, 75 kPa cell pressure
Shear Stress (kPa)
Shear Strain (%)
0
10
20
30
40
50
60
70
0.0
0.5
1.0
1.5
2.0
2.5
3.0
3.5
4.0
20150622bCP75
20150622cCP75
20150623aCP75

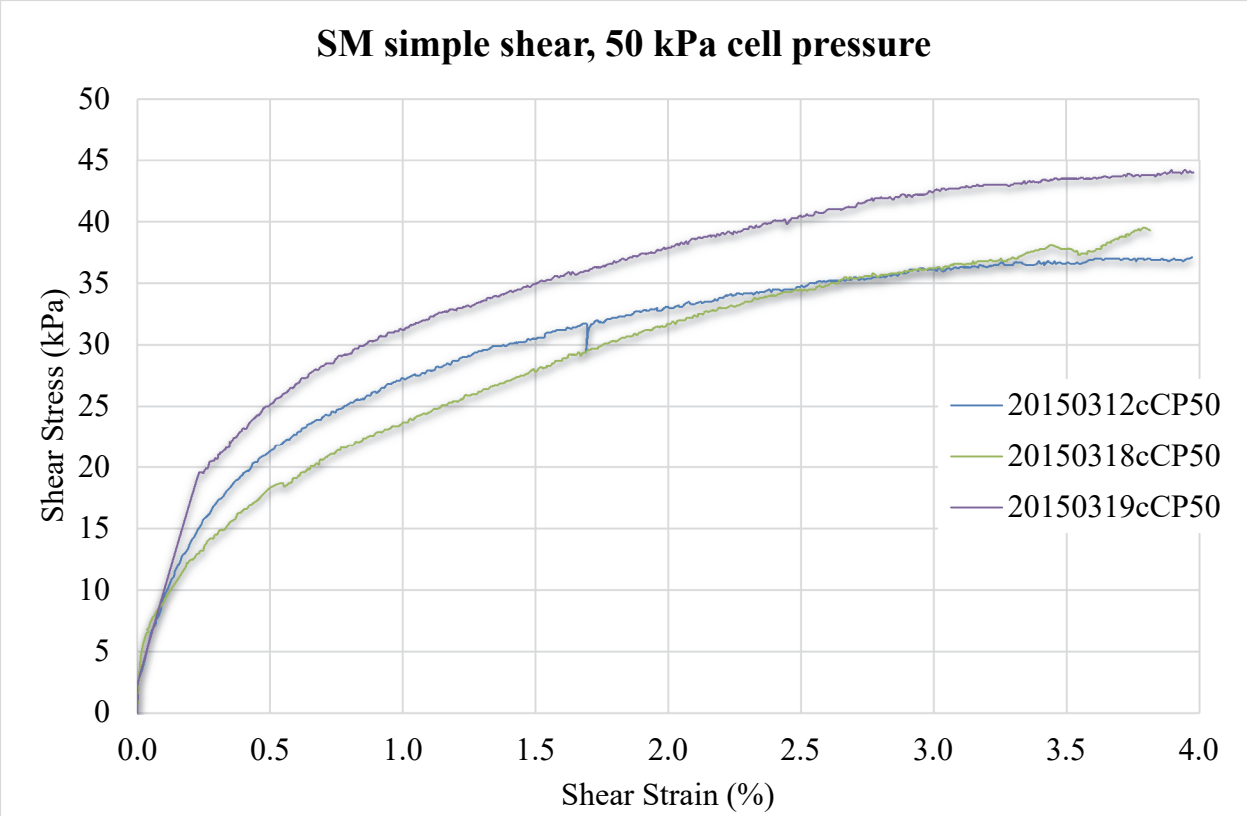
SM simple shear, 50 kPa cell pressure
Shear Stress (kPa)
Shear Strain (%)
0
5
10
15
20
25
30
35
40
45
50
0.0
0.5
1.0
1.5
2.0
2.5
3.0
3.5
4.0
20150312cCP50
20150318cCP50
20150319cCP50

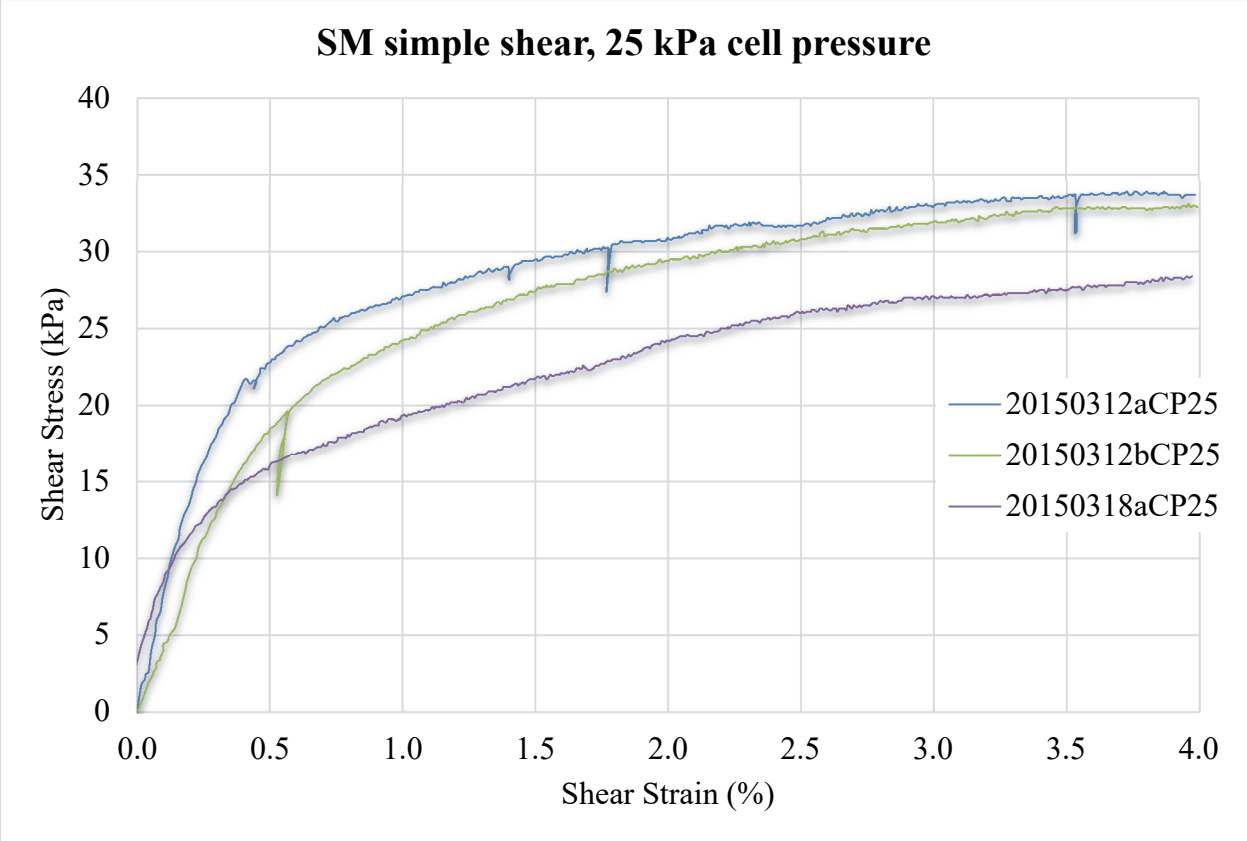
SM simple shear, 25 kPa cell pressure
Shear Stress (kPa)
Shear Strain (%)
0
5
10
15
20
25
30
35
40
0.0
0.5
1.0
1.5
2.0
2.5
3.0
3.5
4.0
20150312aCP25
20150312bCP25
20150318aCP25

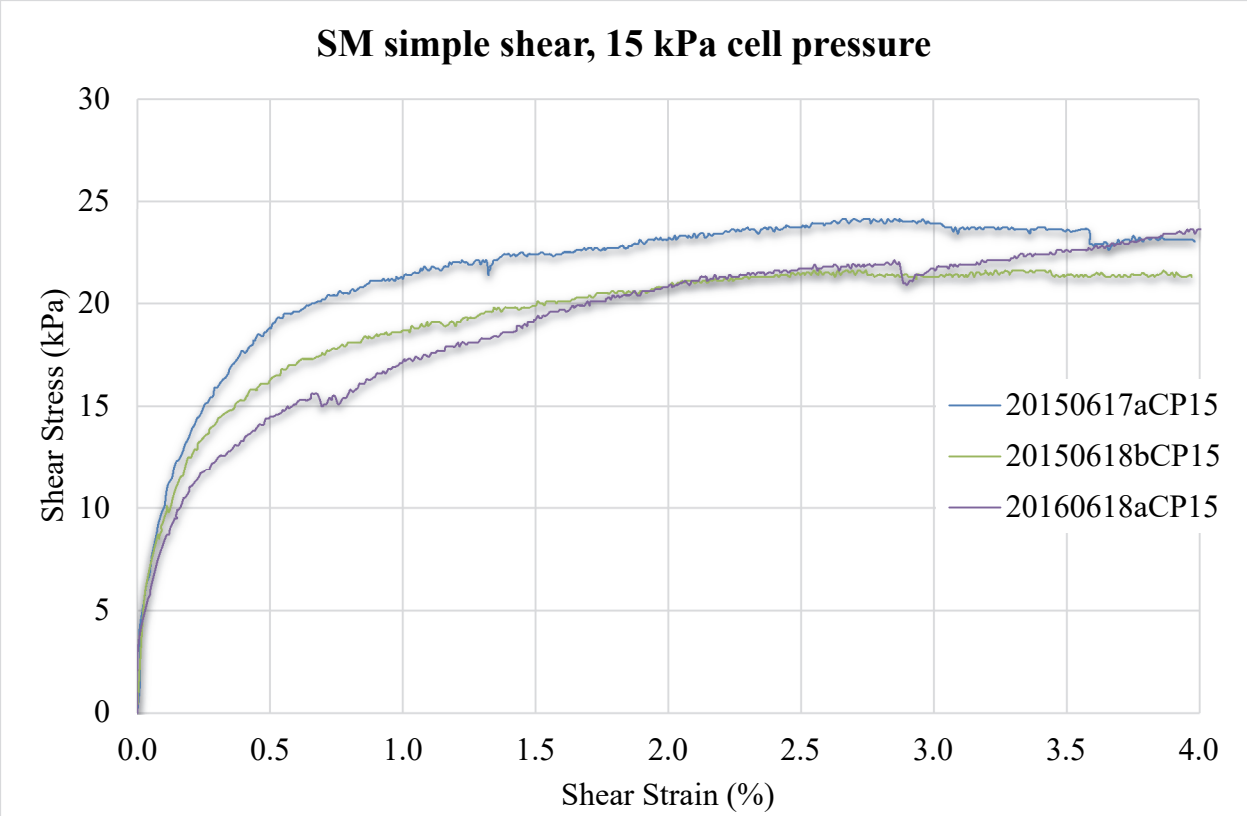
SM simple shear, 15 kPa cell pressure
Shear Stress (kPa)
Shear Strain (%)
0
5
10
15
20
25
30
0.0
0.5
1.0
1.5
2.0
2.5
3.0
3.5
4.0
20150617aCP15
20150618bCP15
20160618aCP15

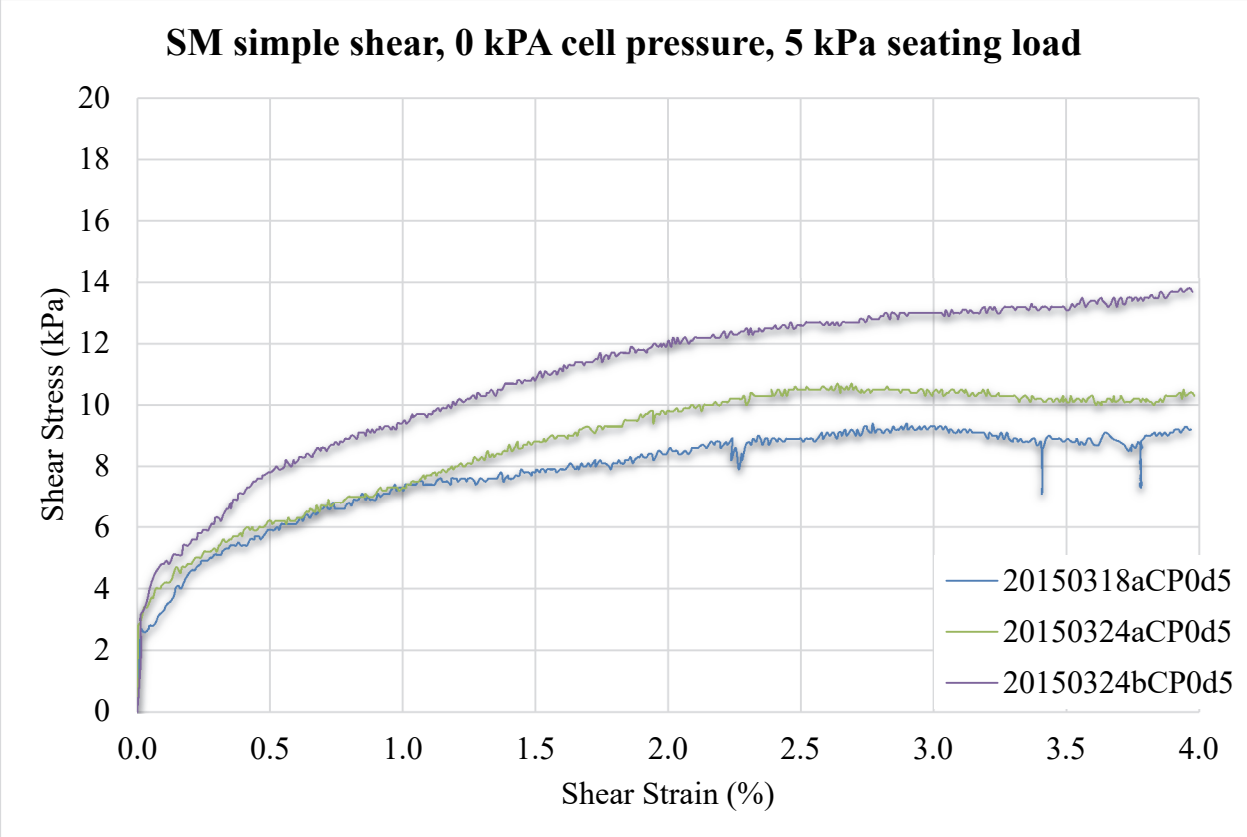
SM simple shear, 0 kPA cell pressure, 5 kPa seating load
Shear Stress (kPa)
Shear Strain (%)
0
2
4
6
8
10
12
14
16
18
20
0.0
0.5
1.0
1.5
2.0
2.5
3.0
3.5
4.0
20150318aCP0d5
20150324aCP0d5
20150324bCP0d5

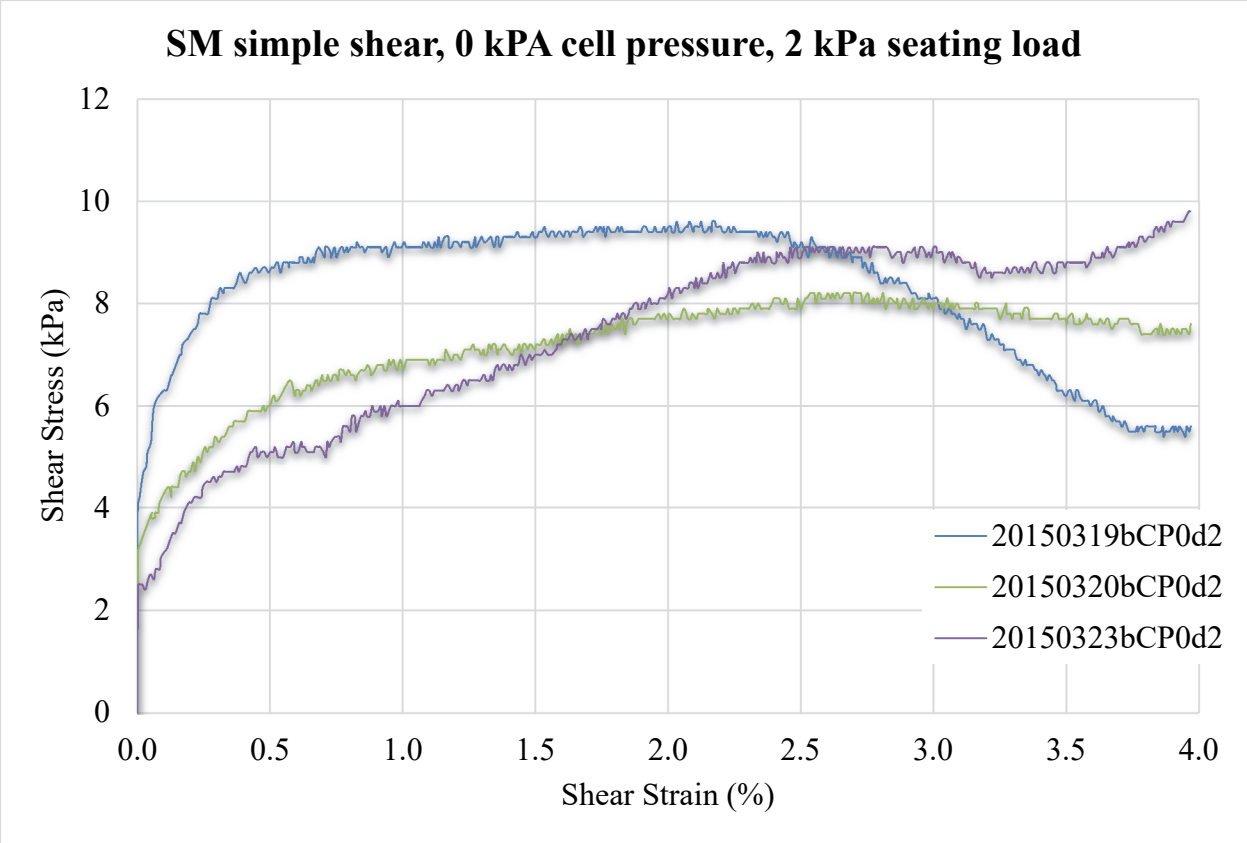
SM simple shear, 0 kPA cell pressure, 2 kPa seating load
Shear Stress (kPa)
Shear Strain (%)
0
2
4
6
8
10
12
0.0
0.5
1.0
1.5
2.0
2.5
3.0
3.5
4.0
20150319bCP0d2
20150320bCP0d2
20150323bCP0d2

ML simple shear test data

Cell Pressure (kPa)	Shear Stress at Failure τ (kPa)	Test Name
500	264.0	20160222bCP500
500	261.0	20160223aCP500
500	273.4	20160225aCP500
250	142.1	20160225bCP250
250	145.4	20160226aCP250
250	138.2	20160301aCP250
100	55.4	20151007aCP100
100	57.2	20151007bCP100
100	56.6	20151008aCP100
75	48.2	20151014aCP75
75	49.4	20151015bCP75
75	49.6	20151125aCP75
50	42.1	20151008bCP50
50	38.9	20151019aCP50
50	34.3	20151019bCP50
25	24.4	20151013aCP25
25	25.8	20151013bCP25
25	27.7	20151015aCP25
15	16.5	20151020aCP15
15	19.5	20151109bCP15
15	21.1	20151215aCP15
0	16.1	20151028aCP0d5
0	13.7	20151106aCP0d5
0	13.7	20160809aCP0d5
0	11.6	20151109aCP0d2
0	10.9	20151120aCP0d2
0	13.1	20160805aCP0d2

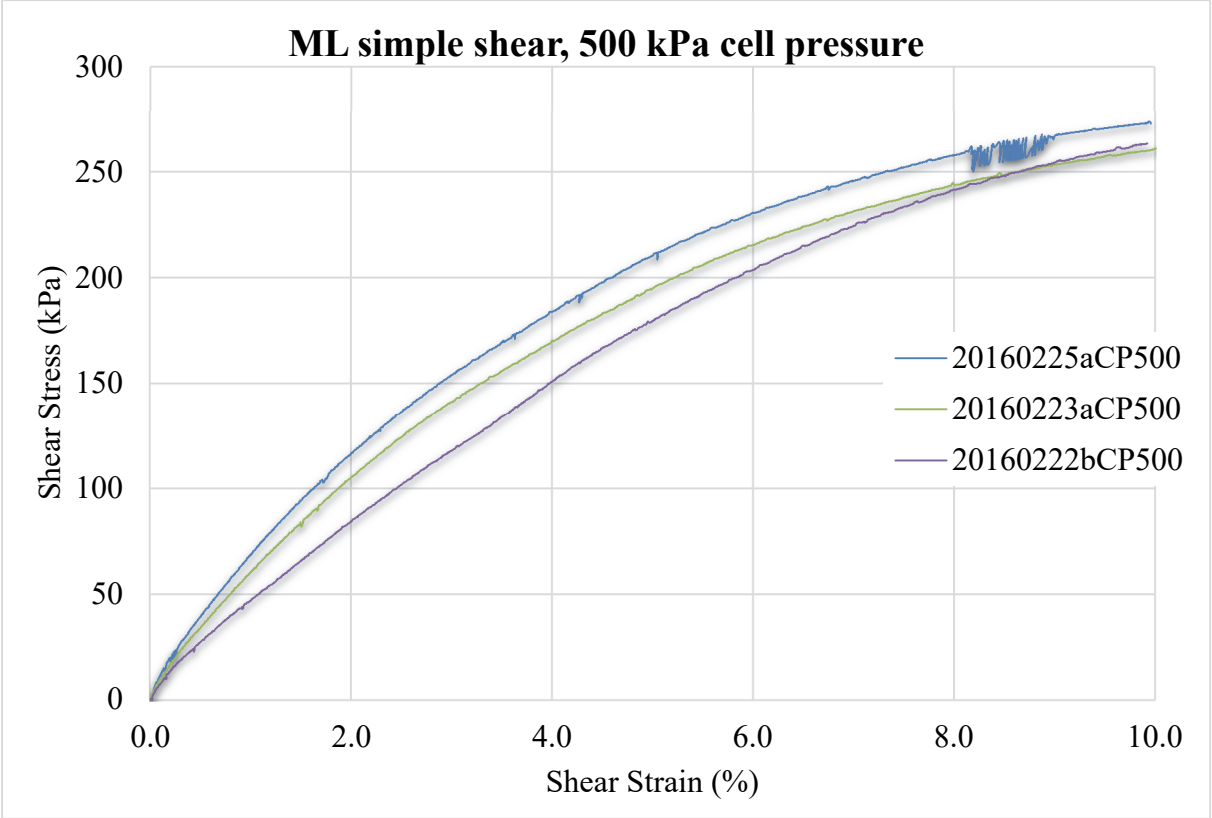
ML simple shear, 500 kPa cell pressure
Shear Stress (kPa)
300
250
200
150
100
50
0
0.0
2.0
4.0
6.0
8.0
10.0
Shear Strain (%)
20160225aCP500
20160223aCP500
20160222bCP500

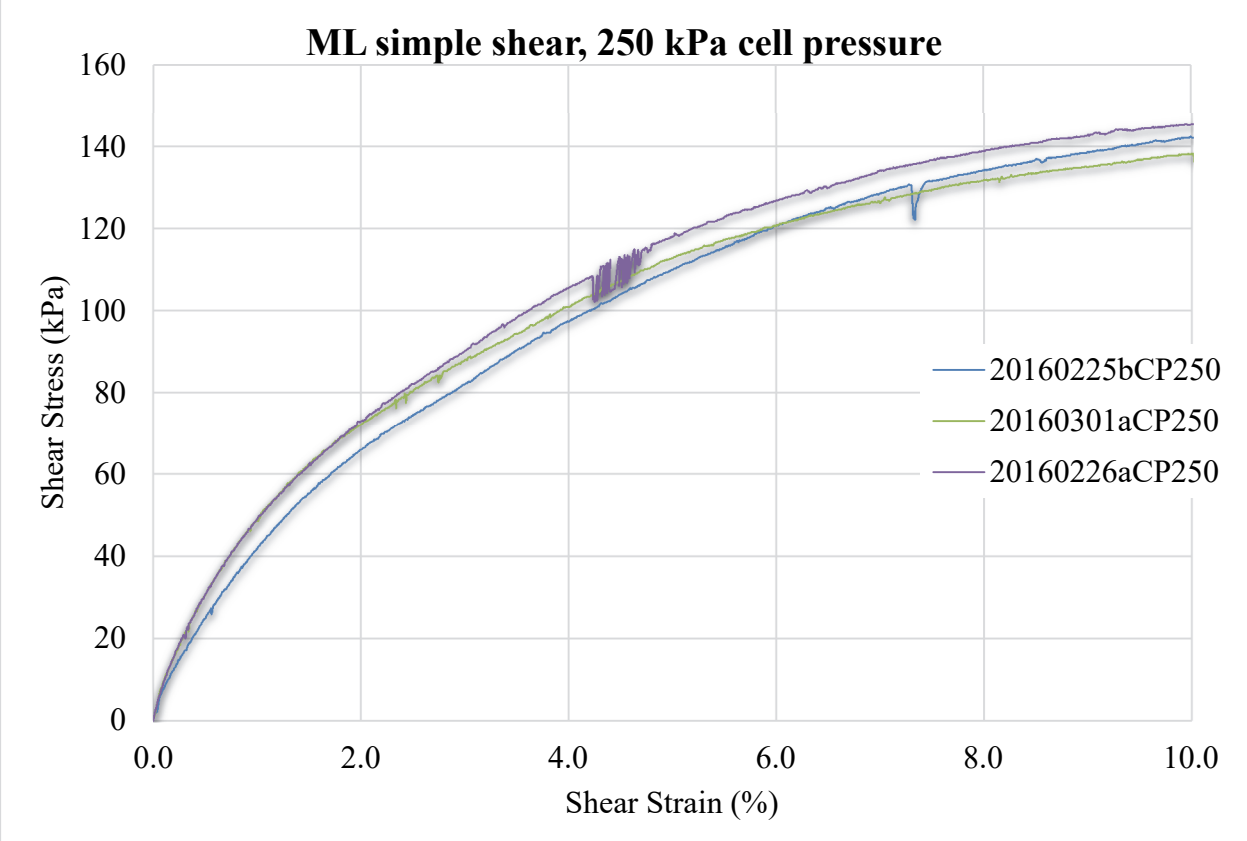
ML simple shear, 250 kPa cell pressure
Shear Stress (kPa)
160
140
120
100
80
60
40
20
0
0.0
2.0
4.0
6.0
8.0
10.0
Shear Strain (%)
20160225bCP250
20160301aCP250
20160226aCP250

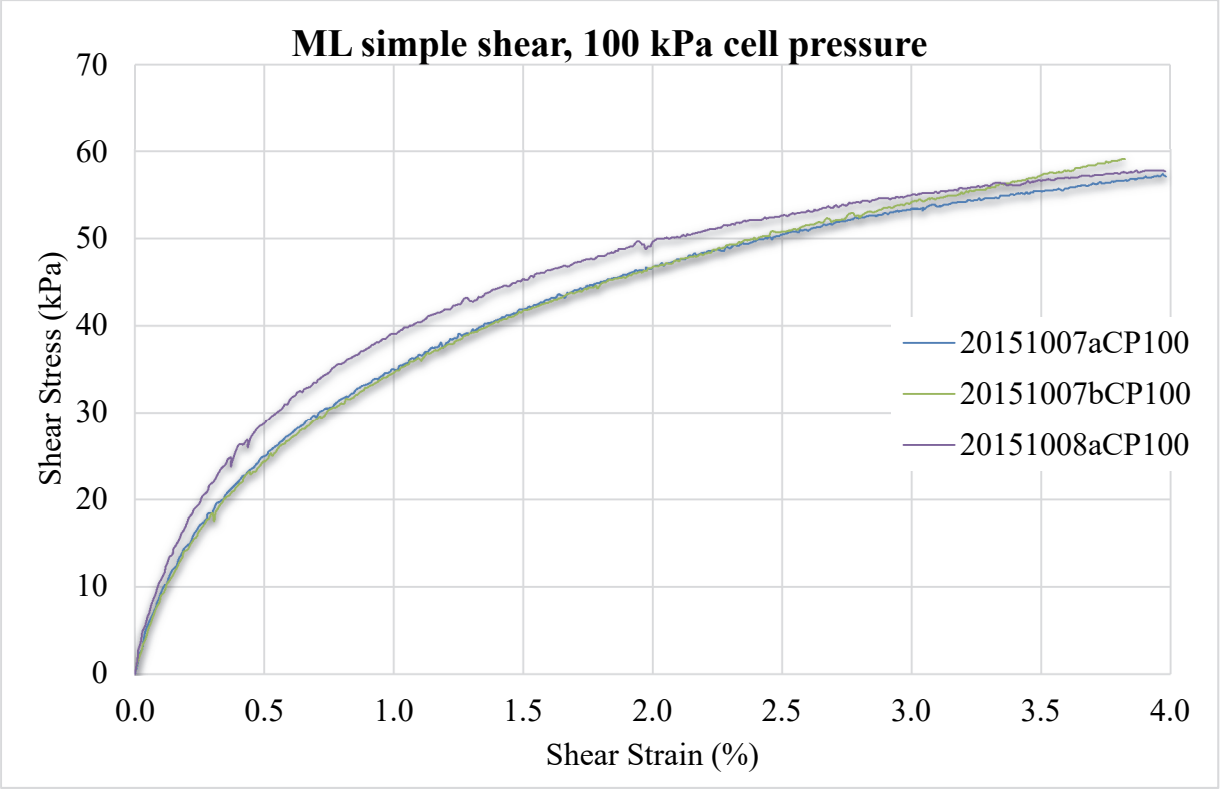
ML simple shear, 100 kPa cell pressure
Shear Stress (kPa)
70
60
50
40
30
20
10
0
0.0
0.5
1.0
1.5
2.0
2.5
3.0
3.5
4.0
Shear Strain (%)
20151007aCP100
20151007bCP100
20151008aCP100

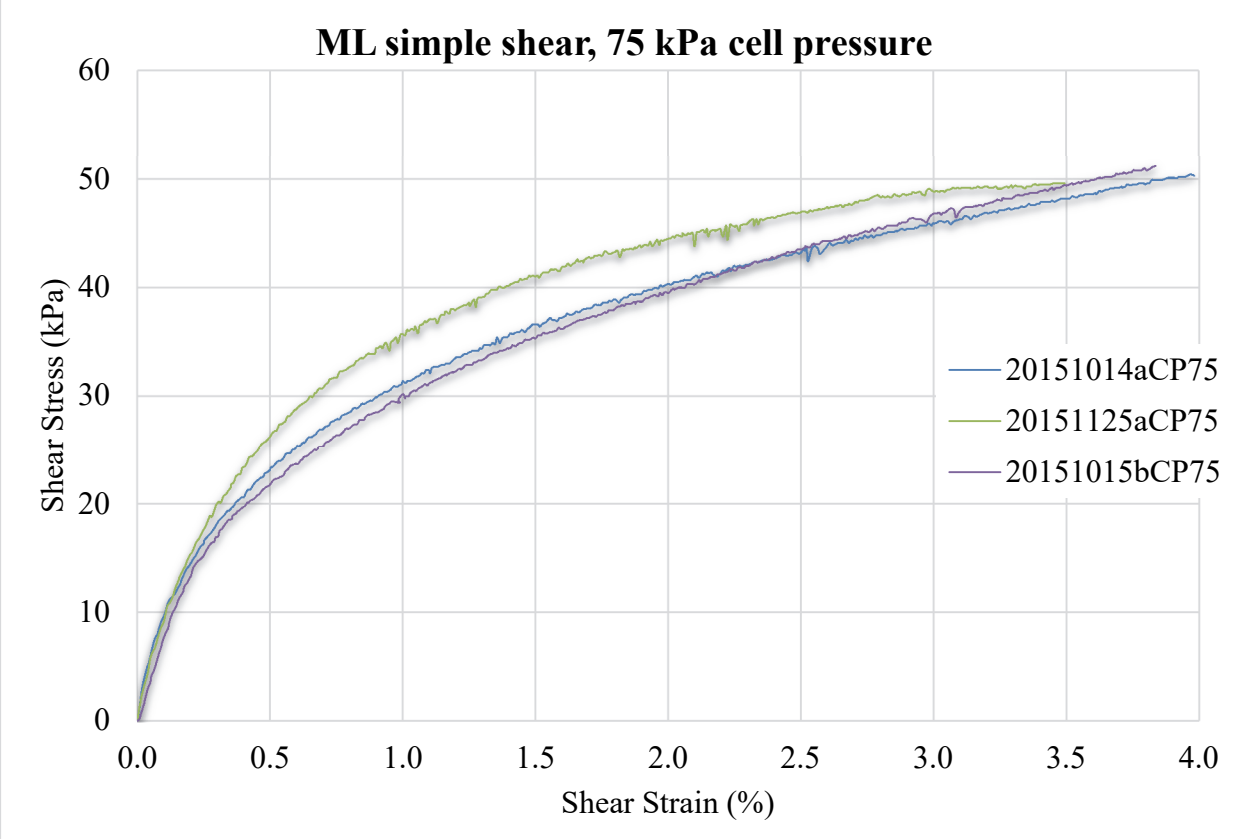
ML simple shear, 75 kPa cell pressure
Shear Stress (kPa)
60
50
40
30
20
10
0
0.0
0.5
1.0
1.5
2.0
2.5
3.0
3.5
4.0
Shear Strain (%)
20151014aCP75
20151125aCP75
20151015bCP75

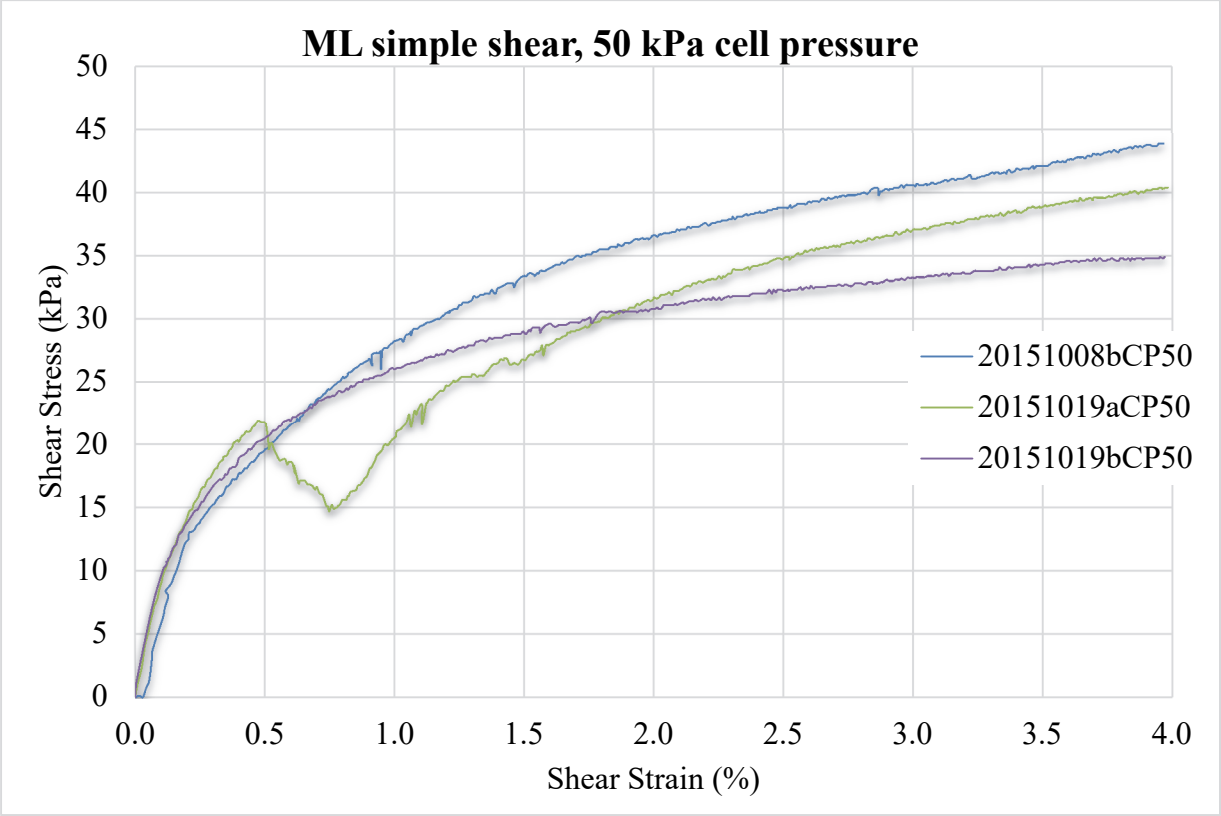
ML simple shear, 50 kPa cell pressure
Shear Stress (kPa)
Shear Strain (%)
0
5
10
15
20
25
30
35
40
45
50
0.0
0.5
1.0
1.5
2.0
2.5
3.0
3.5
4.0
20151008bCP50
20151019aCP50
20151019bCP50

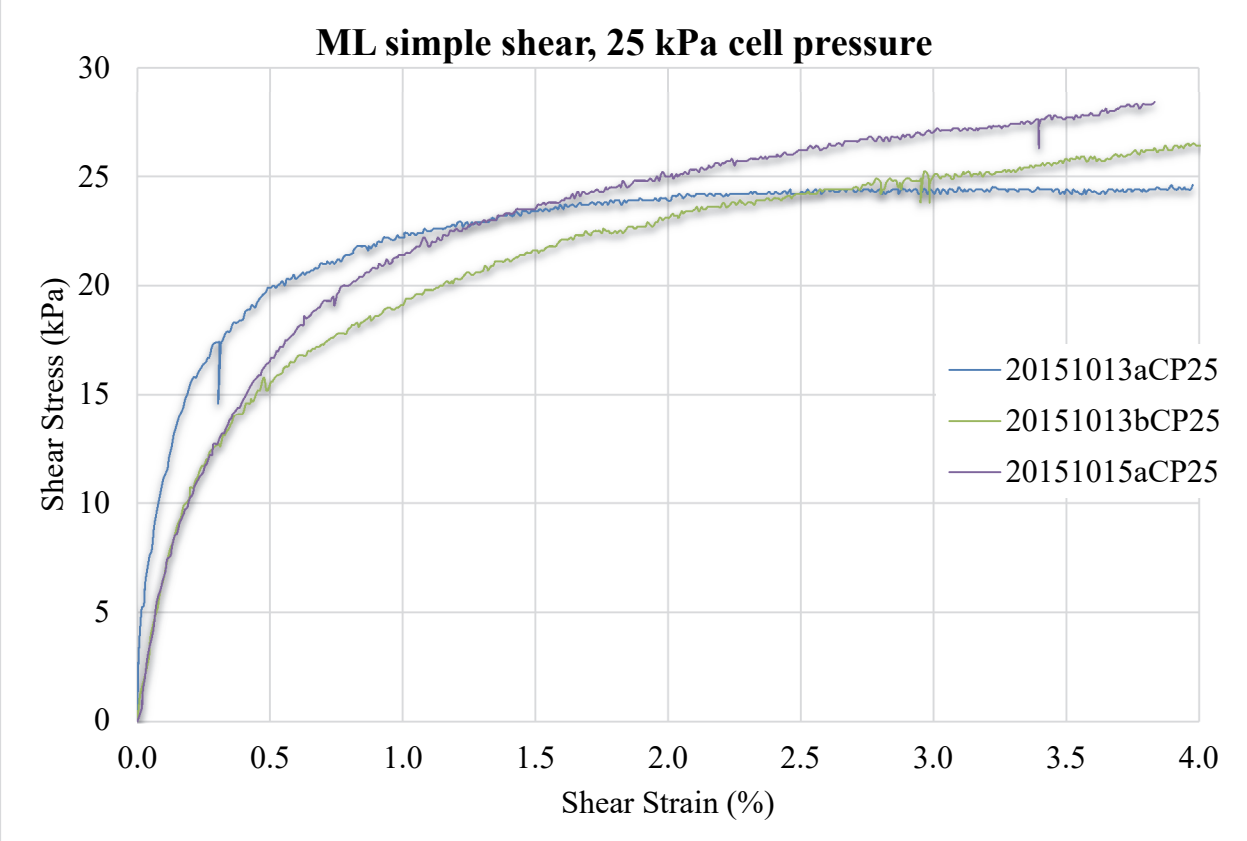
ML simple shear, 25 kPa cell pressure
Shear Stress (kPa)
Shear Strain (%)
0
5
10
15
20
25
30
0.0
0.5
1.0
1.5
2.0
2.5
3.0
3.5
4.0
20151013aCP25
20151013bCP25
20151015aCP25

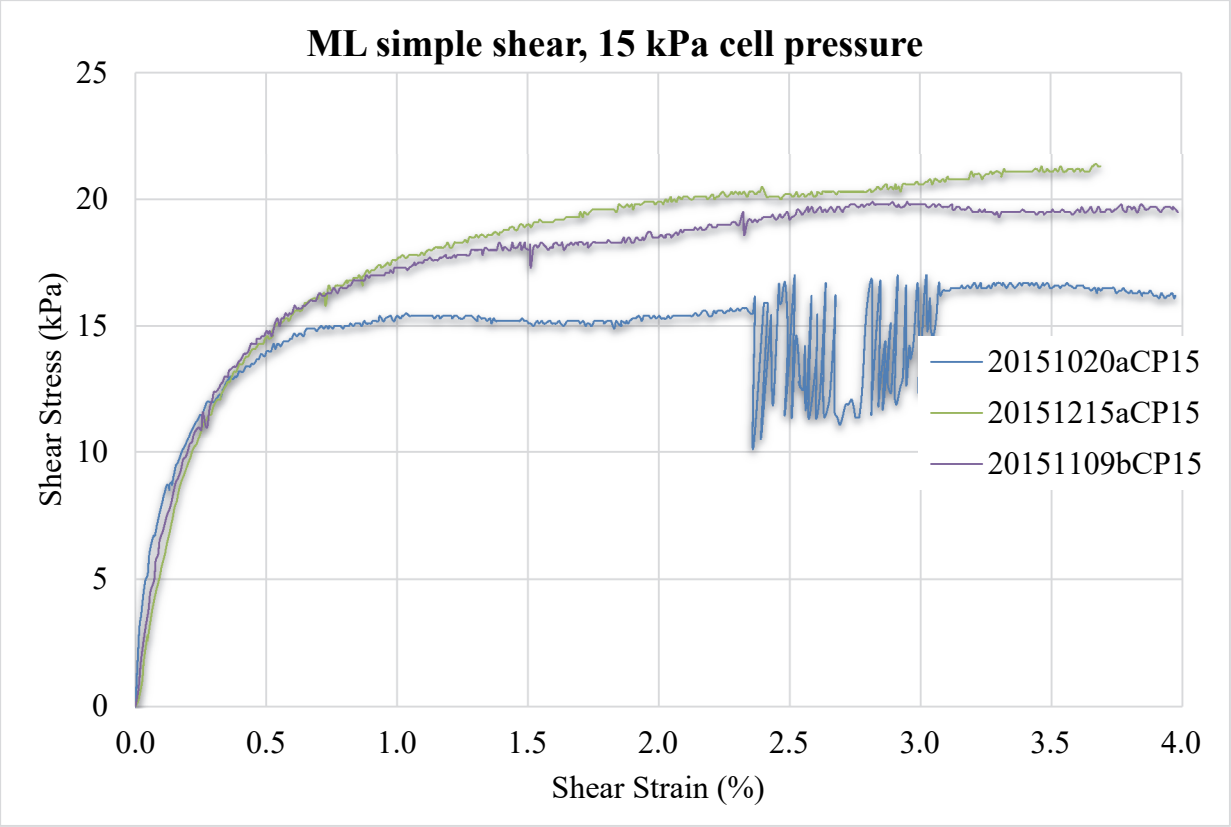
ML simple shear, 15 kPa cell pressure
Shear Stress (kPa)
Shear Strain (%)
0
5
10
15
20
25
0.0
0.5
1.0
1.5
2.0
2.5
3.0
3.5
4.0
20151020aCP15
20151215aCP15
20151109bCP15

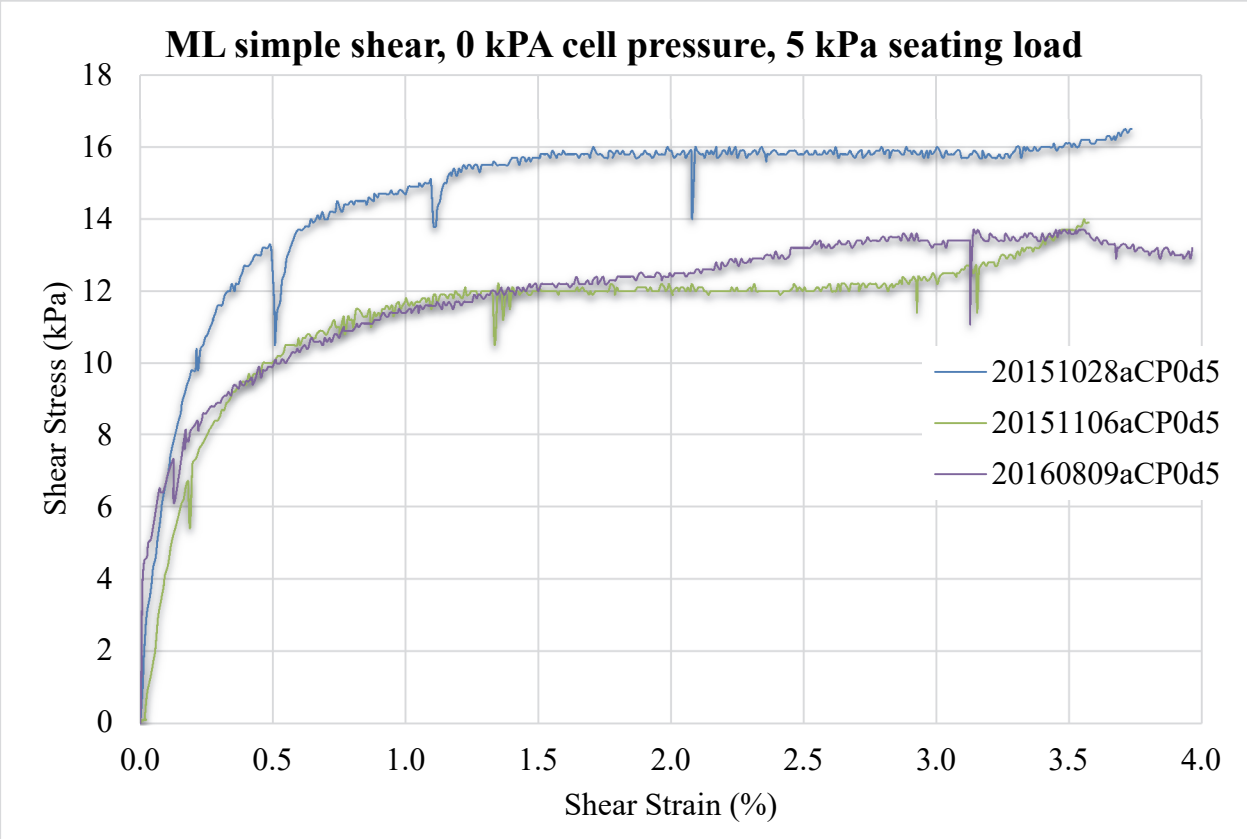
ML simple shear, 0 kPA cell pressure, 5 kPa seating load
Shear Stress (kPa)
Shear Strain (%)
0
2
4
6
8
10
12
14
16
18
0.0
0.5
1.0
1.5
2.0
2.5
3.0
3.5
4.0
20151028aCP0d5
20151106aCP0d5
20160809aCP0d5

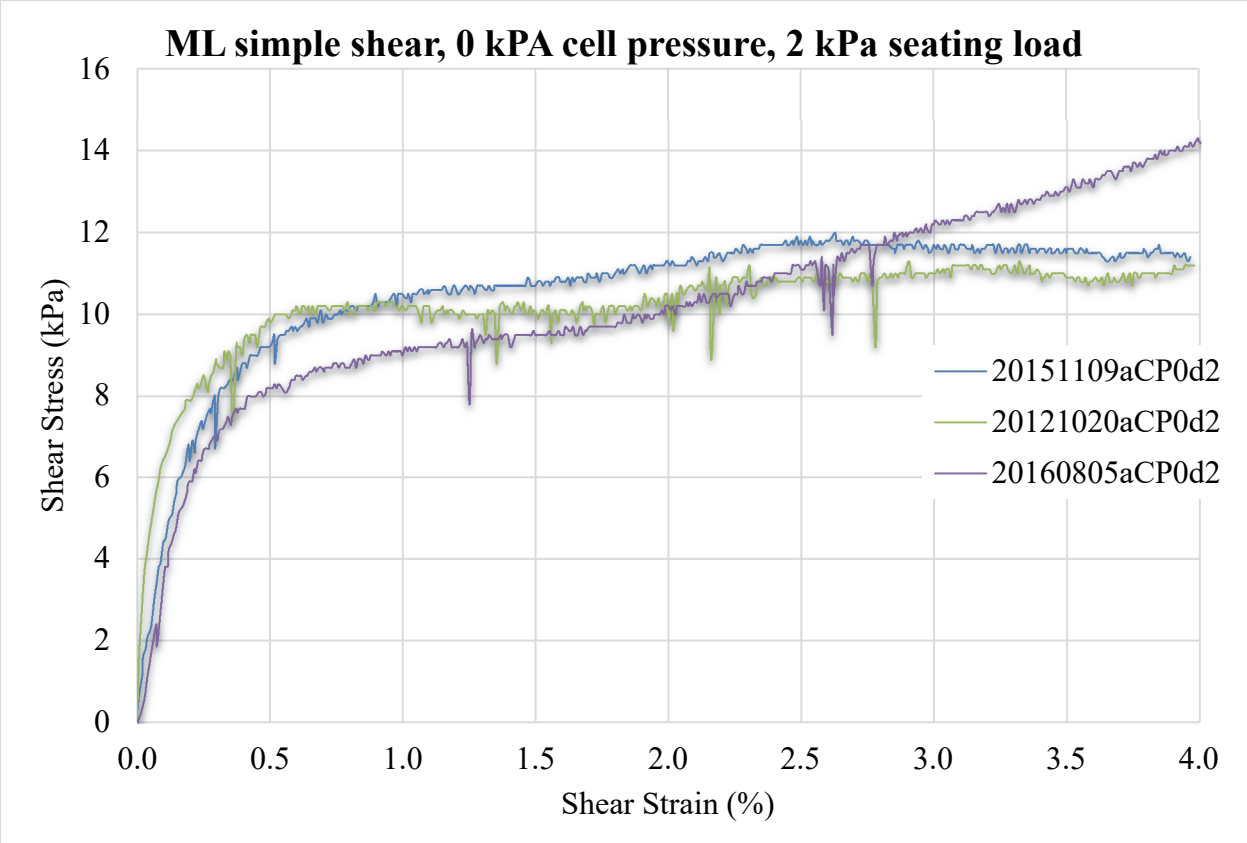
ML simple shear, 0 kPA cell pressure, 2 kPa seating load
Shear Stress (kPa)
Shear Strain (%)
0
2
4
6
8
10
12
14
16
0.0
0.5
1.0
1.5
2.0
2.5
3.0
3.5
4.0
20151109aCP0d2
20121020aCP0d2
20160805aCP0d2

SP ring shear test data

Specimen	Cell Pressure kPa	Shear Stress at failure kPa	Cyclic Strain at failure %	Failure Cycle	Shear Stress at critical state kPa	Cyclic Strain at critical state %
CP100-A	100	88.52	0.21264	4	100.45	0.20983
CP100-B	100	90.10	0.21231	4	102.94	0.20967
CP100-C	100	89.83	0.21217	4	102.55	0.20967
CP100-D	100	88.96	0.21225	3	103.02	0.20967
CP100-E	100	87.24	0.21294	3	106.60	0.21113
CP100-F	100	81.01	0.21244	3	97.07	0.21112
CP100-G	100	84.70	0.21231	4	97.36	0.20967
CP100-H	100	80.80	0.21242	4	93.24	0.20986
CP75-A	75	66.00	0.21275	4	74.88	0.21019
CP75-B	75	60.06	0.21286	3	76.99	0.21164
CP75-C	75	61.53	0.21281	4	73.56	0.21019
CP75-D	75	72.47	0.21292	4	79.55	0.21056
CP75-E	75	72.05	0.21261	4	82.12	0.21006
CP75-F	75	86.28	0.21306	4	95.88	0.21136
CP75-G	75	74.08	0.21306	3	89.03	0.21156
CP75-H	75	73.07	0.21256	4	83.44	0.20992
CP75-I	75	76.10	0.21256	3	89.11	0.21144
CP75-J	75	71.88	0.21275	4	79.99	0.21017
CP50-A	50	54.83	0.21289	4	64.18	0.21044
CP50-B	50	43.90	0.21311	3	56.75	0.21036
CP50-C	50	43.90	0.21311	4	62.11	0.21044
CP50-D	50	50.32	0.21292	4	58.31	0.21036
CP50-E	50	49.00	0.21308	4	55.09	0.21050
CP50-F	50	52.84	0.21292	3	66.65	0.21031
CP25-A	25	28.51	0.21375	4	38.21	0.21225
CP25-B	25	28.77	0.21294	4	33.75	0.21181
CP25-C	25	25.11	0.21387	3	33.39	0.21108
CP25-D	25	37.63	0.21331	3	41.14	0.21075
CP25-E	25	29.47	0.21350	4	34.43	0.21086

Specimen	Cell Pressure kPa	Shear Stress at failure kPa	Cyclic Strain at failure %	Failure Cycle	Shear Stress at critical state kPa	Cyclic Strain at critical state %
CP25-G	25	35.39	0.21394	4	41.83	0.21239
CP25-H	25	34.40	0.21331	3	47.10	0.21075
CP25-I	25	35.82	0.21325	3	43.63	0.21125
CP25-J	25	30.59	0.21325	4	36.73	0.21083
CP10-A	10	18.99	0.21350	4	22.95	0.21106
CP10-B	10	19.26	0.21350	3	27.27	0.21244
CP10-C	10	12.81	0.21400	3	17.83	0.21261
CP10-D	10	18.74	0.21394	3	28.91	0.21244
CP10-E	10	21.23	0.21350	4	24.31	0.21250
CP10-F	10	17.33	0.21350	3	21.19	0.21250
CP10-G	10	16.16	0.21325	5	20.87	0.21111
CP10-H	10	26.74	0.21331	4	34.32	0.21089
CP10-I	10	13.66	0.21400	4	19.30	0.21114

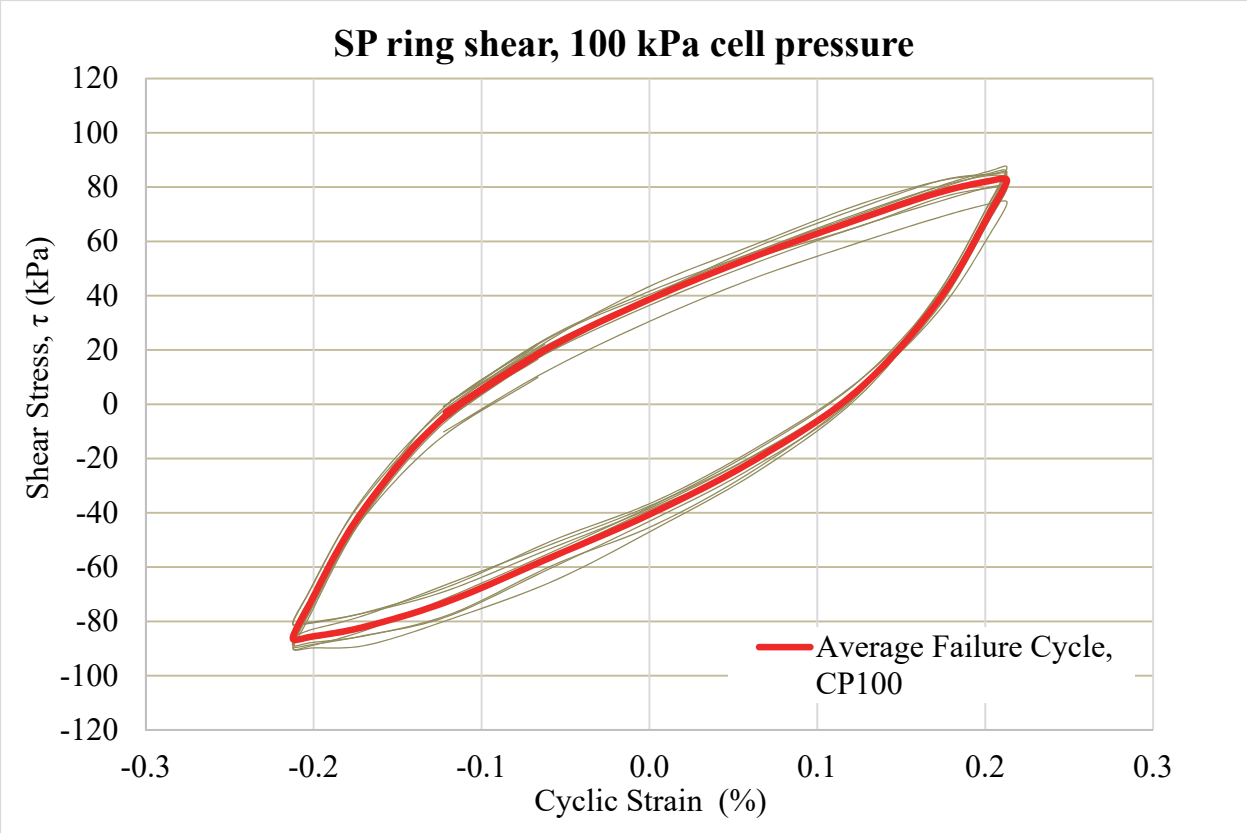
SP ring shear, 100 kPa cell pressure
Shear Stress, τ (kPa)
120
100
80
60
40
20
0
-20
-40
-60
-80
-100
-120
-0.3
-0.2
-0.1
0.0
0.1
0.2
0.3
Cyclic Strain (%)
Average Failure Cycle, CP100

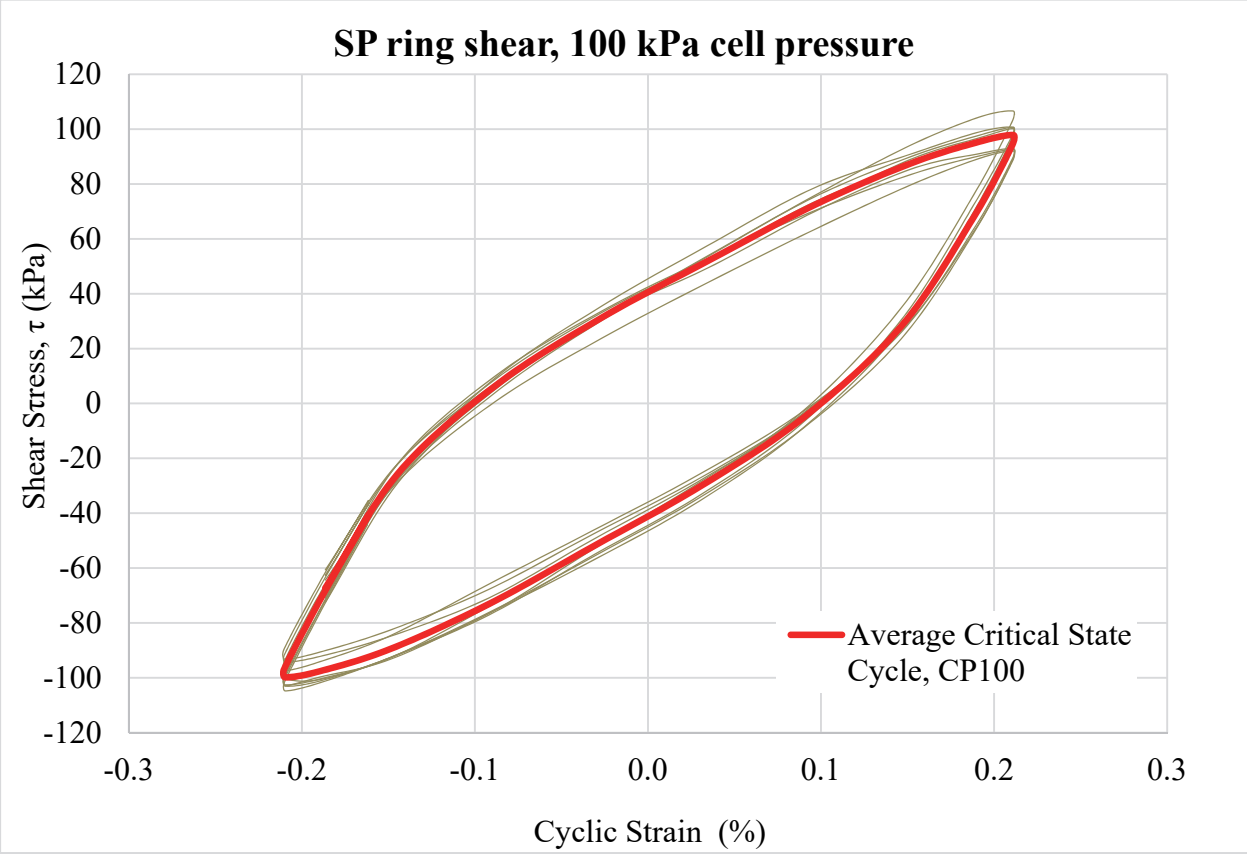
SP ring shear, 100 kPa cell pressure
Shear Stress, τ (kPa)
120
100
80
60
40
20
0
-20
-40
-60
-80
-100
-120
-0.3
-0.2
-0.1
0.0
0.1
0.2
0.3
Cyclic Strain (%)
Average Critical State Cycle, CP100

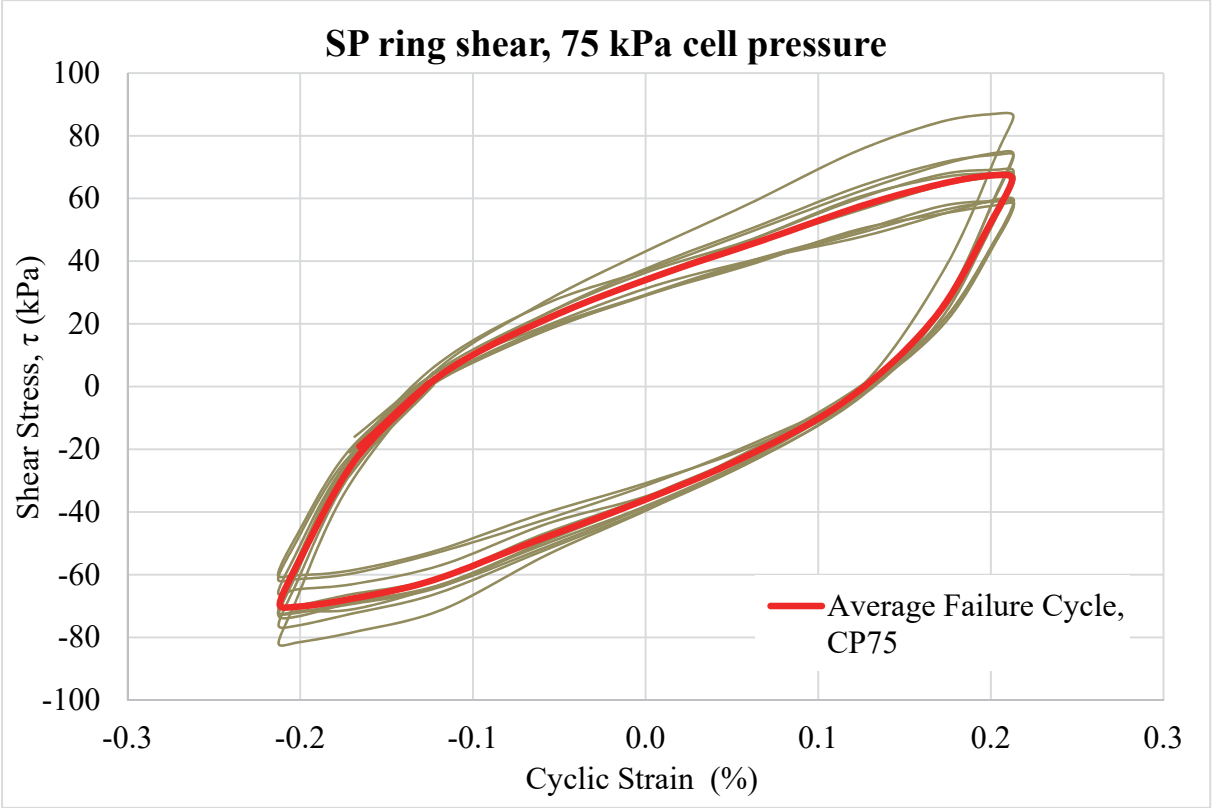
SP ring shear, 75 kPa cell pressure
Shear Stress, τ (kPa)
100
80
60
40
20
0
-20
-40
-60
-80
-100
-0.3
-0.2
-0.1
0.0
0.1
0.2
0.3
Cyclic Strain (%)
Average Failure Cycle, CP75

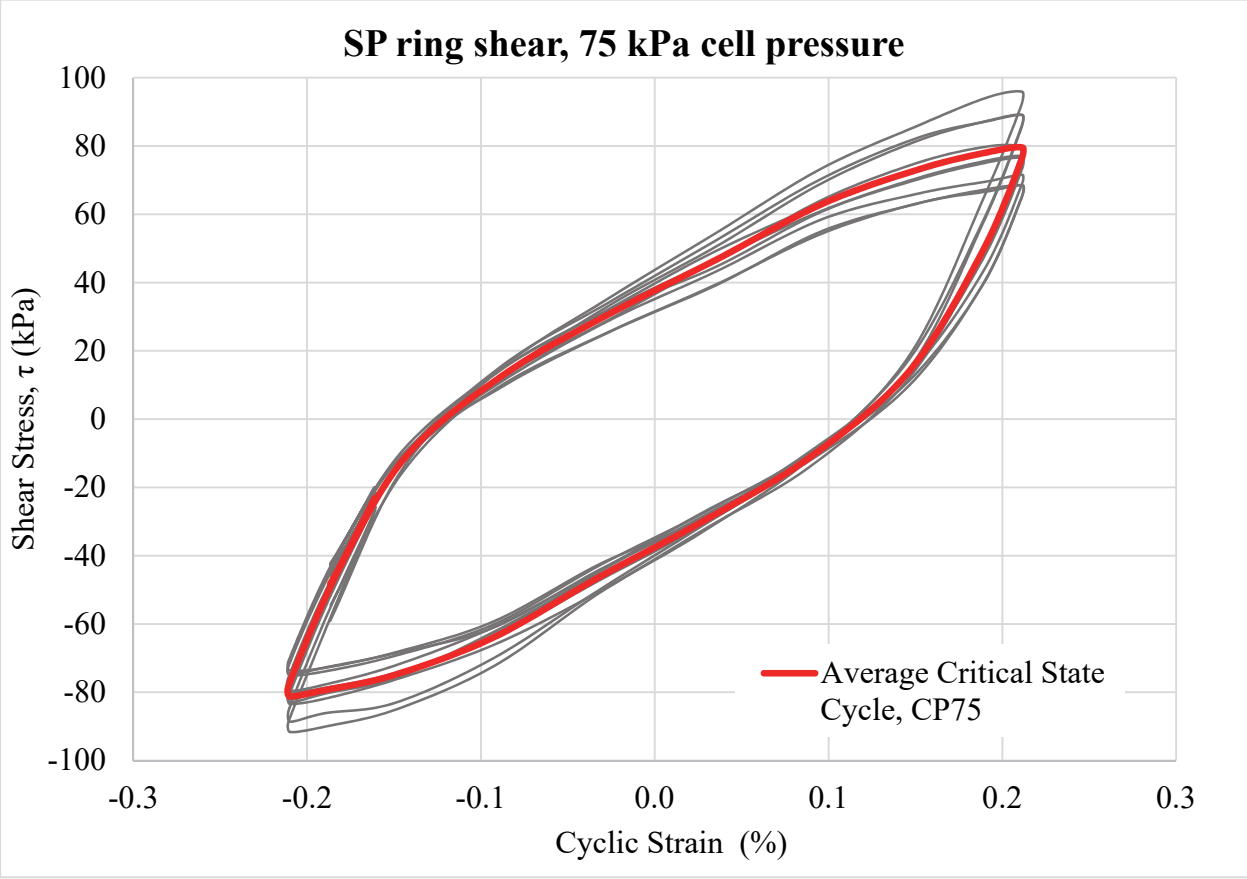
SP ring shear, 75 kPa cell pressure
Shear Stress, τ (kPa)
100
80
60
40
20
0
-20
-40
-60
-80
-100
-0.3
-0.2
-0.1
0.0
0.1
0.2
0.3
Cyclic Strain (%)
Average Critical State Cycle, CP75

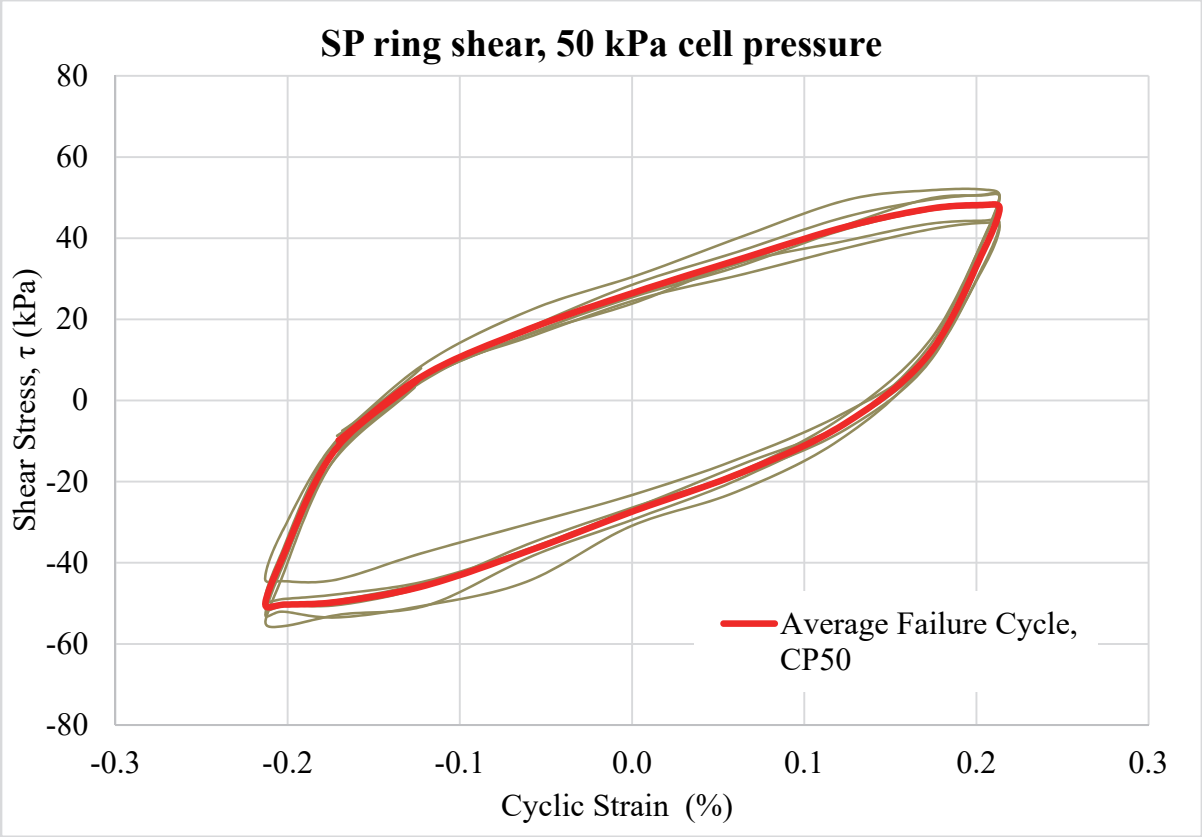
SP ring shear, 50 kPa cell pressure
Shear Stress, τ (kPa)
80
60
40
20
0
-20
-40
-60
-80
-0.3
-0.2
-0.1
0.0
0.1
0.2
0.3
Cyclic Strain (%)
Average Failure Cycle, CP50

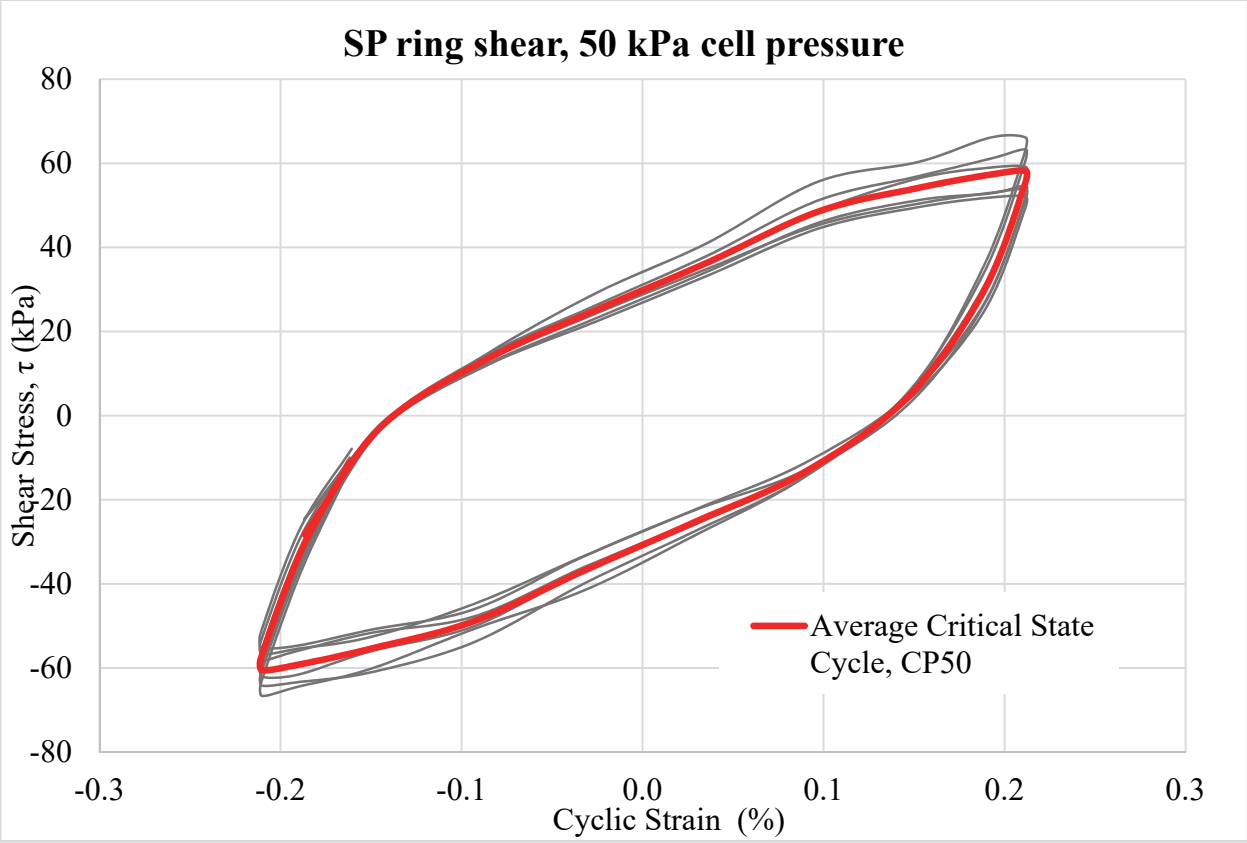
SP ring shear, 50 kPa cell pressure
Shear Stress, τ (kPa)
80
60
40
20
0
-20
-40
-60
-80
-0.3
-0.2
-0.1
0.0
0.1
0.2
0.3
Cyclic Strain (%)
Average Critical State Cycle, CP50

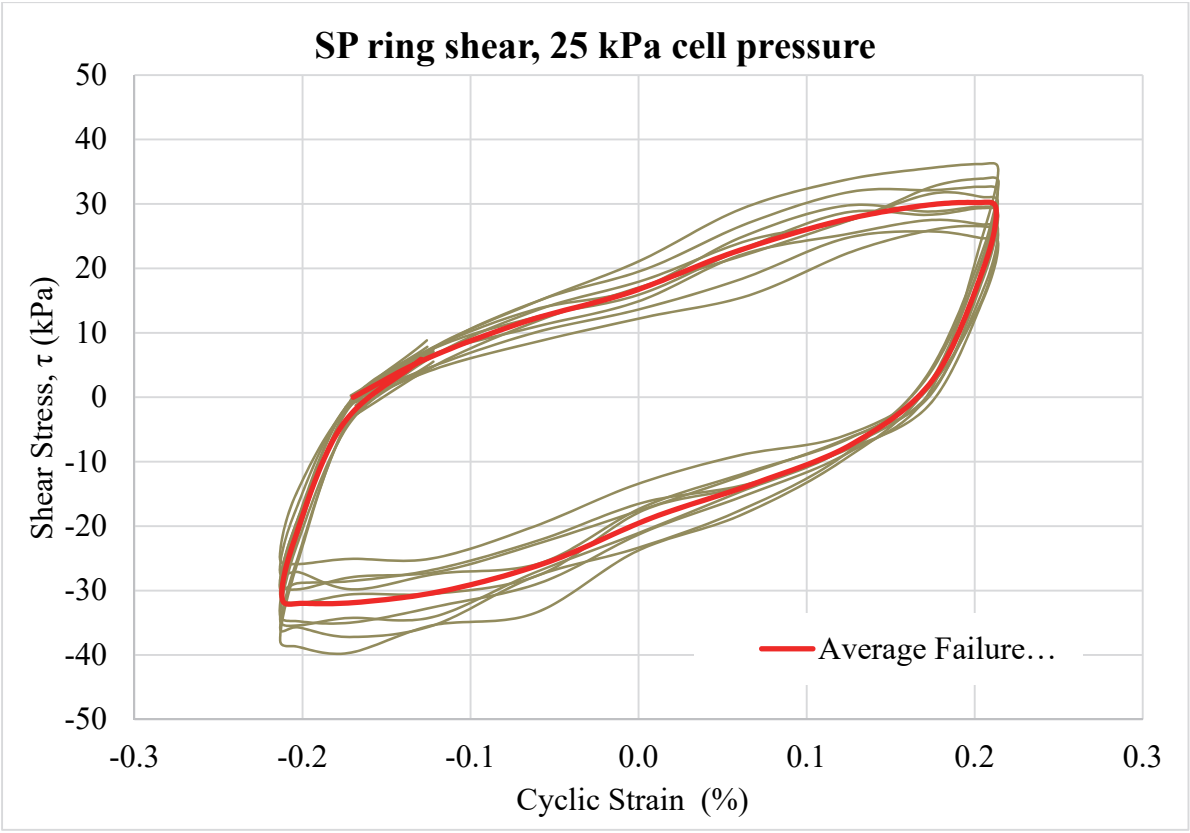
SP ring shear, 25 kPa cell pressure
Shear Stress, τ (kPa)
50
40
30
20
10
0
-10
-20
-30
-40
-50
-0.3
-0.2
-0.1
0.0
0.1
0.2
0.3
Cyclic Strain (%)
Average Failure…

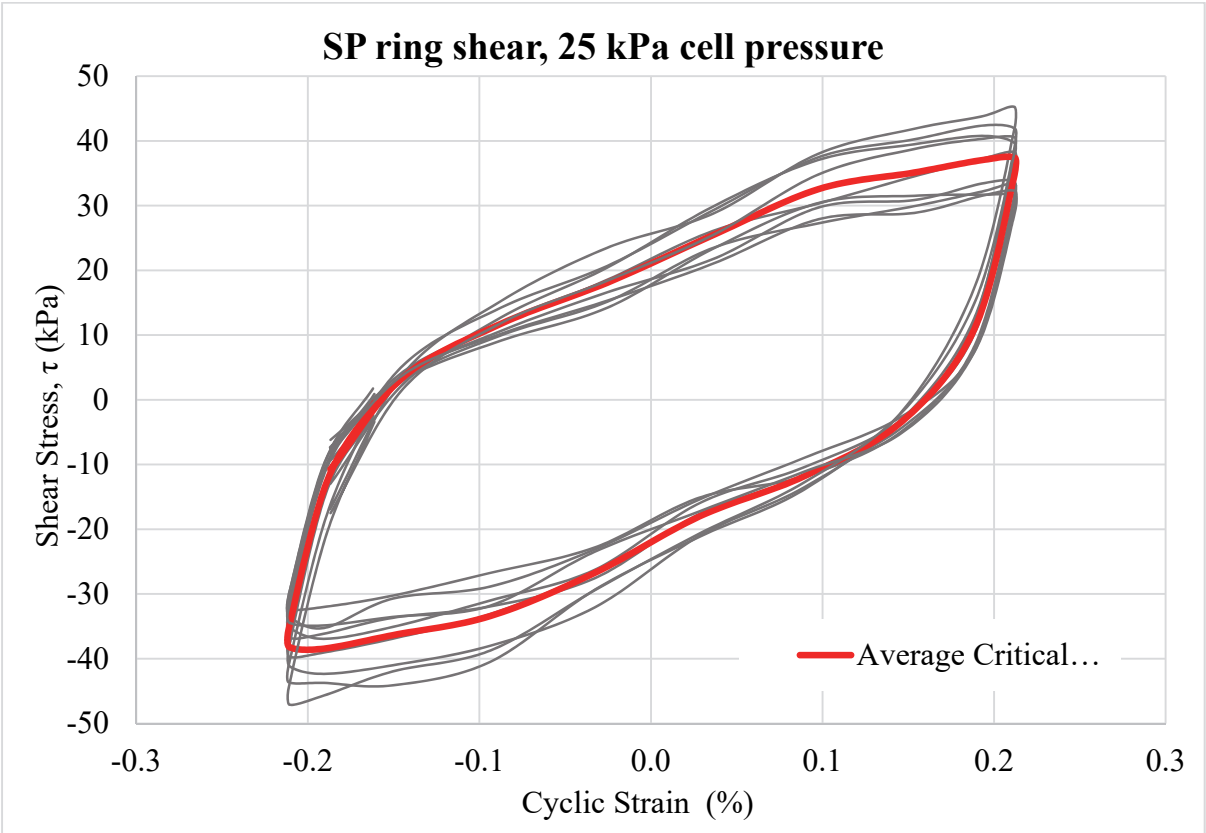
SP ring shear, 25 kPa cell pressure
Shear Stress, τ (kPa)
50
40
30
20
10
0
-10
-20
-30
-40
-50
-0.3
-0.2
-0.1
0.0
0.1
0.2
0.3
Cyclic Strain (%)
Average Critical…

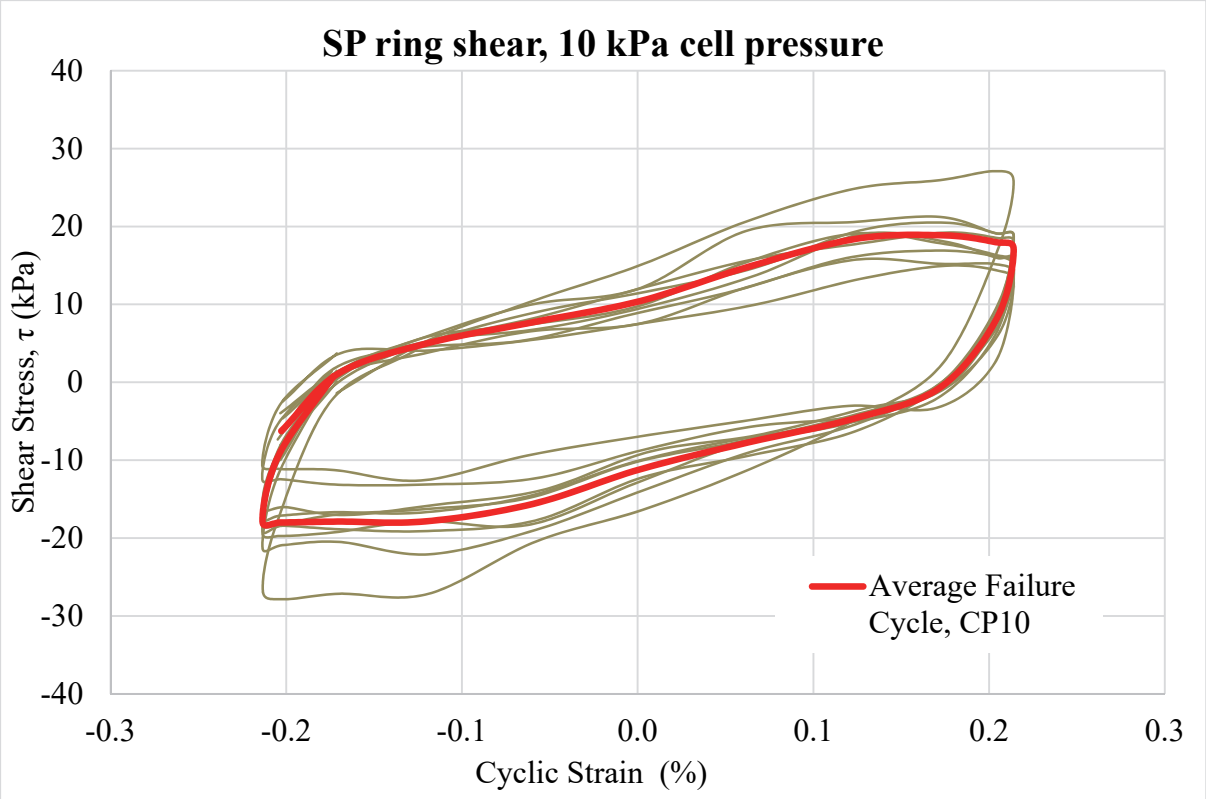
SP ring shear, 10 kPa cell pressure
Shear Stress, τ (kPa)
40
30
20
10
0
-10
-20
-30
-40
-0.3
-0.2
-0.1
0.0
0.1
0.2
0.3
Cyclic Strain (%)
Average Failure Cycle, CP10

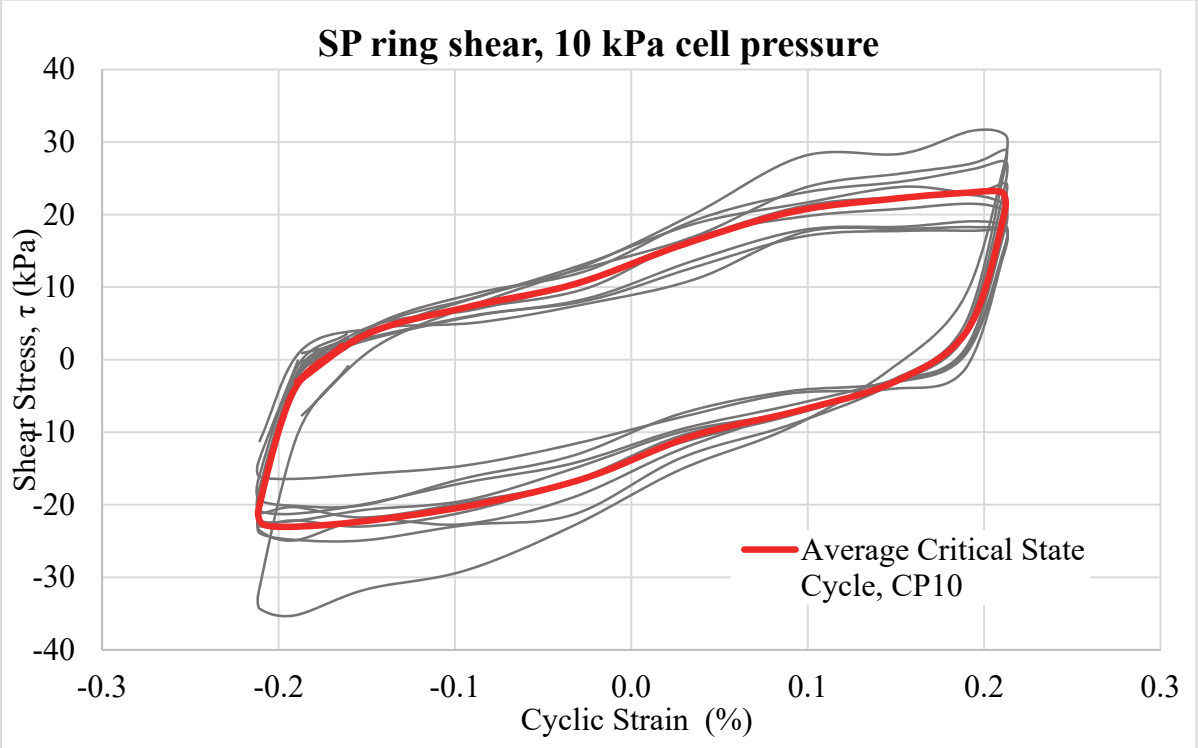
SP ring shear, 10 kPa cell pressure
Shear Stress, τ (kPa)
40
30
20
10
0
-10
-20
-30
-40
-0.3
-0.2
-0.1
0.0
0.1
0.2
0.3
Cyclic Strain (%)
Average Critical State Cycle, CP10

REPORT DOCUMENTATION PAGE

Form Approved
OMB No. 0704-0188

1. REPORT DATE *(DD-MM-YYYY)*	2. REPORT TYPE	3. DATES COVERED *(From - To)*
August 2018	Final report	

4. TITLE AND SUBTITLE

Laboratory Investigations of Cohesionless Shear Strength in Low Confinement Environments

5a. CONTRACT NUMBER

5b. GRANT NUMBER

5c. PROGRAM ELEMENT NUMBER

6. AUTHOR(S)
Katherine E. Winters, Oliver-Denzil S. Taylor, Woodman W. Berry, Amy L. Cunningham, Wesley R. Rowland, and Mark D. Antwine

5d. PROJECT NUMBER
458272

5e. TASK NUMBER

5f. WORK UNIT NUMBER

7. PERFORMING ORGANIZATION NAME(S) AND ADDRESS(ES)

U.S. Army Engineer Research and Development Center
Geotechnical and Structures Laboratory
3909 Halls Ferry Road
Vicksburg, MS 39180-6199

8. PERFORMING ORGANIZATION REPORT NUMBER

ERDC/GSL TR-18-22

9. SPONSORING / MONITORING AGENCY NAME(S) AND ADDRESS(ES)

Headquarters, U.S. Army Corps of Engineers
Washington DC 20314-1000

10. SPONSOR/MONITOR'S ACRONYM(S)

11. SPONSOR/MONITOR'S REPORT NUMBER(S)

12. DISTRIBUTION / AVAILABILITY STATEMENT

Approved for public release; distribution is unlimited.

13. SUPPLEMENTARY NOTES

14. ABSTRACT

In low-confining stress environments, Mohr-Coulomb failure mechanics implies that a cohesionless soil has negligible shear strength. This report presents results of total stress laboratory investigations from triaxial and simple shear loadings for three loose- to medium-dense, cohesionless materials, i.e., a poorly-graded sand (SP), a silty sand (SM), and a silt (ML), at confining pressures ranging from zero to 1000 kPa, as well as cyclic ring shear testing of the SP material at confining pressures from 10 to 100 kPa. All materials exhibited shear strengths and stress paths in excess of expected failure surfaces at confining pressures under 100 kPa. The data indicate that cohesionless soils exhibit significant soil fabric strength characteristics that are not captured by the standard internal friction angle definition, as evidenced by the shear stress intercept of the trendlines relating shear strength and confining pressure. Under low confinement, the continuum fabric dominates the angle of the Mohr envelope. The significant difference in the Mohr envelope shape illustrates that the internal fabric's ability to resist different loading mechanisms cannot be assumed by a linear approximation.

15. SUBJECT TERMS
Laboratory testing
Low confinement
Soil fabric
Soil mechanics
Shear strength
Shear strength of soils-Testing
Sandy soils
Soil erosion
Soil mechanics

16. SECURITY CLASSIFICATION OF:			17. LIMITATION OF ABSTRACT	18. NUMBER OF PAGES	19a. NAME OF RESPONSIBLE PERSON
a. REPORT	b. ABSTRACT	c. THIS PAGE			19b. TELEPHONE NUMBER *(include area code)*
UNCLASSIFIED	UNCLASSIFIED	UNCLASSIFIED	SAR	76	